Inaugural-Dissertation

zur Erlangung der Doktorwürde

der Gesamtfakultät für Mathematik,

Ingenieur- und Naturwissenschaften

der Ruprecht-Karls-Universität Heidelberg

vorgelegt von

Sonja Wieland

Tag der mündlichen Prüfung

05.07.2024

Electrical and Optical Properties of Doped and Functionalized Semiconducting Carbon Nanotube Networks

Gutachter

Prof. Dr. Jana Zaumseil

Dr. habil. Benjamin Scott Flavel

Abstract

The optical properties of single-walled carbon nanotubes (SWCNTs) are governed by near-infrared (NIR) excitons that are stable at room temperature owing to the quasi one-dimensional nanotube nature. Emission from additional states, such as trions and luminescent oxygen defects, can be induced by distinct protocols, but may also occur unintentionally. While trions and luminescent oxygen defects are of different physical origin, both appear at distinct energies that are red-shifted compared to the emission of the mobile excitons and can provide insights into the energy landscape and excited state dynamics of SWCNTs. A trion is a three-particle state of an exciton bound to a positive or negative charge carrier and is formed in the presence of excess charges. Conversely, emission from luminescent lattice defects is of excitonic character. Distinct configurations of covalently bound oxygen defects create trapping potentials below the exciton state, allowing luminescent decay of localized excitons. To date, both trions and oxygen defects have mostly been investigated in dispersed SWCNTs. However, applications in optoelectronic devices usually rely on nanotube networks in contact with other materials that can significantly affect the optical properties of trions and luminescent defects. A better understanding of, and strategies for, the reproducible and robust formation of trions and luminescent oxygen defects in SWCNT networks are therefore required.

Trions are commonly reported in the emission spectra of redoxchemically, electrochemically or electrostatically charged nanotubes. Precise control of trion formation and emission relative to excitons might be achieved by exploiting the high sensitivity of trions towards their dielectric environment. This thesis investigates the influence of different gate dielectric materials on trions and excitons in networks of semiconducting (6,5) SWCNTs that are incorporated into field-effect transistors (FETs). At a given charge carrier density, variations in photo-luminescence (PL) intensities and energies depending on the gate dielectric material, but also trion polarity, are observed. Analysis of the corresponding electrical FET properties identifies charge localization by the dielectric environment as a major factor for the polarity-dependent reduction of exciton quenching, emission blue-shift and trion formation.

While trions can be induced reversibly in SWCNTs through charge accumulation, luminescent oxygen defects usually alter the emissive properties of carbon nanotubes permanently as a result of a chemical reaction of the carbon lattice. In this thesis, a photocatalytic approach is employed to functionalize (6,5) SWCNTs deposited on the transition metal oxides TiO_x and ZnO_x with spatial precision. Optical excitation of these reactive oxidic nanotube environments in the presence of trace amounts of water and oxygen initiates the defect functionalization of adjacent SWCNTs. The emission energies of the two resulting emission bands correspond well to the previously reported ether-d and epoxide-l oxygen defect configurations. The defect PL characteristics are strongly influenced by the surface and dielectric properties of the underlying oxidic substrates, as oxygen-functionalized SWCNTs on TiO_x are brighter than on ZnO_x and pristine nanotubes on glass.

Kurzfassung

Die optischen Eigenschaften einwandiger Kohlenstoff-Nanoröhren (englisch *single-walled carbon nanotubes*, SWCNTs) sind aufgrund ihrer quasi-eindimensionalen Röhrenstruktur selbst bei Raumtemperatur von Nahinfrarot-Exzitonen geprägt. Lichtemission aus weiteren Zuständen, wie etwa Trionen und Sauerstoffdefekten, kann durch bestimmte Verfahren herbeigeführt werden, tritt häufig jedoch auch unbeabsichtigt auf. Wenngleich Trionen und leuchtende Sauerstoffdefekte unterschiedlichen physikalischen Ursprungs sind, treten beide bei bestimmten, im Vergleich zur Emission der mobilen Exzitonen rotverschobenen, Energien auf und können Einblicke in die Energielandschaft sowie die Dynamik der angeregten Zustände von SWCNTs liefern. Trionen bilden sich in Gegenwart von extern induzierten Ladungsträgern und können als Exzitonen, an die jeweils ein Loch oder Elektron gebunden ist, betrachtet werden. Im Gegensatz dazu weist die Emission von leuchtenden Gitterdefekten exzitonischen Charakter auf. Spezielle Konfigurationen kovalent gebundener Sauerstoffdefekte erzeugen Fallenpotentiale, die energetisch tiefer als der Exziton-Zustand liegen und den strahlenden Zerfall der dort lokalisierten Exzitonen ermöglichen. Gegenwärtig werden sowohl Trionen als auch Sauerstoffdefekte vorwiegend in dispergierten SWCNTs untersucht. Anwendungen in optoelektronischen Bauteilen beruhen jedoch hauptsächlich auf Netzwerken von Nanoröhren in Kontakt mit anderen Materialien, welche die optischen Eigenschaften von Trionen und leuchtenden Defekten erheblich beeinflussen können. Ein besseres Verständnis und Strategien für die reproduzierbare und robuste Bildung, oder auch Vermeidung, von Trionen und leuchtenden Sauerstoffdefekten in SWCNT-Netzwerken sind daher erforderlich.

Trionen werden häufig in den Emissionsspektren von redoxchemisch, elektrochemisch oder elektrostatisch geladenen Nanoröhren beobachtet. Die hohe Sensitivität von Trionen gegenüber ihrer dielektrischen Umgebung stellt eine potentielle Möglichkeit zur gezielten Kontrolle der Bildung und Emission von Trionen im Vergleich zu Exzitonen dar. In der vorliegenden Arbeit wird der Einfluss verschiedener Gate-Dielektrikumsmaterialien auf Trionen und Exzitonen in Netzwerken aus halbleitenden (6,5) SWCNTs untersucht, die in Feldeffekttransistoren integriert sind. Bei einer gegebenen Ladungsträgerdichte werden Variationen der Intensität und Energie der Photolumineszenz (PL) in Abhängigkeit vom Gatematerial, aber auch der Polarität der Trionen, beobachtet. Die Auswertung der entsprechenden elektrischen FET-Eigenschaften zeigt, dass Ladungsträgerlokalisierung durch die dielektrische Umgebung ein wichtiger Faktor für die beobachtete polaritätsabhängige Reduktion der Exzitonlöschung, Emissionsblauverschiebung und Trionenbildung ist.

Während Trionen in Kohlenstoffnanoröhren durch Akkumulation von Ladungsträgern reversibel induziert werden können, verändern leuchtende Sauerstoffdefekte die Emissionseigenschaften von SWCNTs in der Regel dauerhaft, da sie mit chemischen Reaktionen am Kohlenstoffgitter einhergehen. Die vorliegende Arbeit verfolgt einen photokatalytischen Ansatz zur Funktionalisierung von auf den Übergangsmetalloxiden TiO_x und ZnO_x abgeschiedenen

(6,5) SWCNTs. Die optische Anregung dieser reaktiven oxidischen SWCNT-Umgebung in Anwesenheit von Spuren von Wasser und Sauerstoff initiiert die Funktionalisierung der umliegenden SWCNTs mit Sauerstoffdefekten. Die Energien der beiden daraus hervorgehenden Emissionsbanden stimmen gut mit den literaturbekannten Ether-d- und Epoxid-l-Sauerstoffdefektkonfigurationen überein. Die Eigenschaften der Defekt-PL werden stark von den Oberflächen- und dielektrischen Eigenschaften der oxidischen Substrate beeinflusst, wobei sauerstofffunktionalisierte SWCNTs auf TiO_x heller als auf ZnO_x und auch heller als unbehandelte SWCNTs auf Glas sind.

Acknowledgements

The PhD journey is rewarding, but can also be tough at times. I am grateful for the colleagues, friends and family who accompanied and supported me along the way.

First of all, I would like to thank Prof. Dr. Jana Zaumseil for her ongoing support, trust and guidance. Moreover, thank you for sharing with me your views on concise paper writing, for providing opportunities to present my research at various international conferences from the very beginning, and for entrusting me with negotiating in the group's interests as representative in the cleanroom user meetings.

I further thank Dr. Benjamin Scott Flavel (Karlsruhe Institute of Technology) for kindly agreeing to be the second reviewer of this thesis, as well as my colleagues for proof-reading.

I send many thanks to all my former colleagues from the NMOE and PC2D group for creating such a supportive and collaborative working atmosphere, and for the countless scientific discussions and exchange of ideas. Thanks to the whole group also for the vibrant social spirit and the fun after-work and weekend activities.

I would like to extend my gratitude to the students I supervised for their dedicated work on their projects, despite the fact that they were not continued. I know that obtaining suboptimal results can be challenging and frustrating, but it is also an integral aspect of the research process, providing opportunities for growth and learning.

I also greatly appreciate the excellent assistance from the administrative and technical staff at the Chair of Applied Physical Chemistry who were always quick to help out, both with administrative support and with advice or a hand when I repaired equipment.

Furthermore, I would like to thank my university and Erasmus friends who have been around not only during my PhD studies, but with whom I share memories since our very first semesters and who made challenging study periods a lot easier to take. Thank you for your constant support, empathy and compassion, even now that we are scattered all over Germany and beyond.

My flat mates are among those who witnessed my PhD journey most intimately, celebrating with me the highs, but likewise cheering me up in the lows. Thank you for the caring atmosphere and empathy, for the memorable moments and engaging discussions in our kitchen and garden, for the many joint gardening and baking experiments, and for your enthusiasm for my scientific explanations of all sorts of everyday occurrences. Our frequent visitor Ruwi also deserves a special word of thanks.

Most importantly, I want to express my gratitude towards my family and boyfriend. Thank you for your unlimited love, care and support throughout the years of my PhD studies and before.

Contents

Abbreviations

AFM	Atomic force microscopy
ALD	Atomic layer deposition
BCB	Divinyltetramethylsiloxane-bis-benzocyclobutene
CoMoCAT	Cobalt-molybdenum catalyst
DOS	Density of states
EVET	Electronic-to-vibrational energy transfer
FET	Field-effect transistor
FWHM	Full width at half maximum
HfO_x	Hafnium oxide
IRF	Instrument response function
MIS	Metal-insulator-semiconductor
MPD	Multi-phonon decay
NIR	Near-infrared
NMP	*N*-Methyl-2-pyrrolidone
PFO-BPy	Poly[(9,9-dioctylfluorenyl-2,7-diyl)-*alt*-(6,6'-2,2'-bipyridine)]
PL	Photoluminescence
PLQY	Photoluminescence quantum yield
PMMA	Poly(methyl methacrylate)
PS	Polystyrene
PVDF-TrFE-CTFE	Poly-(vinylidene fluoride-*co*-trifluoroethylene-*co*-chlorotrifluoro-ethylene
RBM	Radial breathing mode
rms	Root mean square roughness
ROS	Reactive oxygen species
SWCNT	Single-walled carbon nanotube
TCSPC	Time-correlated single-photon counting
(Teflon) AF2400	(poly-[4,5-difluoro-2,2-bis(trifluoromethyl)-1,3-dioxole-*co*-tetra-fluoroethylene]
THF	Tetrahydrofuran
TiO_x	Titanium dioxide
ttmgb	1,2,4,5-tetrakis(tetramethylguanidino)benzene
UV	Ultraviolet
Vis	Visible
ZnO_x	Zinc oxide

1. Introduction

The increasing demand for low-cost electronics and miniaturization have intensified the exploration of alternative materials to traditional inorganic semiconductors in the past decades. Carbon-based materials have attracted significant attention due to their potential for cost-effective processing, as they are mostly solution-processable and do not necessitate energy-intensive purification and processing. Among these alternatives, semiconducting single-walled carbon nanotubes (SWCNTs) with their exceptional charge transport properties alongside high photo- and temperature-stability[1,2] are particularly promising for various electronic applications. They also provide additional functionalities, including mechanical flexibility and stretchability, and their narrowband near-infrared (NIR) optical transitions.[3,4] The distinct transition energies are determined by the SWCNT species, commonly referred to as chirality, and fine-tuned by their environment. The NIR wavelength range is highly relevant for biological sensing[5,6] and telecommunication applications.[7] SWCNTs with their high and balanced hole and electron mobilities[3,4] are also interesting for optoelectronic applications as they exhibit electrically induced emission (electroluminescence) in addition to the optically induced photoluminescence (PL). Their small diameters, typically of a few nanometers, and high aspect ratios[8] make them an intriguing model system for one-dimensional semiconductors, with properties distinctly different from three-dimensional bulk semiconductors.

The excited states in SWCNTs are of excitonic character even at room temperature due to the strong axial confinement in the nearly one-dimensional nanotubes. However, the high probability of non-radiative decay of the mobile excitons at the tube ends,[9] together with the existence of optically dark exciton states,[10] results in low photoluminescence quantum yields of ~ 1 %.[11] Charged impurities and lattice defects in the SWCNTs, introduced unintentionally during nanotube processing or device fabrication and operation, may not only impede charge transport,[12,13] but further reduce the photoluminescence through exciton quenching.[14,15] Moreover, their interaction with excitons can result in the appearance of additional emission features that lie energetically below the exciton emission and are detrimental for applications demanding high spectral purity, such as organic light-emitting diodes.[16] Yet, these additional emission features can contribute to a better understanding of the energy landscape and excited state dynamics of carbon nanotubes. Accordingly, many protocols for the controlled introduction of charged impurities and luminescent defects into SWCNTs have been

developed to date, enabling the assignment of the charge carrier- and defect-induced red-shifted emission to radiative decay of trions[17,18] and trapped excitons,[19,20] respectively.

Trions are three-particle bound states of two holes and one electron or two electrons and one hole.[21] They can be considered as positively or negatively charged excitons as they form upon diffusive encounter between a mobile exciton and a charge carrier. Importantly, the process of trion formation is concomitant with the carrier-induced quenching of photoluminescent excitons. Trions can be created through optical excitation of SWCNTs in the presence of redoxchemically,[17,22] electrochemically[23–26] or electrostatically[16,27,28] induced charges, and in electroluminescent devices.[24,29–31] Since their emission intensity relative to the exciton depends on the number of charge carriers present on the nanotube, they are indicators of the nanotube doping state.[32–34] Similar to excitons, trions are highly susceptible to changes in the dielectric environment as a result of the limited dielectric screening in SWCNTs,[35,36] but little systematic research has been devoted to their interactions with their environment to date. A universal understanding of the factors influencing trion formation and emission, however, is crucial for both avoiding trion emission when high spectral purity is required, and investigating the potential of these charged excited states with their non-zero spin.[27,37–39]

In contrast to trions, luminescent defect emission originates from excitons localized at lattice defects. Local potential minima at luminescent defect sites capture the excitons, improving nanotube PL as the trapped excitons are no longer subject to diffusive quenching but instead decay radiatively with emission energies lowered with respect to the freely diffusing excitons.[20,40] Yet, only well-defined defect configurations give rise to luminescent exciton decay, whereas oxidative damage of carbon nanotubes caused by harsh environmental conditions can significantly quench their PL.[15] Careful chemical reaction design is therefore required to create luminescent defects, and the precise configuration determines their emission energy.[19,41–44] While the covalent attachment of alkyl and aryl moieties (so-called sp^3 defects) to the carbon lattice offers additional possibilities for emission tuning through variation of their electronic properties, the introduction of functional oxygen groups (ether, epoxide) usually requires less sophisticated experimental protocols. Irrespective of the defect type, their distinct properties result from the same physical origin as they possess zero-dimensional character.[45] As a result, they can only host one exciton at a time and exhibit room-temperature single-photon emission at telecommunication wavelengths, making them interesting materials for optical quantum information technologies.[46–48] Moreover, the brightening and shift of nanotube emission further into the infrared offers new perspectives for their use in, *e.g.*,

sensing.[49–52] Solid-state approaches for the introduction of luminescent defects with spatial precision also open possibilities for on-chip emission tuning.[53]

The formation and emissive properties of both trions and luminescent defects have mainly been studied in dispersed SWCNTs, even though deposited networks of SWCNTs are more relevant for applications in optoelectronic devices.[3,54] Yet, their optical spectroscopy suffers from additional challenges compared to nanotube dispersions due to the increase in environmental heterogeneity. Within a network, the individual nanotubes interact distinctively with adjacent nanotubes and with the substrate or encapsulating layers, resulting in, *e.g.*, broadening of the ensemble emission bands.[55] The PL properties of carbon nanotubes are most unambiguously studied in single-chirality samples to rule out charge and energy transfer between different SWCNT species,[56–58] so that all spectral features are clearly distinguishable and assignable to the chirality under investigation. This thesis studies trions and luminescent oxygen defects in networks of monochiral (6,5) SWCNTs, which are among the most-studied nanotubes since they are readily available in high purities and quantities.[11] Positive and negative trions are induced through electrostatic charging of (6,5) SWCNTs in FETs, and oxygen defects are created in substrate-deposited nanotubes through a new photocatalytic approach. The results highlight the significant impact of environmental factors on carbon nanotubes.

The thesis is structured as follows: **Chapter 2** provides the necessary background knowledge, including basics of carbon nanotubes, the current understanding of trions and oxygen defects, and the working principle of field-effect transistors with a focus on SWCNT network-based devices. **Chapter 3** covers the materials as well as the experimental and analytical procedures employed in this thesis. In **Chapter 4**, the combined analysis of the optical and electrical properties of electrostatically charged (6,5) SWCNT networks in FETs, depending on the gate dielectric material, charge carrier polarity and trap density, gives insights into the external factors influencing trion formation and emission. Charge carrier trapping is found to play a crucial role and is further investigated through deliberate removal of electron traps with the reducing agent 1,2,4,5-tetrakis(tetramethylguanidino)benzene (ttmgb). **Chapter 5** presents a method to introduce oxygen defects with spatial precision into networks of (6,5) SWCNTs on different substrates using photocatalytically created reactive oxygen species (ROS). For this purpose, two different photoreactive transition metal oxides, TiO_2 and ZnO, are tested and found to have a distinct impact on the PL from the resulting oxygen-functionalized nanotubes. The thesis concludes with **Chapter 6**, summarizing the results and providing a perspective for further studies.

2. Background

This chapter introduces the relevant theories and concepts used in this thesis. It discusses the electrical and general optical properties of single-walled carbon nanotubes with a focus on their susceptibility to external influences, followed by an overview of special optical features that are observed upon nanotube charging or functionalization with oxygen, respectively. The chapter concludes with an introduction to the operating principle of field-effect transistors with specific focus on ambipolar carbon nanotube network-based devices.

2.1 Single-walled carbon nanotubes

Single-walled carbon nanotubes are best described as hollow cylinders of sp^2-hybridized carbon atoms. Their high aspect ratio, with tube diameters on the order of 1 nm and tube lengths of several μm, makes them suitable model systems for one-dimensional semiconductors.[59] If several SWCNTs of different diameters are stacked inside each other, they are referred to as multi-walled carbon nanotubes.[60] Yet, only single-walled carbon nanotubes are of relevance for optoelectronic applications due to their well-defined and structure-dependent electronic and optical properties.[61,62] This thesis investigates semiconducting SWCNTS, and this section thus focuses on their structure and specific optical and electrical properties. Further emphasis is placed on their high sensitivity towards external influences such as changes in the immediate environment and the presence of charge carriers.

2.1.1 Structure

SWCNTs can be conceptually understood as seamlessly rolled up sheets of graphene, which consist of purely sp^2-hybridized carbon atoms arranged in a planar honeycomb lattice (see **Figure 2.1**).[59] The circumferential roll-up vector $\vec{C}_\mathrm{h}$ describes the coinciding carbon atoms

through a linear combination of the primitive lattice vectors $\vec{a}_1$ and $\vec{a}_2$, and hence the nanotube circumference, according to

$$\vec{C}_\mathrm{h} = n\vec{a}_1 + m\vec{a}_2 \,. \tag{1}$$

The length of the lattice vectors can be calculated from the carbon-carbon distance in the graphene lattice, $a_{\mathrm{C-C}} = 0.142$ nm, as $a = \sqrt{3}\, a_{\mathrm{C-C}} = 0.246$ nm. It defines the nanotube diameter d together with the integer pair (n, m) as

$$d = \frac{|\vec{C}_\mathrm{h}|}{\pi} = \frac{a}{\pi}\sqrt{n^2 + nm + m^2} \,. \tag{2}$$

Moreover, the roll-up angle α with respect to the primitive lattice vectors $\vec{a}_1$ can be calculated from the parameters n and m through the trigonometric relationship

$$\cos(\alpha) = \frac{2n + m}{2\sqrt{n^2 + nm + m^2}} , \tag{3}$$

making the (n, m) pair sufficient to uniquely define the SWCNT geometry. Irrespective of the symmetry-related context of the term chirality, the combinations of n and m are commonly

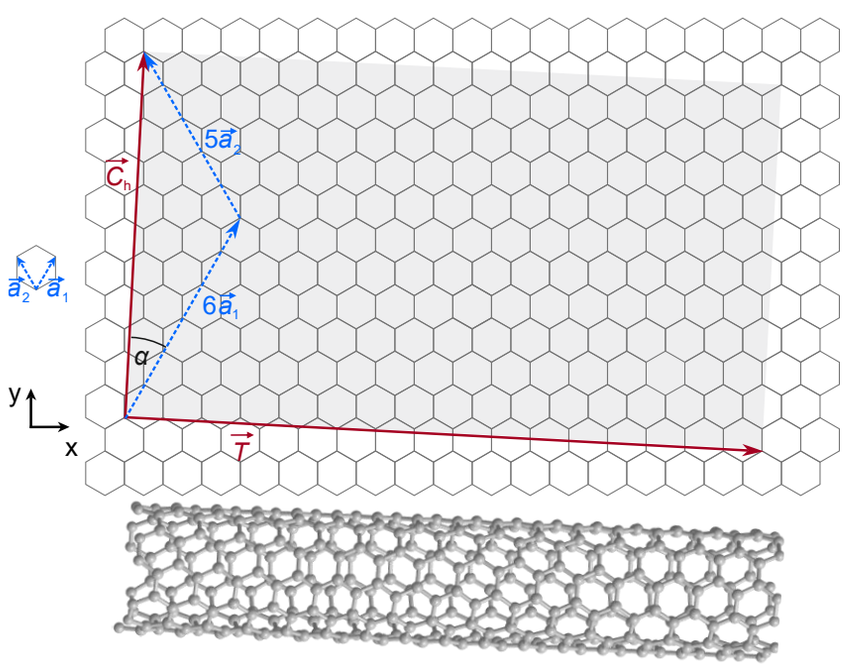

Figure 2.1: Schematic construction of a (6,5) SWCNT from a graphene sheet. The roll-up vector $\vec{\boldsymbol{C}}_\mathbf{h}$ and the chiral angle $\boldsymbol{\alpha}$, defined through linear combination of multiples of the primitive lattice vectors $\vec{\boldsymbol{a}}_\mathbf{1}$ and $\vec{\boldsymbol{a}}_\mathbf{2}$, determine the tube diameter. The longitudinal periodicity is given by the translational vector $\vec{\boldsymbol{T}}$.

referred to as chirality, and α is also called chiral angle. Due to the symmetry of the hexagonal honeycomb lattice, chiral angles from 0° to 30° are sufficient to describe all SWCNT structures. Zigzag SWCNTs with $(n, 0)$ and armchair SWCNTs with (n, n) exhibit chiral angles $\alpha = 0°$ and 30°, respectively, and are achiral. All other (n, m) SWCNTs are chiral, and the integer pair (m, n) corresponds to their enantiomers.

While SWCNTs typically exhibit very high aspect ratios, they can fundamentally be described by a unit cell spanned by the circumferential vector $\vec{C}_\mathrm{h}$ and the translational vector $\vec{T}$, that is, the shortest graphene lattice vector orthogonal to $\vec{C}_\mathrm{h}$. Accordingly, the length of the nanotube can be expressed as multiples of $|\vec{T}|$ if the half-sphere-capped or open tube ends[63] are neglected.

2.1.2 Synthesis, purification and sorting

Synthesis methods for carbon nanotubes are commonly based on the decomposition of a carbon-containing precursor, catalyzed by transition metal nanoparticles or compounds thereof.[64] Chemical vapor deposition (CVD) techniques using gaseous precursors are predominantly employed for the large-scale, commercial synthesis of SWCNTs. The (6,5) SWCNTs investigated in this thesis are produced with the CoMoCAT process, named after the bimetallic cobalt-molybdenum catalyst.[65] Here, carbon monoxide serves as the carbon source for preferential growth of small-diameter SWCNTs ($d \sim 0.7 – 1.2$ nm) at reaction temperatures of 700 – 850 °C and pressures of 1 – 10 atm. Subsequent acid treatment dissolves the support material, releasing the SWCNTs. Other methods rely on plasma technologies,[66] laser ablation[67] or electric-arc discharge,[68] which require higher temperatures (> 1000 °C) and produce carbon nanotubes with larger diameters ($d \sim 1 – 2$ nm). Templated synthesis for chirality-specific SWCNT growth is also investigated, but currently still produces limited quantities and purities.[69]

Irrespective of the employed method, the as-produced SWCNTs are contaminated with amorphous carbon and residual catalyst particles. Moreover, existing growth processes yield a manifold of metallic and semiconducting chiralities. For optoelectronic applications, the impurities must be removed and metallic and semiconducting SWCNTs need to be separated, and some applications even require enantiomeric purity. Nanotube sorting is further complicated through the attractive van-der-Waals interactions between the extended π-systems of the nanotube sidewalls, which result in nanotube bundling,[70] and by the poor solubility of SWCNTs in nearly all solvents.[71] Thus, current solution processing strategies[70,72] require a

de-bundling step in which the as-produced nanotube raw material is sonicated (typically bath sonication or tip sonication) in the respective solvent and immediate re-aggregation is prevented through the addition of a stabilizing agent, that is, a surfactant or polymer. Impurities and remaining nanotube bundles are sedimented subsequently through centrifugation. The obtained supernatant contains individual, dispersed SWCNTs. Selectivity towards the electronic type (metallic or semiconducting), one or several chiralities, or even the enantiomeric forms is either achieved through choice of the stabilizing agent or through an additional sorting step[73] like density-gradient ultracentrifugation, gel permeation chromatography, dielectrophoresis or aqueous two-phase extraction.

While surfactants like sodium dodecyl sulfate or sodium (deoxy-)cholate typically yield a dispersion of different metallic and semiconducting carbon nanotubes,[72,73] π-conjugated polymers with long alkyl chains can extract nanotubes in organic solvents with high chiral purity already in the dispersion step.[74,75] The polymer chains selectively wrap around their preferred chiralities, which are thus stabilized against re-aggregation and can be separated from the non-exfoliated material by centrifugation. For example, the (6,5) SWCNTs studied in this thesis were selectively extracted from CoMoCAT raw material in toluene using the fluorene-bipyridine copolymer poly[(9,9-dioctylfluorenyl-2,7-diyl)-alt-(6,6'-2,2'-bipyridine)] (PFO-BPy) shown in **Figure 2.2**. Polyfluorenes and copolymers thereof are most widely employed,[74,76–78] but other polymer classes like polythiophenes[79] and polycarbazoles[80] have also been used to sort nanotubes with this so-called polymer wrapping approach, and small changes in the polymer structure were found to result in significantly different preferences for single chiralities or broader diameter ranges. Despite considerable theoretical efforts and the large library of wrapping polymers identified to date, the mechanisms behind chiral selectivity and yield of the dispersion process are still only poorly understood. The molecular weight of the wrapping polymer,[81,82] the length of its alkyl chains,[77] the viscosity of the solvent[82,83] and the doping state of the SWCNTs[84] have experimentally been identified as influencing factors.

Finally, it should be pointed out that the harsh conditions of nanotube de-bundling, which forms the basis of current purification and sorting strategies, can induce severe damage to the

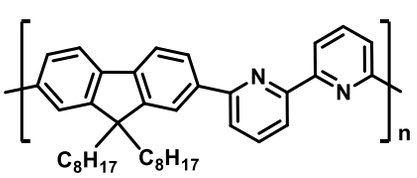

Figure 2.2: Structure of the polymer PFO-BPy, which selectively wraps (6,5) SWCNTs.

carbon lattice and shorten the nanotubes, deteriorating both charge transport and optical properties of SWCNTs.[85] Shear-force mixing in combination with polymer-wrapping was found to be less harmful than sonication techniques, and can provide SWCNTs with high quality and purity in large amounts.[11]

2.1.3 Electronic structure

The electronic structure of SWCNTs can be derived from the band structure of graphene, specifically, from the bonding π and antibonding π* bands, within the nearest-neighbor tight-binding formalism.[86] These bands, also referred to as valence and conduction band, govern the optical transitions of graphene. In proximity to the K and K' points of the first Brillouin zone,

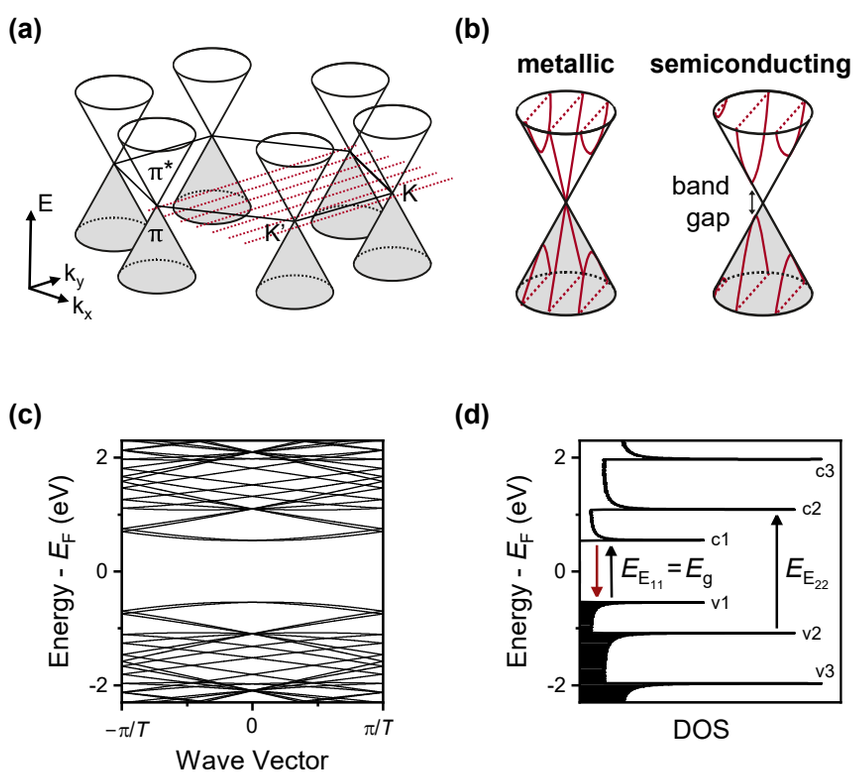

Figure 2.3: Derivation of the nanotube DOS from the graphene band structure, assuming electron-hole symmetry. a) The graphene band structure exhibits Dirac cones with a linear dispersion around the K and K' points. The SWCNT sub-bands are obtained by conceptual consideration of the allowed wave vectors in the circumferential direction as cutting lines (visualized in red). b) Semiconducting or metallic SWCNTs, depending on the position of the cutting lines with respect to the K points. c) Band structure and d) DOS distribution for a semiconducting (6,5) SWCNT. Allowed optical transitions between the first and second van Hove singularities, respectively, are visualized with arrows. In the single-particle picture, the energy of the E_{11} transition, E_{E11}, corresponds to the band gap E_g.

they possess a near-linear dispersion and are approximately symmetrical since electron-hole symmetry can be assumed, giving rise to the so-called Dirac cones (see **Figure 2.3a**).[59,86]

Rolling up the graphene sheet to create the nanotube imposes periodic boundary conditions onto the electron wave vector in this direction. Boundary conditions also exist for the axial wave vectors. Yet, the allowed wave vectors in axial direction can be considered as continuous in the limit of very long SWCNTs ($L \gg |\vec{T}|$).[87] Thus, the electronic motion is quantized with discrete allowed states only around the tube circumference, resulting in sub-bands within the SWCNT conduction and valence bands that define the SWCNT band structure.[87] The sub-bands are obtained by slicing the graphene band structure as visualized in **Figure 2.3a**. The roll-up angle dictates the orientation of these lines within the Brillouin zone. If a line intersects the Dirac cone at the K or K' point (see **Figure 2.3b**), where valence and conduction band meet in the graphene band structure, the nanotube is metallic due to the finite density of states (DOS) at the Fermi level. Otherwise, a band gap E_g exists and the nanotube is semiconducting. The (n, m) pair provides information about the electronic type of each nanotube species. The $(n - m)$ mod 3 = 0 nanotubes are metallic, with the non-armchair $(n \neq m)$ SWCNTs exhibiting small curvature-induced band gaps on the order of tens of meV.[88] The remaining two thirds of nanotube structures, with $(n - m)$ mod 3 = $\pm$ 1, are semiconducting. The band gap of the semiconducting species roughly scales with d^{-1} due to the linear dispersion of the Dirac cone around the Fermi level and can be estimated according to

$$E_{\mathrm{g}}\,(\mathrm{eV}) \sim \frac{0.7}{d\,(\mathrm{nm})}. \tag{4}$$

The total density of states (DOS) distribution of SWCNTs can be derived from the summed-up sub-band DOS (see **Figure 2.3c**) as multiple sharp peaks, visualized in **Figure 2.3d** for a semiconducting (6,5) SWCNT. These so-called van Hove singularities are characteristic for electrons in a one-dimensional system. As mentioned above, the DOS is zero around the Fermi level for semiconducting SWCNTs and takes on a finite value in case of metallic nanotubes.

It is important to acknowledge that the presented nearest-neighbor tight-binding and zone-folding formalisms encompass several approximations, such as neglecting curvature-induced deviations from the sp^2 hybridization particularly towards small tube diameters.[86,89] However, despite these simplifications, the resulting density of states (DOS) closely matches the electronic structure of carbon nanotubes reported by scanning tunneling microscopy[90] and has successfully been used for describing charge transport and thermoelectric behavior of carbon nanotubes.[91,92] The van Hove singularities can also describe some of the optical properties of SWCNTs, but fail to describe details of the transitions, as will be discussed in the next section.

2.1.4 Excitons

Semiconducting SWCNTs possess a direct bandgap that enables optically or electrically induced luminescence. In contrast to that, fast non-radiative carrier relaxation prevents emission from metallic nanotubes. Since the transition rate is proportional to the joint DOS of the initial and final state, the single-particle DOS distribution (see Section 2.1.3) can explain the narrow absorption and emission bands observed in the optical spectra of semiconducting SWCNTs as transitions between occupied (valence band) and unoccupied (conduction band), sharp van Hove singularities (see **Figure 2.3d**).[93] Conservation of angular momentum permits only E_{ii} transitions between the i^{th} van Hove singularities in the valence (v1, v2, …) and the conduction band (c1, c2, …) for electric fields parallel to the nanotube axis.[94] E_{ij} transitions ($i \neq j$) are allowed perpendicular to the tube axis, but are not observed in the optical spectra of SWCNTs since the absorption cross section in the perpendicular direction is substantially smaller than in the parallel direction (antenna effect).[95]

In the single-particle picture, the energy of the optical transition between the first van Hove singularities, $E_{\text{E}11}$, corresponds to the single-particle band gap E_{g} of the carbon nanotube.[93] However, there exists a notable disparity between the experimentally observed transition energies and E_{g} calculated from the tight-binding model.[93,96,97] Thus, the simple picture of an excited state with free holes and electrons is not sufficient, and many-body effects need to be considered when describing excited states in SWCNTs due to the weak dielectric screening in low-dimensional systems (see **Figure 2.4a**).[98] Strong electron-hole interactions result in the formation of bound electron-hole pairs, that is, excitons with binding energies E_{b} that are significantly larger compared to inorganic, bulk semiconductors. Through two-photon excitation spectroscopy, exciton binding energies in the range of several 100 meV have been reported,[99,100] making excitons in SWCNTs stable and observable at room temperature. In addition to E_{b}, which characterizes the attractive electron-hole interaction, many-body interactions involve a second term to account for the repulsive interaction between the excited electron in the conduction band and the electrons which remained in the valence band, *i.e.*, the self-energy E_{self}. Thus, the E_{11} transition energy $E_{\text{E}11}$ is expressed as

$$E_{\text{E}_{11}} = E_{\text{g}} - E_{\text{b}} + E_{\text{self}} \tag{5}$$

within the many-body framework. In SWCNTs, E_{self} exceeds E_{b}, resulting in many-body effects that increase $E_{\text{E}11}$ compared to the single-particle band gap.[10,98]

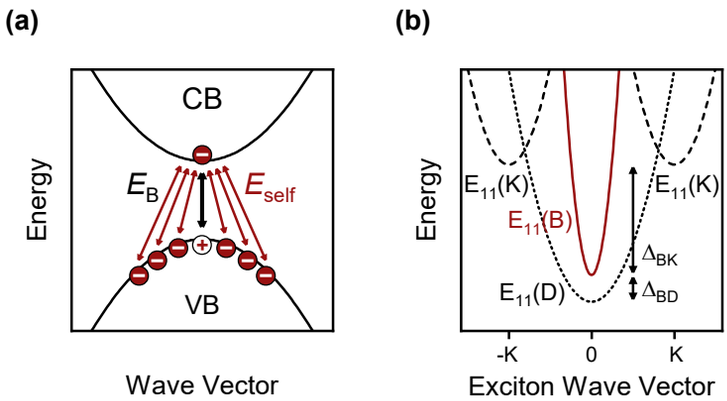

Figure 2.4: Excited states of SWCNTs within the excitonic picture. a) Illustration of many-body effects with strong attractive electron-hole and repulsive electron-electron interactions, expressed through exciton binding energy, E_b, and self-energy, E_{self}. b) Schematic energy dispersion of the singlet E_{11} states.

As a consequence of the K and K' valley degeneracy in the graphene lattice, each excitonic level exhibits four distinct electron-hole pair excitations arising from the possible distributions of the hole and electron across the two valleys (intravalley: KK, K'K', intervalley: KK', K'K). Additionally, each of the valley configurations can host four different exciton spin configurations, that is, one singlet and three triplets. Each E_{ii} state therefore comprises a manifold of 16 excitons. Direct optical transitions require momentum conservation, making the two intervalley (K-momentum) excitons, $E_{11}(K)$, optically forbidden (dark). Triplet excitons are also dark due to the spin conservation imperative together with the weak spin-orbit coupling in SWCNTs. Mixing of the intravalley (zero-momentum) singlet excitons as a result of the short-range Coulomb interactions in SWCNTs lifts their degeneracy by splitting into a bonding and antibonding state of odd and even parity, respectively.[101] Since the selection rules require direct optical transitions to occur between states of opposite parity, the even-parity, zero-momentum exciton is dark and thus typically referred to as $E_{11}(D)$.[62] Thus, among the 16 exciton states, only the odd-parity, zero-momentum singlet exciton, $E_{11}(B)$, is optically allowed in one-photon absorption or emission processes.

The energy dispersion of the E_{11} singlet exciton manifold is schematically visualized in **Figure 2.4b**. Notably, the $E_{11}(B)$ dispersion exhibits a markedly steeper profile than the $E_{11}(D)$ dispersion as a result of the lower effective mass of the bright exciton compared to the dark exciton.[102] Owing to the bright-dark splitting Δ_{BD}, the dark zero-momentum exciton is located a few meV below the bright exciton.[103] The dark K-momentum excitons reside around 25 meV above the bright excitons (Δ_{BK}).[104] In a first approximation, Δ_{BD} and Δ_{BK} scale inversely with

the tube diameter, *i.e.*, $\Delta_{BD} \sim d^{-1}$ and $\Delta_{BK} \sim d^{-1}$. In contrast to the dark singlet excitons, the understanding of triplet excitons remains limited. Results from different experimental and theoretical studies present a great variation in the proposed E_{11} triplet energies. Yet, experimental confirmation of the theoretically predicted tube diameter-dependence of the singlet-triplet splitting, which follows a d^{-2} scaling,[105] has been achieved.[106]

2.1.5 Optical properties

The peculiar DOS and above-discussed many-body interactions in the nearly one-dimensional SWCNTs gives rise to characteristic optical properties. Typical absorption and emission spectra from (6,5) SWCNTs are shown in **Figure 2.5**. The absorption spectrum exhibits characteristics resonances in the visible and NIR spectral range that correspond to the E_{22} (~ 2.156 eV, 575 nm) and E_{11} (~ 1.240 eV, 1000 nm) transitions, respectively. In contrast to that, the PL spectrum only displays one prominent peak that corresponds to the E_{11} transition even after optical excitation into a higher excitonic state, such as the E_{22} exciton, as a consequence of the fast internal relaxation to the E_{11} manifold, which occurs within ~ 100 fs.[107,108] The very narrow bandwidth (~ 20 meV in the presented spectrum) and very small Stokes shift (~ 4 meV) of the E_{11}(B) emission is related to the rigidity of the SWCNT lattice and concomitant small reorganization energy.[109]

The optical spectra of SWCNTs feature additional, weaker bands, which arise from brightening of dark excitons, *e.g.*, through coupling to phonon modes. The strongest sideband is suggested to result from exciton scattering at lattice defects[110,111] and thus corresponds to the excitation (decay) of the dark E_{11}(K) exciton under absorption (emission) of a D phonon with energy $\hbar\omega_D$.[104,112] Moreover, a weak vibronic sideband occurs in the emission spectrum through

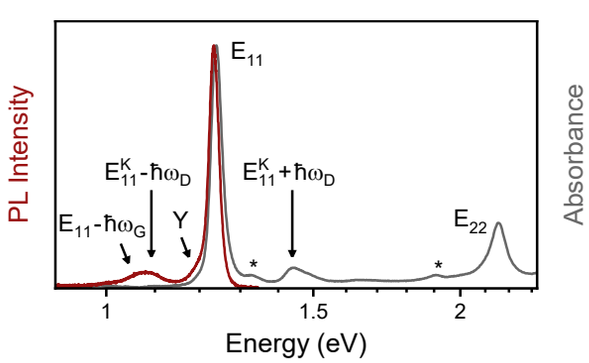

Figure 2.5: Absorption and photoluminescence spectra of (6,5) SCWCNTs with assignment of the main excitonic transitions and sidebands. Impurity signals are marked with an asterisk (*).

coupling of the bright E_{11}(B) exciton to a G phonon mode with energy $\hbar\omega_G$ at red-shifted energies compared to the brightened K-momentum exciton.[104] The Y band, which appears as a red-shifted shoulder to the bright exciton emission, has previously been assigned to extrinsic factors or brightened triplets.[112] Recent investigations suggest that its origin may be linked to defects induced externally through interactions between the nanotubes and polar substrates,[55] in agreement with the observation of significant Y band enhancement in deposited SWCNT networks compared to nanotubes in dispersion. Moreover, a strongly red-shifted PL sideband associated with the unintentional introduction of oxygen defects during nanotube processing is frequently observed.[113]

The existence of dark exciton states affects the photophysical properties of SWCNTs particularly at low temperatures (< 50 – 100 K, tube diameter-dependent), when the thermal distribution favors the dark E_{11}(D) state, thus significantly reducing exciton PL.[103] However, dark excitons alone cannot completely account for the generally low PL quantum yields in (6,5) SWCNTs. Instead, bright excitons can decay non-radiatively at quenching sites like the tube ends or lattice defects.[9,114] Excitons are highly mobile along individual nanotubes and sample large parts of the nanotube during their lifetime (~ 10 – 100 ps)[62] due to their high diffusion constants of 1 – 10 $cm^2 s^{-1}$.[9,115,116] Thus, they will encounter a quenching site with high probability, making diffusive exciton quenching dominant over radiative exciton decay.

The immediate environment of SWCNTs (*e.g.*, surfactant, wrapping polymer, solvent, other nanotubes)[117] presents another factor that significantly affects the emissive properties of excitons, such as quantum yields and transition energies. The high susceptibility of excitons towards their environment originates from the small nanotube diameters. This characteristic causes the electric field lines, which define the Coulomb interaction between hole and electron, to extend into the surrounding medium outside the nanotube.[118] The dielectric environment adds external screening to the internal Coulomb interactions,[119] reducing the exciton binding energy. Perebeinos *et al.*[120] proposed a power law scaling of the binding energy with the dielectric constant of the environment ε, $E_b \propto \varepsilon^{-1.4}$. In combination with the concomitant, dominating self-energy reduction,[117,121] this results in a lowering, *i.e.*, a solvatochromic red-shift, of the optical transition energies (see Equation (5)) by several tens of meV.[118,122–124] Due to these electronic effects, local variations in the dielectric environment along the axis of a single nanotubes enabled the localization of excitons at cryogenic temperature.[125] Notably, deposited networks of SWCNTs experience a multitude of different environments through, *e.g.*, tube-tube, tube-surfactant and tube-substrate interactions, resulting in significant PL broadening.[55,126–128]

Apart from the transition energies, the PL quantum yield also decreases as a function of the environmental dielectric constant.[123] Exciton dissociation, that is, non-radiative decay, is facilitated upon external screening,[129] and strong dielectric interactions of nanotubes on polar substrates can even lead to total PL quenching.[128,130] It has further been suggested that electrophile solvents additionally reduce the quantum yield by perturbation of the electronic structure, creating non-radiative decay sites.[129] Finally, it should be noted that endohedral encapsulation of, *e.g.*, solvents, inside the SWCNT also affects the dielectric environment and transition energies.[131] This effect becomes relevant for large-diameter tubes capable of hosting molecules within their cavity.

Another significant external influence on the emissive properties of SWCNTs arises from the presence of charge carriers on the nanotubes, which substantially affects exciton photophysics and can even induce trion formation (see Section 2.2). While nanotube charging thus aids in the investigation of fundamental electronic and excited state properties of carbon nanotubes, it may also be undesired since it causes a reduction in exciton PL intensity. One reason for this phenomenon is the significant absorption bleaching caused by the reduction of available valence or conduction band states upon *p*- or *n*-doping, respectively.[22,132] Moreover, while the reduction of oscillator strength is proportional to the charge carrier density and therefore suitable for the determination of charge carrier densities,[22,26] the interaction of mobile excitons with charge carriers causes Auger quenching as a new non-radiative decay path.[14,24,27] The high mobility of excitons in SWCNTs makes this charge-mediated PL quenching process very efficient.[133,134] Therefore, the exciton PL intensity is reduced more rapidly than the absorption upon nanotube charging, with a non-linear dependence on charge carrier density.[135]

Furthermore, the excitonic E_{11} transitions in SWCNTs exhibit a shift towards higher energies upon nanotube charging. Spataru *et al.* suggested that the presence of charge carriers reduces the exciton binding energy by hundreds of meV as a consequence of dynamical screening effects from acoustic plasmons.[136,137] They explained the small overall impact on the exciton transition energy, which was experimentally found to blue-shift by only a few to several tens of meV,[24,26,138–140] with the simultaneous self-energy reduction (band gap renormalization) that reduces the impact of the strongly decreased exciton binding energy on the optical transition energy (see Equation (5)).

Recently, Hertel and coworkers argued that the high susceptibility of SWCNTs to their environment necessitates consideration of the presence of counterions, which accompanies several charging approaches such as redox- and electrochemical doping, for optical spectra analysis of charged nanotubes. They thus introduced a new model to explain the charging-

related observations in the framework of inhomogeneous charging, where the counterions remain in close proximity to the nanotubes due to poorly screened Coulomb interactions with the charge carriers on the nanotube, inducing perturbations to the electronic structure of the SWCNTs.[135,141,142] Charge carriers are localized at the resulting local potential traps. Upon diffusive encounter of these randomly distributed "charge puddles", excitons decay non-radiatively or form trions (see Section 2.2), causing charge carrier density-dependent exciton quenching. Moreover, the exciton wavefunction is confined to non-doped, intrinsic regions along the nanotube axis according to this model. The lengths of these segments are reduced with charging level, which is used to rationalize the observed dependence of the exciton blue-shift on charge carrier density.

2.1.6 Charge transport properties

The intrinsic charge transport properties of SWCNTs are defined by their DOS, diameter and chirality, whereas inter-tube transport presents an additional important parameter in nanotube networks. One factor contributing to the promising potential of SWCNTs for optoelectronic applications is their intrinsic ambipolar charge transport, originating from the nearly symmetric valence and conduction band.[54] This characteristic, combined with their narrow bandgap, leads to small injection barriers for holes and electrons when interfaced with commonly used electrode metals such as gold or palladium.[143] Consequently, the presence of both hole and electron conduction, providing possibilities for electroluminescence generation, is typical for SWCNT-based devices,[144,145] unless the nanotubes are modified by external doping.[12]

Charge transport in short and defect-free SWCNTS is ballistic.[146] Longer nanotubes, with lengths exceeding the electron mean free path (> 1 μm) exhibit diffusive band transport that is constrained by inelastic scattering with phonons or lattice defects.[61,87] Nonetheless, they maintain remarkably high single-nanotube field-effect mobilities of 10^3 – 10^4 $cm^2 (Vs)^{-1}$.[147] Theoretical and experimental research have shown that charge carrier mobilities decrease with increasing temperature due to the enhancement of phonon scattering rates.[147,148] Moreover, mobility is reduced in large- compared to small-bandgap SWCNTs because phonon backscattering is higher in small-diameter tubes.[147] For nanotube-based devices, large bandgaps can, however, be advantageous as they yield lower off-currents and may therefore give better on/off ratios (see Section 2.4).[149]

Furthermore, the charge carrier mobilities in both individual SWCNTs and networks exhibit a strong dependence on the charge carrier density, which is also attributed to the one-

dimensional DOS. Initially, the mobility increases with carrier density up to a maximum due to filling of the first subband, which reduces the number of available states for scattered charge carriers and consequently enhances the mobility.[91,147,150,151] As the first subband is occupied and the Fermi level enters the next subband, the sudden increase of unoccupied DOS leads to enhanced phonon scattering and, accordingly, a decrease in charge carrier mobility.[61,152] A second mobility maximum can be observed upon further increase in charge carrier concentration, achievable, *e.g.*, through electrolyte gating.[151]

Charge transport in SWCNTs is predominantly studied in field-effect transistors, and precise knowledge of the capacitance is necessary to reliably calculate charge carrier densities and mobilities (see Section 2.4). However, parallel-plate capacitor models that simply rely on the capacitance of the gate dielectric typically overestimate the gate-field capacitance due to both the nanotube open-network structure and their quantum capacitance, ultimately resulting in an underestimation of the mobilities.[153,154] The quantum capacitance of nanotubes can be considered as a serial component of the capacitance and needs to be accounted for as it is significantly smaller ($\sim 4 \cdot 10^{-10}$ F m^{-1})[155] than typical thin-film gate dielectric capacitances. It arises from the coupling of the one-dimensional nanotubes to the planar gate electrode and is proportional to the DOS at the Fermi level.[150] This intrinsic nanotube capacitance can be included in the experimental capacitance determination by measuring the on-state capacitance of the device, when the whole network is charged.[153]

SWCNT networks are highly relevant for electronic and optoelectronic devices due to their ease of processing and high on-currents. Charge transport in networks is, however, more complex since charge carriers cross multiple nanotubes on their trajectory between two electrodes. Consequently, the nanotube density, *i.e.*, interconnectivity, becomes a crucial parameter, and charge transport in sparse networks has been described with percolation models.[156,157] Yet, above network densities of 10 – 15 μm^{-1}, which are typically reached in networks for electronic applications, the percolation threshold is overcome and on-conductance and mobility saturate.[153,158]

The importance of inter-tube transport, associated with a junction resistance of 10^2 – 10^5 kΩ between adjacent SWCNTs[159–161] as compared to intra-tube resistances of ~ 10 kΩ μm^{-1} along individual SWCNTs,[147,161] is evident in the distinct temperature dependence of charge carrier mobilities in individual nanotubes and networks. While recent experimental studies[143,162–166] and theoretical models[167,168] suggest that contributions from intra-tube transport cannot be neglected, mobilities in networks of SWCNTs decrease towards lower temperatures in nanotube networks, opposite to the trend in individual nanotubes, as a consequence of the

reduced efficiency of the thermally activated inter-tube hopping transport.[143,162,163,169] The inter-tube junction resistance depends on the nanotube diameter and crossing angle,[170,171] the electronic type[159] and the presence of bundled nanotubes,[160,161] underscoring the importance of stable SWNCT dispersions with high selectivity for semiconducting species. Adjustment of the amount of wrapping polymer or surfactant may be necessary to ensure well-dispersed nanotubes without hindering charge transport, given that the presence of polymer potentially impedes inter-tube transport.[172,173] Although such an impact is still discussed,[174] it is advisable to remove any unbound dispersing agent from the dispersion before deposition of the nanotube networks, which can be achieved with minimal effort.

Residual polymer, the substrate and additional layers like an encapsulant or the gate dielectric in top-gated FETs affect the energetic landscape of nanotube networks and can directly influence inter- and intra-tube charge transport. Within individual nanotubes, charge scattering with surface phonons in highly polar environments such as silicon or hafnium dioxide strongly reduces the carrier mobilities.[166,175] It has moreover been reported that polar environments hinder inter-tube transport by inducing dipolar disorder from randomly oriented dipoles. This broadens the nanotube DOS, creating trap states that do not participate in inter-tube charge transport..[166,176] Additionally, the dielectric environment can introduce charge traps, further impeding charge transport. To mitigate the adverse effects of high-k dielectric materials in FETs while preserving high capacitances for low-voltage device operation, bilayer dielectrics have been established for nanotube network-based FETs.[177] These bilayers consist of a thin, low-k and trap-free polymer dielectric in direct contact with the nanotubes, combined with a high-k metal oxide on top.

2.2 Trions in single-walled carbon nanotubes

Trions are a common feature in the PL spectra of charged SWCNTs and display a red-shift by 100 – 200 meV compared to the exciton emission (see **Figure 2.6a**).[17,32] They can be described as bound states of two holes and one electron, or two electrons and one hole, as visualized in **Figure 2.6b**. Similar to excitons, they exhibit high binding energies and room-temperature stability due to the low dimensionality of carbon nanotubes.[178] In contrast to the bright exciton, trions exhibit a non-zero spin and are charged, offering potential for spin manipulation in carbon nanotubes through electric and magnetic fields,[37,38] as well as electrically driven trion conduction.[27] This section provides an overview of the creation and optical properties of trions in SWCNTs.

2.2.1 Trion formation

Initially predicted in 2009 by Rønnow and coworkers,[178] the first experimental evidence of room temperature-stable trions in SWCNTs was presented by Matsunaga[17] and Santos[18] *et al.* in 2011. Both methods employed optical excitation of SWCNTs in the presence of excess charge carriers. Matsunaga *et al.* utilized *p*-doping molecules to provide the necessary surplus holes, while Santos *et al.* created trions all-optically at high excitation densities, where an Auger-type process between two excitons produced free charge carriers. Since these initial studies, various approaches have been developed to induce trion PL from semiconducting carbon nanotubes. These methods include the optical excitation of redoxchemically,[17,22] electrochemically[23–26] or electrostatically[16,27,28] charged nanotubes. Furthermore, trion EL has been observed as a result of electrical excitation under ambipolar FET operation[24,29] and upon impact excitation.[30,31] The formation of trions at structural sp^3 defects has also been suggested,[140,179–181] whilst other studies only observed a rapid charge carrier-induced quenching of defect state photoluminescence[13,164] (see Section 2.3 for details on luminescent defects in SWCNTs).

Positive and negative trions form when a diffusing exciton encounters a hole or an electron, respectively. The localization of the charges involved in trion generation has been hypothesized,[18,141] and it was suggested that the resulting trions may likewise be localized at

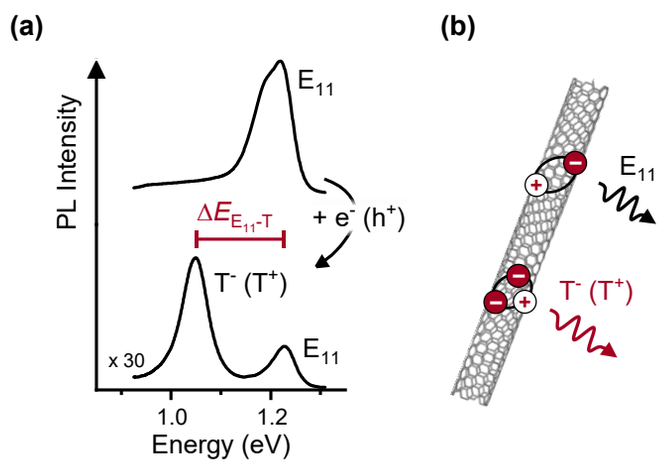

Figure 2.6: a) PL spectrum of a pristine (6,5) SWCNT network in a field-effect transistor (top), which displays exciton (E_{11}) emission, and of the same nanotube network after charging (bottom), exhibiting an additional negative (positive) trion peak T^- (T^+) and strongly reduced PL intensity. The exciton-trion separation is indicated in red. b) Schematic of a carbon nanotube with excitons (top) and trions (bottom).

electrostatic potential fluctuations.[139,182] Recent investigations indicate a correlation between localization and the charging scheme of the SWCNT, discriminating between homogeneous and inhomogeneous charging.[22,141] Inhomogeneous charging, *e.g.*, using redox chemistry, introduces counterions in proximity to the nanotube surface (see Section 2.1.5) and is expected to induce charge- and trion-trapping, whereas homogeneous charging strategies would result in reduced localization. In any case, the diffusive trion formation process competes with carrier-induced Auger quenching of excitons, resulting in a concomitant reduction of PL intensities (see **Figure 2.6a**).[183,184] Several studies reported timescales ranging from multiple tens of femtoseconds[185,186] to a few picoseconds[183,184] for diffusive trion formation, and the process was found to accelerate with increasing carrier concentration.[185] Nishihara *et al.* proposed that trions are not formed directly from the bright exciton, but through the energetically lower-lying dark exciton state (see **Figure 2.7**),[184,187] however, other studies have provided less conclusive evidence.[24,188] In early theoretical studies, Watanabe and Asano proposed that trions consist of a dark triplet exciton and an additional positive or negative charge carrier.[189]

It has been proposed that trions can be directly excited from the charged ground state since the absorption spectra of SWCNTs in the presence of surplus charges exhibit an additional red-shifted band. While several photophysical studies exist that corroborate this

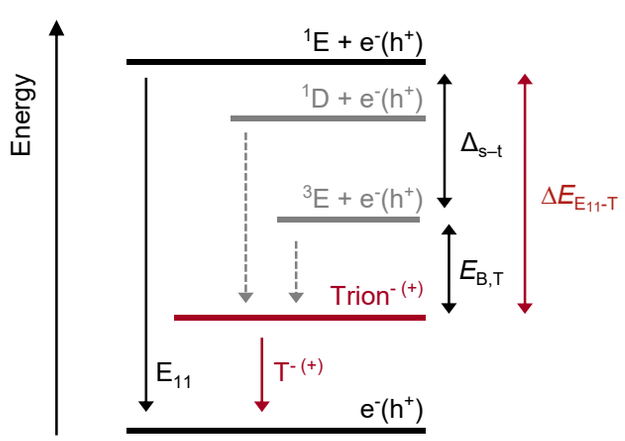

Figure 2.7: Proposed energy levels and bright exciton and trion emission in charged SWCNTs (note that some studies argue that the ground state of the exciton and trion manifold are decoupled).[135,141] The splitting Δ_{s-t} between the bright singlet (^{1}E) and the triplet (^{3}E) exciton and the trion binding energy $E_{B,T}$, that is, the difference between lowest exciton (^{3}E) and trion state, contribute to the exciton-trion energy separation ΔE_{E11-T}. Potential trion formation paths through the dark (^{1}D) singlet or the triplet exciton are still debated and visualized as grey dashed arrows.

hypothesis,[17,23,26,38,139,141,183,185] other investigations suggest that the additional absorption feature arises from an exciton-polaron state that can transform into a trion.[39,54,190]

2.2.2 Optical properties of trions

The experimentally observed energy difference between trion and exciton emission is significantly larger than the trion binding energy $E_{B,T}$ that was predicted in initial theoretical calculations.[21] Matsunaga *et al.* provided an explanation for this discrepancy by suggesting that strong short-range Coulomb interactions in the nearly one-dimensional nanotubes lead to non-negligible singlet-triplet splitting $\Delta_{s\text{-}t}$, which contributes to the energy separation $\Delta E_{E11\text{-}T}$ between trion and exciton PL (see **Figure 2.6a** and **Figure 2.7**).[17] Moreover, minor variations in the trion binding energies of positive and negative trions have been observed[23,24] due to the small difference in effective hole and electron masses.[23,191] Neglecting these mass effects, the exciton-trion separation can be represented by

$$\Delta E_{\mathrm{E_{11}\text{-}T}} = E_{\mathrm{B,T}} + \Delta_{\mathrm{s\text{-}t}} = \frac{\mathrm{A}}{d} + \frac{\mathrm{B}}{d^2}. \tag{6}$$

A and B are constants that parameterize the trion binding energy[189] and the singlet-triplet splitting,[17,23,105] which scale inversely with the tube diameter d and inversely with the square of the tube diameter, respectively. Accordingly, the energy spacing between exciton and trion increases for small-diameter tubes. A range of experimental values for A and B of A = 40 – 105 meV·nm and B = 48 – 70 meV·nm^2 has been reported and the variations have been attributed to the dependence of both parameters on the dielectric environment.[17,18,23,27,29,192] In general, if dielectric screening is reduced in a low-k environment, the trion binding energy and singlet-triplet splitting increase.[35,36]

Trion lifetimes are shorter than exciton lifetimes. Lifetimes of few picoseconds[39,184,186] to several hundred femtoseconds[38,135,185] have been reported. An extracted effective radiative lifetime of around 20 ns[38] indicates the dominance of non-radiative decay channels in trion decay. Koyama *et al.* observed a dependence of trion decay times on the charge carrier density, which they attributed to Auger processes between trions and external charge carriers.[185] They further concluded a significant nonradiative contribution by internal Auger recombination, that is, electron-hole recombination within the trion under ejection of the third charge carrier.

2.3 Oxygen defects in single-walled carbon nanotubes

Shortly after the first observations of photoluminescence from well-dispersed, semiconducting carbon nanotubes, non-radiative quenching of the highly mobile excitons at nonradiative lattice defects and tube ends was identified as the main cause of their low PLQY,[9,114] and efforts were made towards the development of protocols for the preparation of high-quality nanotubes with low defect density.[11] In contrast to that, Ghosh *et al.*[19] and Piao *et al.*[20] demonstrated that specific lattice defect configurations, introduced through controlled functionalization of SWCNTs with oxygen or aryl sp^3 moieties, cause additional emission features in the SWCNT PL spectra. These luminescent defects exhibit emission that is red-shifted from the E_{11} emission and can be conceptualized as zero dimension-like states below the free exciton state that are capable of trapping the mobile exciton and thus prevent diffusive quenching within the exciton lifetime. Therefore, luminescent defects bear the potential of substantial luminescence enhancement.[20] Many studies have been devoted to exploring and expanding their applicability in various optical and optoelectronic applications like single-photon emission, optical sensing and bioimaging, as reviewed elsewhere.[49–52] Compared to oxygen defects, sp^3 defects offer greater versatility in tuning PL characteristics, such as emission energy, and interactions with external analytes due to the possibility of tailored attachment of specific molecular moieties. However, oxygen defects often require less sophisticated preparation protocols, which can make them experimentally more accessible.

This section covers the basic concepts and theories behind luminescent defects in SWCNTs, with particular emphasis on oxygen defects and the impact of specific oxygen defect configurations on the PL properties. The section concludes with an overview of methods for the introduction of oxygen defects developed to date. Note that some of the models describing covalent defects have initially been established for sp^3-functionalized nanotubes, but are applicable to oxygen defects since their spectroscopic properties are based on a common physical mechanism.[45]

2.3.1 Optical properties of luminescent defects

Luminescent defects introduce significant sp^3 character into the otherwise nearly sp^2-hybridized carbon atoms in the nanotube lattice. This causes a local symmetry breaking at the defect site, which lifts the K and K' valley degeneracy.[193] Thus, the zero-momentum bright and dark excitons, E_{11}(B) and E_{11}(D), that are nearly degenerate in pristine SWCNTs with an energy difference of around 5 meV, split into a lower-energy, stabilized E_{11}* state and a higher-energy,

destabilized E_{11}^{up} state (see **Figure 2.8a**).[19] The ground state also splits. Since the optically active E_{11}^* state lies significantly below the bright exciton state (~ 100 meV), an exciton sampling the SWCNT length and encountering a defect (see **Figure 2.8b**) will be localized in the E_{11}^* state within picoseconds even at room temperature.[194] The trapped exciton can decay radiatively with an energy that is lowered with respect to the free exciton emission by the optical trap depth ΔE_{opt} as a consequence of the splitting of ground and excited state (see **Figure 2.9a**). Trap density-dependent energetic relaxation by up to 100 meV as a result of trapping-induced local reorganization of the excited-state SWCNT geometry has been proposed as an additional contribution to the lowering of the emission energy,[195,196] but remains tentative with the small experimental defect Stokes shift of ~ 20 meV contradicting this notion.[197] The optical trap depth correlates with the free exciton energy, that is, the inverse nanotube diameter.[20,42,198]

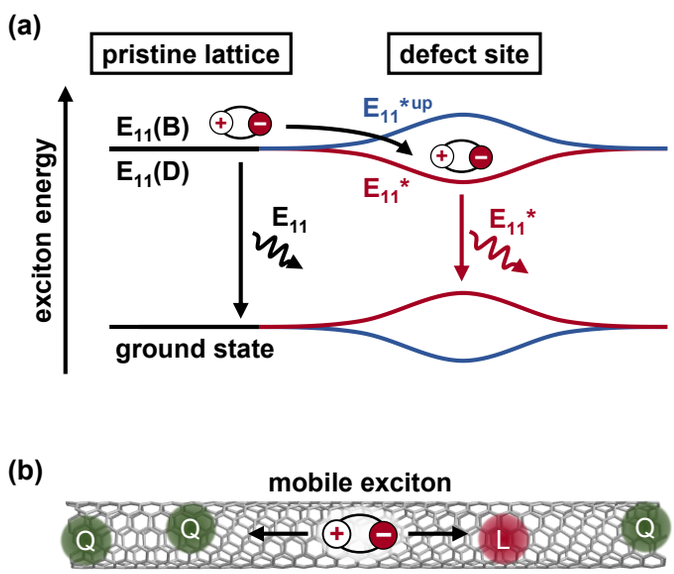

Figure 2.8: a) Perturbation of the ground and lowest exciton states upon functionalization with oxygen or sp^3 defects, and radiative relaxation in the pristine nanotube lattice and the defect site. States of the same parity are indicated by the same color (blue/red). b) An exciton diffusing along the nanotube can encounter a quenching site (Q) or a luminescent (L) defect.

In addition to the vertical optical transition, the trapped exciton can de-trap in a thermal process (**TD**, see **Figure 2.9b**).[196] The corresponding thermal trap depth ΔE_{therm} is substantially smaller than the optical trap depth and is expected to resemble more closely the actual depth of the trap potential. This actual trap depth is expected to directly influence the degree of exciton localization and exciton relaxation dynamics.[196] Furthermore, the existence

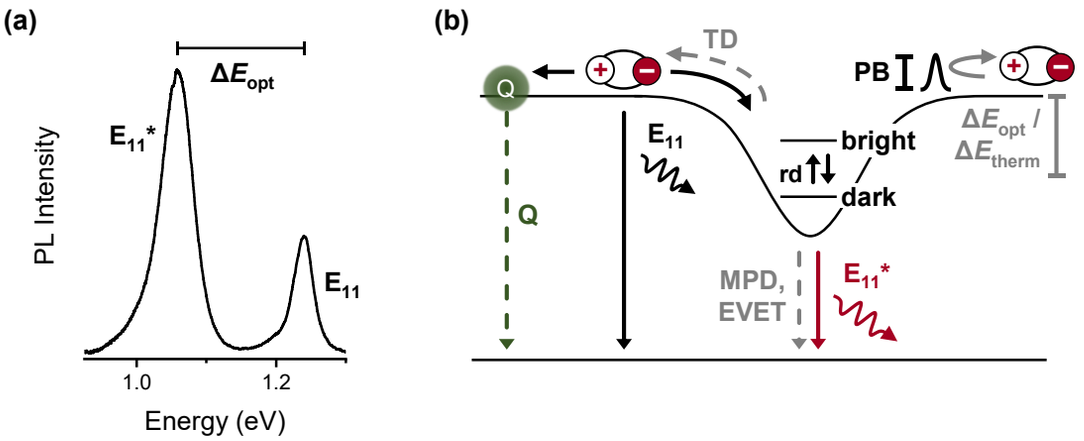

Figure 2.9: a) PL spectrum of defect-functionalized (6,5) SWCNTs. b) Exciton dynamics in oxygen defect-functionalized SWCNTs according to He *et al.*[200] and Kim *et al.*[199] (Q – quenching, TD – thermal detrapping, rd – redistribution between bright and dark states, MPD – multi-phonon decay, EVET – electron-to-vibrational energy transfer, PB – potential barrier). Radiative and non-radiative decay paths of localized excitons are indicated by solid red and dashed grey lines, respectively.

of fluctuating potential barriers (**PB**) of 3 – 22 meV next to the trap sites can affect the exciton trapping and de-trapping dynamics particularly at low temperatures.[195,199]

The absence of diffusive exciton quenching (**Q**) upon exciton localization strongly increases the PL lifetime of defect states (multiple 100 ps for defects compared to E_{11} lifetimes of around 10 ps)[198,201] and is responsible for the significant PL brightening.[20,201] Importantly, the quality of the pristine nanotubes affects the magnitude of such localization-induced PL enhancement since emission quenching is caused by excitons diffusively encountering non-luminescent structural defects or nanotube ends.[202] Accordingly, the strongest rise in PLQY upon functionalization was found for short SWCNTs, which exhibit a high probability of excitons traveling to the PL-quenching nanotube ends within their lifetime, and for nanotubes with large amounts of lattice imperfections that could arise, *e.g.*, from a harsh dispersion process.[197,203]

Efficient defect PL is observed already at rather low defect densities of 5 to 10 per µm.[20] In this low-density regime, the PLQY increases with defect density up to a maximum. Higher defect densities cause severe nanotube lattice perturbation and π-system disruptions that reduce the luminescence drastically.[42] It was further suggested that the homogeneity of defect distribution along the SWCNT influences the luminescence brightening.[204] Due to the low defect densities required to observe brightened PL from functionalized nanotubes, the shape of the corresponding absorption spectra closely resembles the pristine absorption profile with

some broadening and reduction of oscillator strength.[19,201,205] Furthermore, absorption by the defect state is weak due to the low defect density and could only be observed in samples of very high chiral purity and high SWCNT concentration.[42,197,205]

While defect-trapped excitons, in contrast to free excitons, are not available for diffusive quenching, they can undergo other non-radiative decay pathways (see **Figure 2.9b**) that have been identified through systematic investigation of the effects of nanotube chirality,[20,198] trap depth,[198] environment[200] and temperature.[196] Due to the enhanced exciton-phonon coupling upon exciton localization,[134] multi-phonon decay (**MPD**) becomes relevant as a non-radiative relaxation pathway.[198] MPD is enhanced as fewer phonons are required to bridge the optical gap. Thus, comparing the same defect types on different nanotube chiralities, the defect lifetimes and PL emission efficiencies decrease with increasing SWCNT diameter.[42,198] Furthermore, electron-to-vibrational energy transfer (**EVET**), a type of Förster resonance energy transfer, reduces defect emission from functionalized SWCNTs that are dispersed in a solvent or matrix.[200,206] The efficiency of the energy transfer from the defect state to adjacent molecules depends on the spectral overlap of the molecular absorption and the low-energy defect emission, which is typically given for the infrared-active vibrational modes of polar solvents like water. Finally, thermal up-conversion of the localized exciton into the free E_{11} state by means of the above-discussed thermal detrapping (**TD**) represents a third mechanism with significant impact on the lifetime of trapped excitons.[200]

Notably, a manifold of defect states exists of which only one is bright, similar to free excitons. In case of oxygen defects, a dark state is located 6 to 15 meV below the bright state, reducing defect state PL efficiency especially at low temperature.[196,201] The presence of dark states also influences the defect-state decay characteristics, which is biexponential with a short lifetime component resulting from the fast redistribution (**rd**) between the bright and dark states[198] and a long lifetime component that mainly consists of the above-mentioned three non-radiative decay pathways together with the radiative decay.[200]

Importantly, the quantum dot-like defects can only host one exciton at a time,[206] allowing for single-photon emission from luminescent defects states at room temperature.[46,47] This two-level character, together with the long defect state lifetimes of several 100 ps compared to the fast defect-state population within around 10 ps further causes a rapid trap-state filling and thus non-linear pump-power dependence of defect PL, that is, a decrease in defect/free exciton emission ratio with increasing excitation density.[45] Therefore, absolute defect quantification through emission profile characterization is unreliable across different experimental setups. Raman D/G^+ ratios have proved useful to quantify absolute defect

densities for sp^3 defects instead (see Section 3.2.4),[207] and similar correlations might exist for oxygen defects in nanotubes.

2.3.2 Role of the oxygen defect configuration

Oxygen defects entail an oxygen atom binding to two adjacent carbon atoms within the nanotube lattice. The precise configuration determines the trapping potential and consequently influences spectroscopic properties such as emission energy (see **Figure 2.10**).[19,195] The defect can be oriented along a C-C bond that is either parallel (l) or perpendicular (d) to the nanotube axis. Moreover, the functional oxygen group can exhibit ether- or epoxide-character. According to computational studies and supported by experimental results, the ether-d configuration presents the most stable form of oxygen defect configurations.[19,195]

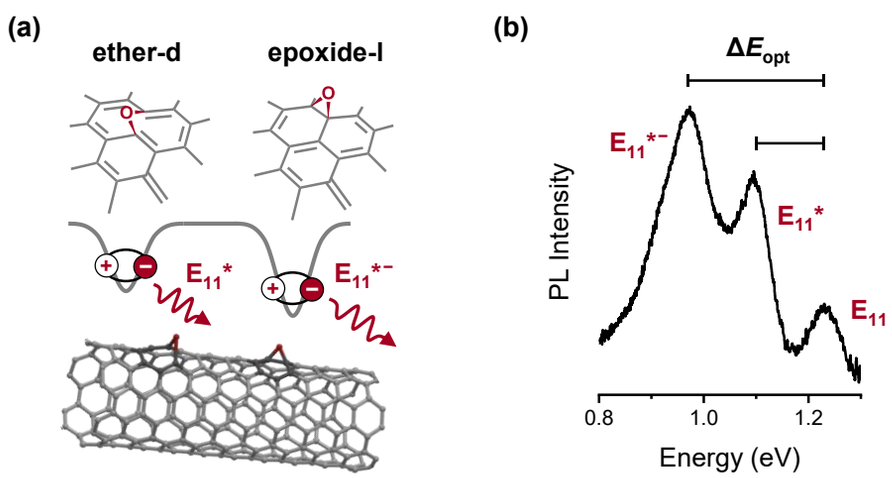

Figure 2.10: a) Ether-d and epoxide-l defect configurations with the corresponding trapping potentials and E_{11}^* and E_{11}^{*-} emission. b) PL spectrum of a (6,5) SWCNT network functionalized with both defect configurations. The horizontal bars indicate the optical trap depths ΔE_{opt} of the E_{11}^* and E_{11}^{*-} transitions, respectively.

The oxygen-bound carbon atoms possess a higher sp^3 character in the epoxide than in the ether configuration.[19] Besides the defect-bridged C-C bond, the carbon lattice bonds neighboring the epoxide defect also experience elongation. The preservation of a higher sp^2 character for the carbon atoms binding to the ether defect results in a smaller perturbation of the lattice, as only the distance between the oxygen-bound carbon atoms increases. Consequently, the red-shift of the trapped exciton with respect to the free exciton emission is

less pronounced for ether compared to epoxide defects.[19] Accordingly, oxygen-functionalized (6,5) SWCNTs exhibit ether-d defect PL at around 1.11 eV (1120 nm) and epoxide-l emission at around 0.99 eV (1250 nm), corresponding to optical trap depths of 130 and 300 meV, respectively.[46,208] Due to this difference in ΔE_{opt}, variations in decay dynamics and low-temperature behavior can be expected, similar to findings in aryl-functionalized nanotubes featuring distinct defect configurations and trapping potentials.[42] Currently, however, there are few comparative studies specifically exploring differences between the two oxygen defect configurations.[46]

2.3.3 Oxygen functionalization strategies

Multiple strategies towards oxygen functionalization of SWCNTs, mainly in aqueous dispersion, have been developed since the first report in 2010.[19,209] Oxygen-containing reactive species (reactive oxygen species, ROS) such as hydroxyl, superoxide or oxygen radicals, formed through dissociation of a precursor molecule, were proposed to react with the sp^2-hybridized carbon nanotube lattice.[40,46,205,210,211] The exact nature of the ROS initiating the functionalization reaction, however, has been poorly investigated to date. The majority of methods preferentially yields the most stable ether-d oxygen defect type. The concomitant occurrence of the epoxide-l configuration has also been observed,[46,208,212,213] which underscores the sensitivity of defect introduction to external influences. Yet, a systematic understanding of the factors contributing to the preferred formation of a certain defect configuration remains elusive.

The very first and to date most-applied method for oxygen defect introduction exposes SWCNTs to ozone-enriched water and white light for several hours.[19] Following this approach, ten different nanotube chiralities were successfully functionalized. For nanotubes with smaller diameter, higher reactivities were observed due to the inherently higher strain in the more strongly curved bonds.[19,41,42] The ozonization reaction primarily produced a distinct defect configuration. Calculations suggested the formation of an ozonide adduct followed by a Criegee rearrangement to the epoxide-l configuration under loss of molecular oxygen. Irreversible photoisomerization is expected to yield the most stable ether-d defect type.[19]

Oxygen functionalization of SWCNTs using alternative oxidizing agents has also been tested.[19,205,210,214] Factors like redox potential, absorption cross section and the possible creation of insoluble byproducts were found to determine the efficiency and applicability of these oxidants.[19,205] The nanotube surface coverage, which depends on the type and concentration of the surfactant, was identified as another factor determining the efficiency of the

functionalization reaction in these studies.[205,210] For sodium hypochlorite as oxidant, activated through irradiation with UV light (300 nm), a particularly high selectivity towards the ether-d configuration and a strong PL brightening has been observed.[204,205] From the relatively small increase of Raman D/G^+ ratios, the authors inferred that low numbers of nonradiative defects are created in this process. It was suggested that oxygen atoms created through photodissociation of hypochlorite form oxygen defects on the nanotubes within a single step, in contrast to multi-step reactions whose intermediates (*e.g.*, ozonide adduct) could undergo competing reactions into nonradiative structural lattice defects. The ozone-free sodium hypochlorite approach further enabled the application of a continuous flow reactor to prepare milligram quantities of oxygen-functionalized SWCNTs.[205]

While most reported protocols rely on the use of precise quantities of oxidants that are added to the SWCNT dispersions, a method for oxygen functionalization that is experimentally less demanding has been developed by Xhyliu *et al.*[215] This solution-based strategy employs ambient molecular oxygen, activated with UV light (254 nm), as the only reactant to produce SWCNTs with oxygen defects in ether-d configuration.

Solid-state approaches to oxygen defect introduction may further reduce the experimental efforts related to wet-chemical synthesis. To date, few such methods have been developed. UV-ozone irradiation of an SWCNT filter cake[213] and electron-beam deposition of various oxides (SiO_2, Al_2O_3) onto nanotube networks[46,208] yielded luminescence from both the ether-d and the epoxide-l configuration. The oxide layers additionally served as encapsulants for the SWCNTs, resulting in particularly high photostability, which is essential for room-temperature single-photon emission.[46,208] However, the electron-beam process may impede efficient upscaling and restrict flexibility for post-treatment of the SWCNTs due to the encapsulating oxide layer. Reduction of experimental confinements and potential defect introduction with spatial resolution[53] thus motivate the development of a new solid-state method for oxygen defect introduction in this thesis.

2.4 Field-effect transistors

This section introduces the field-effect transistor (FET) layout and working principle. FETs are electronic devices where the flow of current through a semiconductor between two electrodes (source and drain) is regulated by an external electric gate field. As such, they offer the potential of controlled accumulation of charge carriers within a semiconductor and are

well-suited for investigating charge transport in semiconducting materials.[54] Some semiconductors can only transport one type of charge carriers, *i.e.*, holes or electrons (unipolar *p*- or *n*-type transport), forming the basis for electronic logic circuits. Conversely, both charge carrier polarities can be induced in ambipolar materials like semiconducting SWCNTs, and when present at the same time, the recombination of holes and electrons can enable electroluminescence.[144,145] The accumulation of either one or both charge carrier types in SWCNTs in a transistor depends on external parameters like the electrode work function and the presence of intentionally or unintentionally introduced dopants. For instance, water and oxygen molecules are common unintentional dopants which impede electron transport.[216] Moreover, the applied voltages define the operation of SWCNT FETs as ambipolar, purely *n*- or purely *p*-type transistors, with the unipolar carrier accumulation modes being utilized in Chapter 4. Therefore, this section focusses on ambipolar FETs in top-gate bottom-contact geometry under unipolar device operation.

2.4.1 Device layout

In a typical thin-film FET, a semiconducting layer of few to several tens of nm thickness connects the source and drain electrodes, enabling gate-controlled electrical current between them. The source and drain electrodes, which exhibit arbitrary widths and are typically

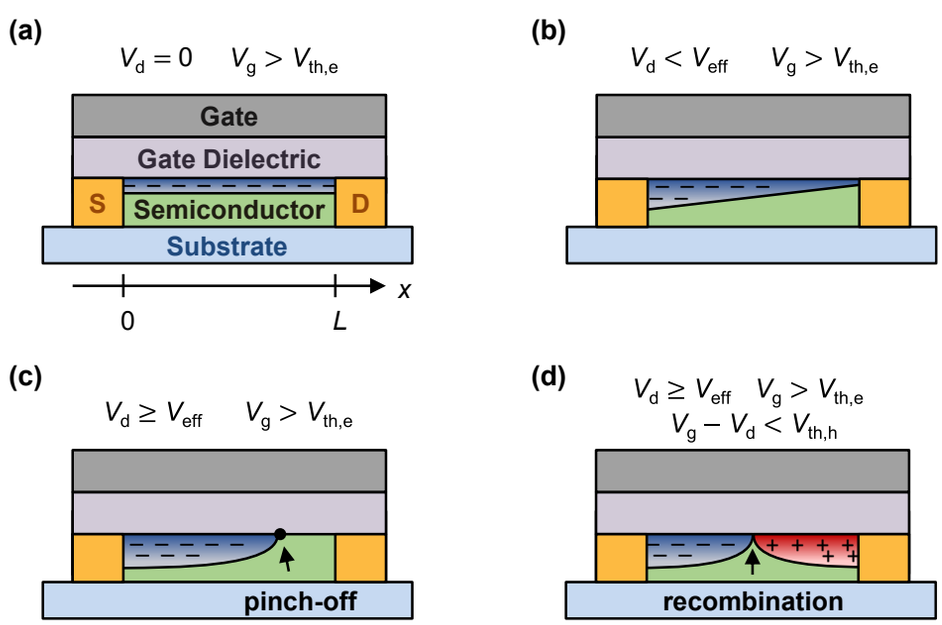

Figure 2.11: Schematic illustration of a top-gate/bottom contact FET operated in the a) accumulation, b) linear, c) saturation and d) ambipolar regime.

separated by a few to several tens of μm, determine the length L and width W of the transistor channel. An insulating layer, termed gate dielectric, separates the semiconductor and the gate electrode.[217] A schematic thin-film transistor featuring a top-gate bottom-contact geometry, which is employed in this thesis with a (6,5) SWCNT network as semiconducting layer, is shown in **Figure 2.11**. Alternative geometries with differing characteristics, resulting from the distinct relative positions of electrodes and channels, as well as different interfacial effects, may be employed depending on the specific requirements.[216,218] Yet, the underlying working principle remains the same across all geometries: The source electrode is typically grounded (source voltage V_s = 0 V). When a gate voltage V_g is applied between the gate electrode and the source electrode, a conductive (active) channel, characterized by the channel length L and the channel width W, forms as a result of charge carrier accumulation at the interface of the semiconductor and the gate dielectric. An electric field between the source and drain electrodes, exerted through the source-drain voltage V_d, induces charge transport within the active channel. The current conducted between the source and drain electrode is referred to as drain current I_d, while the current passing through the dielectric is termed gate current or gate leakage current I_g.

2.4.2 Operating principle

The FET device performance is typically assessed through two types of measurements, that is, output and transfer curves. Output characteristics provide the relationship between I_d and V_d at a constant gate bias V_g (see **Figure 2.12a**). Conversely, in transfer curves, the source-drain voltage V_d remains constant while the variation of I_d with V_g is recorded (see **Figure 2.12b**). Here, while using electron transport as an example, the principles remain the same for hole transport, although with negative voltages.

First, the output curves are derived to showcase the different operating regimes. The unipolar FET operation can be classified into three regimes, that is, the accumulation, linear and saturation regime. These regimes are accessed by selection of the distinct gate and drain voltages. At drain voltage V_d = 0, the FET is operated in the accumulation regime and behaves like a metal-insulator-semiconductor (MIS) capacitor (see **Figure 2.11a**). When a gate voltage is applied, electrons accumulate within the semiconductor at the interface with the gate dielectric.[91,219] Below the threshold voltage for electrons $V_{th,e}$, these electrons occupy trap states that originate from the semiconductor material itself, impurities, or the semiconductor-dielectric interface. Once the applied gate voltage exceeds threshold voltage ($V_g > V_{th,e}$), the majority of electrons is mobile, forming the so-called conductive channel with a typical

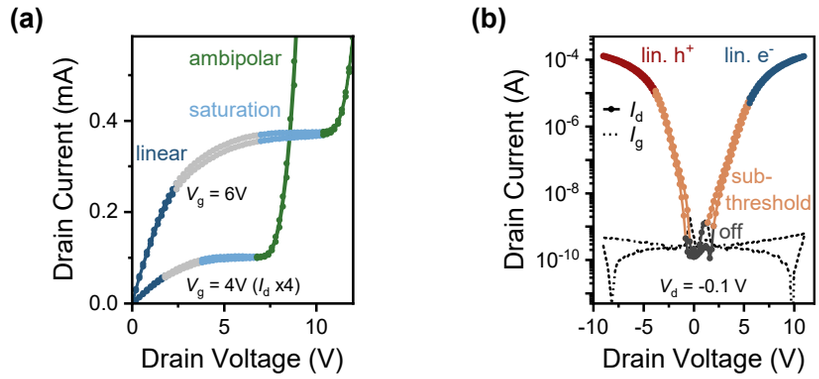

Figure 2.12: a) Output and b) transfer characteristics of a top-gate/bottom contact FET with a (6,5) SWCNT network as semiconductor. The forward and reverse gate voltage sweep exhibit negligible current hysteresis. The distinct transistor operating regimes are marked with different colors.

thickness of a few nanometers, and the drain voltage increases pronouncedly. The onset of mobile charge carrier accumulation can be defined by an effective gate voltage expressed as $V_{\mathrm{eff}} = V_{\mathrm{g}} - V_{\mathrm{th,e}}$. The areal density of mobile charge carriers Q_{mob} is determined not only by V_{g} and $V_{\mathrm{th,e}}$, but also by the area-specific capacitance C_{i} of the MIS capacitor:

$$Q_{\mathrm{mob,e}}(\mathrm{x}) = C_{\mathrm{i}} \cdot \left(V_{\mathrm{g}} - V_{\mathrm{th,e}}\right) = C_{\mathrm{i}} \cdot V_{\mathrm{eff}} \tag{7}$$

Thus, an FET layout enables the introduction of gate-tunable hole and electron densities into the semiconductor, which is utilized in Chapter 4 of this thesis. Typical maximum charge carrier densities range from 10^{12} to 10^{13} cm^{-2} in FETs with a hybrid gate dielectric consisting of a polymer and an oxide layer[164,177] (see Sections 3.1.3 and 4.2 for further information on hybrid gate dielectrics).

A small bias V_{d} applied between source and drain electrode such that $V_{\mathrm{d}} \ll V_{\mathrm{eff}}$ generates a potential gradient in the channel, inducing current flow when $V_{\mathrm{g}} > V_{\mathrm{th,e}}$ (see **Figure 2.11b**). The distribution of mobile charge carriers along the transistor channel can be calculated from the potential $V(\mathrm{x})$ at each channel position $\mathrm{x} \in [0; L]$ as

$$Q_{\mathrm{mob,e}}(\mathrm{x}) = C_{\mathrm{i}} \cdot \left(V_{\mathrm{g}} - V_{\mathrm{th,e}} - V(\mathrm{x})\right) \tag{8}$$

under the approximation of a linearly increasing local channel potential from $V(\mathrm{x}) = 0$ at the source ($\mathrm{x} = 0$) to $V(\mathrm{x}) = V_{\mathrm{d}}$ at the drain electrode ($\mathrm{x} = L$).

The current between source and drain can be determined within the graduate channel approximation,[216] which implies that the gate field greatly exceeds the electric field between

source and drain electrode and can be assumed if the length of the transistor channel is significantly larger than the thickness of the gate dielectric,[220] and considering two-dimensional transport. Specifically, I_d is calculated using Ohm's law according to

$$I_{d,e} = \frac{W \cdot C_i}{L} \cdot \mu_e \cdot \left(\left(V_g - V_{th,e}\right) \cdot V_d - \frac{V_d^2}{2} \right) \tag{9}$$

when recognizing drift diffusion as the only mode of transport and assuming mobility μ to be independent of the charge carrier concentration. In the above-mentioned case of a drain voltage that is small compared to the gate and effective voltage, this relationship simplifies to

$$I_{d,e}^{lin} = \frac{W \cdot C_i}{L} \cdot \mu_{lin,e} \cdot \left(V_g - V_{th,e}\right) \cdot V_d \,. \tag{10}$$

For $V_d \ll V_{eff}$, the drain current depends linearly on the applied drain voltage and the corresponding voltage range is accordingly referred to as the linear operation regime (see **Figure 2.12a**).

Keeping a constant $V_g > V_{th,e}$, a further increase of the drain voltage to $V_d = V_{eff}$ results in the formation of a carrier depletion zone at the charge carrier density pinch-off position x, where $V(x) < V_{th,e}$ (see **Figure 2.11c**). From thereon, the saturation regime is reached since the drain current does not increase any further with V_d (see **Figure 2.12a**). The drain current can then be expressed as

$$I_{d,e}^{sat} = \frac{W \cdot C_i}{2L} \cdot \mu_{sat,e} \cdot \left(V_g - V_{th,e}\right)^2 . \tag{11}$$

In case of ambipolar FETs, like the SWCNT-based transistors in this thesis, an ambipolar charge transport regime exists beyond the saturation regime (see **Figure 2.11d**).[217] This regime, in which both holes and electrons are present in the transistor channel, is entered by further increasing the drain voltage while maintaining a constant gate voltage above $V_{th,e}$, so that the threshold for hole injection from the electron drain electrode is surpassed ($V_g - V_d < V_{th,h}$). Beyond the saturation plateau, the drain current increases superlinearly with the drain voltage, in contrast to unipolar devices (see **Figure 2.12a**).

While output characteristics enable the assignment of the three different operating regimes, the transfer curves are useful for assessing the device performance with metrics like the charge carrier mobility μ, on/off ratio I_{on}/I_{off}, onset voltage V_{on}, and trap density N. The transfer characteristics of ambipolar transistors appear as a combination of the unipolar hole and electron curve at low drain voltages (see **Figure 2.12b**). Consequently, ambipolar FETs are in the off-state, characterized by the off-current I_{off}, in the absence of gate biasing. Holes

(electrons) are induced when a negative (positive) gate voltage is applied. The small V_d initiates current between the source and drain electrodes. Once V_g reaches the onset voltage V_{on}, the current surpasses the noise level of the FET ($I_d > I_g$)[221] and trap states are filled up to the threshold voltage V_{th}. The on-current (I_{on}) corresponds to the drain current value at which the current reaches its maximum, *i.e.*, does not notably increase with further increments in V_g.

The density of surface trap states N at a given temperature T can be calculated from the so-called subthreshold swing S, that is, the inverse of the slope in the subthreshold regime, as[222]

$$N = \left(S \cdot \frac{e}{k_B\, T \ln 10} - 1\right) \cdot \frac{C_i}{e^2} = \left(\frac{\partial V_g}{\partial(\log(I_d))} \cdot \frac{e}{k_B T \ln 10} - 1\right) \cdot \frac{C_i}{e^2}, \tag{12}$$

where k_B is the Boltzmann constant and e corresponds to the elementary charge.

Charge carrier mobilities are an important figure of merit for FETs since they define the maximum device switching speed as well as the source-drain current at fixed voltages.[223,224] The linear mobility can be extracted from the transfer characteristics in the linear regime by converting Equation (9) into

$$\mu_{lin} = \frac{L}{W \cdot C_i \cdot V_d} \cdot \frac{\partial I_d^{lin}}{\partial V_g}\ . \tag{13}$$

It is important to note that the charge carrier mobility does not present a material constant. Instead, it strongly depends on the semiconductor morphology, device layout and measurement conditions. Moreover, the expression is based on the gradual channel approximation assuming ideal device behavior. Factors like the contact resistance, which depends, *e.g.*, on the electrode material and film thicknesses,[225,226] are thus not included, but can be addressed subsequently.

In SWCNT network-based FETs, balanced hole and electron mobilities of 1 – 100 $cm^2\,(Vs)^{-1}$ and high on/off current ratios > 10^6 are typically observed.[81,227] Studies of the temperature and carrier concentration dependence of the electrical properties give valuable insights into the charge transport properties of semiconductors (see Section 2.1.6) and can also be used for transistor optimization.[81] Finally, FETs enable the introduction of precisely controllable densities of positive and negative charge carriers into ambipolar semiconductors, which was done in this thesis.

3. Experimental and characterization methods

This chapter provides an overview of the sample preparation and characterization techniques employed in this work. Basic experimental results are presented to make the described methods more accessible to the reader.

3.1 Materials, thin film and device preparation

3.1.1 Substrate preparation

For all thin-film experiments, alkali-free aluminum borosilicate glass (Schott AF32 eco, thickness 0.3 mm), cleaned *via* subsequent ultrasonication in acetone and isopropanol (Sigma Aldrich), served as the transparent substrates. The alternative substrate surfaces titanium dioxide (TiO_x), zinc oxide (ZnO_x) and divinyltetramethylsiloxane-*bis*-benzocyclobutene (BCB), utilized in Chapter 5, were created through spincoating or airbrush-spraying of the respective precursor molecules on the cleaned glass substrates and subsequent post-treatment as detailed in **Table 3.1**. Film morphologies and thicknesses were determined with atomic force microscopy (AFM, see Section 3.2.1) and profilometry (see Section 3.2.2).

Table 3.1: Substrate preparation. Materials and processing parameters.

Material	Precursor, Supplier	Deposition	Post-treatment
TiO_x	Solaronix Ti-Nanoxide BL/SC organotitanate	Spincoating: 1000 rpm (10 s) + 5000 rpm (20 s)	Sintering at 500 °C, 45 min
ZnO_x	$Zn(OAc)_2 \cdot 2\ H_2O$, Sigma Aldrich (99%)	Airbrush-spraying of 0.3 M solution in methanol on heated substrate (200 °C)	Rinsing with DI-water
BCB	Cyclotene 3022-35, micro resist technology GmbH	Spincoating of 1:4 dilution in mesitylene: 500 rpm (3 s) + 8000 rpm (60 s)	Cross-linking at 290 °C, 2 min

3.1.2 Dispersion and deposition of SWCNTs

Nearly monochiral dispersions of (6,5) SWCNTs in toluene (Sigma Aldrich) were obtained using a polymer-wrapping approach as described previously.[11] 50 mg CoMoCAT raw material, containing various SWCNT chiralities and amorphous carbon as a consequence of the synthetic process, was shear force-mixed together with 65 mg PFO-BPy in 140 mL of toluene for 72 h at 20 °C to selectively disperse the (6,5) chirality. The non-dispersed material was removed by two-times centrifugation at 60,000 *g* for 45 min and subsequent filtration through a syringe filter with 5 μm pore size. The resulting stock dispersion is stable for several months as a consequence of the excess of PFO-BPy, which needs to be removed for further use of the dispersion. For that, the stock dispersion was filtered and the filter cake was washed in 10 mL toluene at 80 °C three times. Subsequently, the filter cake was redispersed in toluene at room temperature by bath sonication for 30 min. The UV-vis-NIR absorption spectra (see Section 3.2.3) exhibited distinct E_{11} and E_{22} absorption peaks and phonon sideband absorption of the (6,5) species, but no peaks from chiralities other than the (6,5) SWCNTs were observed (see **Figure 3.1a**) due to the high chiral purity. Weak absorbance from residual polymer, overlapping with the (6,5) E_{33} absorption, can mainly be attributed to the PFO-BPy wrapping the SWCNTs. The chiral purity was further confirmed by Raman spectroscopy (see Section 3.2.4). In the radial breathing mode (RBM) range, a single peak at 309 cm^{-1} was present (see **Figure 3.1b**), corresponding to (6,5) SWCNTs.

Networks of (6,5) SWCNTs were deposited from the redispersed nanotubes in toluene (E_{11} absorbance at 1 cm path length: 5 and 2 for Chapters 4 and 5, respectively) through spin-coating. Apart from the BCB-coated substrates, all substrates were treated with UV/ozone

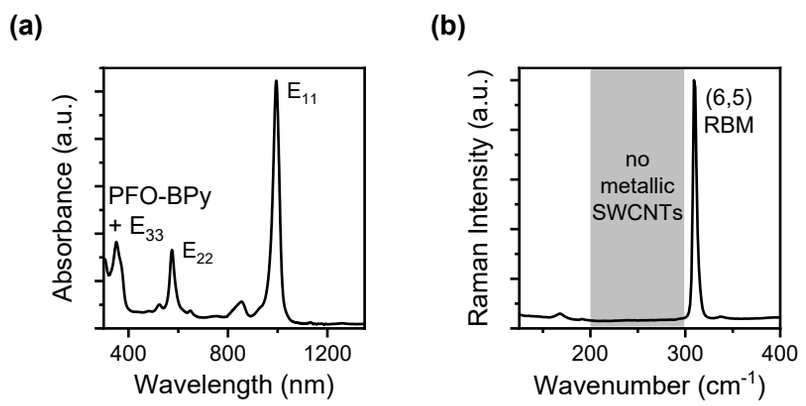

Figure 3.1: a) UV-vis-NIR absorption spectrum of a (6,5) SWCNT dispersion in toluene after removal of excess unbound PFO-BPy. b) Raman spectrum (532 nm excitation) of the dropcast stock dispersion in the RBM range.

(UV Ozone Cleaner E511, Ossila Ltd.) for 10 min prior to the deposition of the nanotubes. Homogeneous network densities were obtained by spincoating three times in air (2000 rpm, 30 s), and annealing at 90 °C for 2 min in between the spincoating steps. Excess polymer was removed in a final washing step with tetrahydrofuran (VWR International) and isopropanol, after which the samples were annealed at 90 °C for 4 min. The resulting networks were examined with atomic force microscopy (see Section 3.2.1). The average nanotube length was 1.2 ± 0.4 µm, and linear network densities of 30 and 10 nanotubes per µm were obtained for the experiments in Chapters 4 and 5, respectively. The type of underlying surface did not significantly affect the SWCNT network densities.

3.1.3 Fabrication of top-gate/bottom-contact field-effect transistors

Top-gate/bottom-contact field-effect transistors, comprised of gold bottom electrodes, random (6,5) SWCNT networks as the semiconductor layer, a hybrid bilayer gate dielectric and a silver gate electrode (see **Figure 3.2a**), were fabricated layer-by-layer on cleaned glass substrates (Schott AF32eco, 300 µm thickness, bath-sonicated in acetone and isopropanol for 10 min).

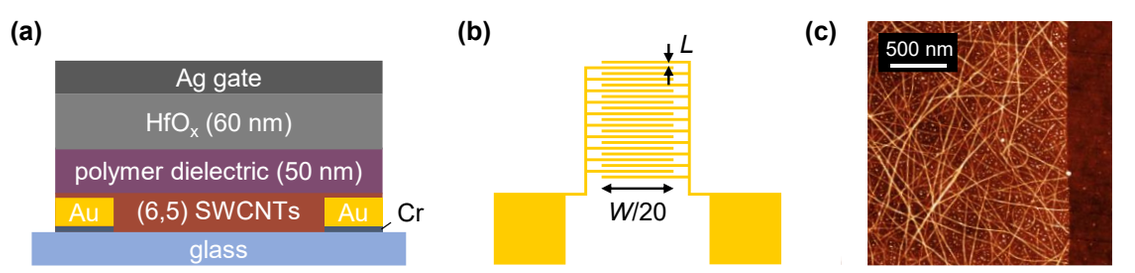

Figure 3.2: a) Schematic layout of an SWCNT network-based FET with a hybrid dielectric composed of selected polymers. b) Layout of interdigitated source and drain bottom electrodes. c) Representative AFM image of a photolithographically patterned (6,5) SWCNT network.

Interdigitated bottom electrodes as shown in **Figure 3.2b** (channel length L = 20 and 10 µm for dielectric variation and ttmgb-doped devices, respectively, with channel width W = 10 mm) were photolithographically patterned on the glass substrates in a cleanroom environment. The non-photosensitive LOR5B (MicroChem Corp.) was spincoated at 4000 rpm for 30 s and soft-baked at 185 °C for 4 min, followed by spincoating of the positive photoresist MICROPOSIT

S1813 (Dow Chemical Co.), which was deposited at 4000 rpm for 30 s and soft-baked at 115° C for 1 min. This double-resist approach allowed for the creation of an undercut in the subsequent 24 to 30 s of pattern development in the alkaline MICROPOSIT MF-319 developer (Dow Chemical Co.). Thus, the formation of metal spikes, which potentially lead to reduced breakdown strength or even shorting of the devices, was avoided in the consecutive electron beam evaporation (HVB-130, Winter Vakuumtechnik GbR) of the gold electrodes with an underlying chromium adhesion layer (30 nm gold, rate: 0.5 Å·s^{-1}, 2 nm chromium, rate: 0.2 Å·s^{-1}) and lift-off in *N*-methyl pyrrolidone (NMP). The electrode substrates were cleaned by bath sonication in acetone and isopropanol for 10 min, respectively.

Random (6,5) SWCNT networks were deposited by spincoating (see Section 3.1.2) and confined to the transistor channel area (see **Figure 3.2c**) with another photolithography step as described above, with the photoresist protecting the channel area during oxygen plasma etching (Nordson MARCH AP-600/30, 100 W, 2 min). Lift-off in NMP (30 – 60 min) removed the photoresist.

Prior to deposition of the polymer component of the hybrid dielectric, the substrates were annealed in dry nitrogen at 300 °C for 1 h to remove residual photoresist, water and oxygen molecules from the SWCNT networks. 50 nm thick layers of the polymer dielectrics poly-[4,5-difluoro-2,2-*bis* (trifluoromethyl)-1,3-dioxole-*co*-tetrafluoroethylene] (Teflon AF2400), poly-(vinylidene fluoride-*co*-trifluoroethylene-*co*-chlorotrifluoroethylene) (P(VDF-TrFE-CTFE), poly(methyl methacrylate) (PMMA) and polystyrene (PS) were deposited following **Table 3.2**. The morphologies and thicknesses of the thin films were determined with AFM and profilometry, respectively (see Sections 3.2.1 and 3.2.2).

Table 3.2: Polymer dielectrics. Materials and processing parameters.

Polymer	Supplier	Concentration, solvent, spincoating parameters	Annealing
Teflon AF2400	Sigma Aldrich	20 g L^{-1} in FluorInert FC-40 (3M): 4000 rpm (180 s)	50 °C (10 min) + 80 °C (30 min)
P(VDF-TrFE-CTFE) (Piezotech RT TS)	Piezotech Arkema	10 g L^{-1} in n-butanone: 1900 rpm (90 s)	80 °C (30 min)
PMMA (syndiotactic, MW = 315 kg mol^{-1})	Polymer Source	20 g L^{-1} in n-butyl acetate: 4000 rpm (30 s)	80 °C (30 min)
PS (atactic, MW = 230 kg mol^{-1})	Polymer Source	20 g L^{-1} in n-butyl acetate: 5000 rpm (60 s)	80 °C (30 min)

The (hybrid) dielectric was completed with a 60 nm thick layer of hafnium oxide (HfO_x) that was deposited through atomic layer deposition (ALD, Ultratech Savannah S100) using alternating pulses of the precursor tetrakis-(dimethylamino)hafnium (Strem Chemicals Inc.) and water at 100 °C. The HfO_x layer ensures stable transistor operation with high gate dielectric breakdown strengths and low gate leakage currents, and further shields the transistor channel from electron-trapping water and oxygen molecules, making the FETs operable in air without the need for additional encapsulation.[177] To finalize the devices, 30 nm silver was thermally evaporated (MB-ProVap 3G, M. Braun Inertgas-Systeme, rate: 0.2 $Å \cdot s^{-1}$ for the first 5 nm, then 0.5 $Å \cdot s^{-1}$) as the top-gate electrode through a shadow mask.

3.1.4 Trap removal and chemical doping of SWCNT networks for FETs

Selected samples of patterned and annealed (6,5) SWCNT networks on electrode substrates were chemically *n*-doped with 1,2,4,5-tetrakis(tetramethylguanidino)benzene (ttmgb) in dry nitrogen atmosphere.[143,228] The substrates were submerged in 3 or 6 $g \cdot L^{-1}$ solutions of ttmgb in anhydrous toluene for 20 min and subsequently annealed at 150 °C for 20 min. The hybrid gate dielectric and gate electrode completed the devices as described in Section 3.1.3.

3.1.5 Oxygen functionalization of SWCNT networks

Random (6,5) SWCNT networks deposited on photoreactive and unreactive reference substrates (see Section 3.1.1) were illuminated with a UV diode (Thorlabs, SOLIS-365C, 365 nm, 1.9 $mW \cdot mm^{-2}$) in ambient air or dry nitrogen (H_2O: 0.7 ppm, O_2: < 0.1 ppm), or with a green diode (Thorlabs, SOLIS-525C, 525 nm, 1.4 $mW \cdot mm^{-2}$) through a 500 nm long-pass filter for 15 min in dry nitrogen. A fresh substrate was used for each illumination condition and annealed at 150 °C for 30 min prior to illumination. For each exposure series, the individual substrates were obtained through cutting of a common parent substrate to ensure consistent SWCNT densities across the respective series. SWCNT networks with spatially confined oxygen defects were obtained by UV exposure for 30 min in dry nitrogen through a 60 μm thick metal shadow masks with circular holes of 60 μm diameter.

3.2 Characterization and data processing

3.2.1 Atomic Force Microscopy

The topography of the SWCNT networks was characterized by atomic force microscopy (Dimension Icon, Bruker Corp. in ScanAsyst mode). The cantilever holder (DAFMCH, Bruker Corp.) was equipped with a ScanAsyst tip (SCANASYST-AIR, Bruker Corp.). The acquired AFM images were processed (background levelling, line error correction) with the open-source software Gwyddion 2.45. A processed AFM image is presented in **Figure 3.2c**.

3.2.2 Profilometry

Layer thickness of the oxide and polymer films were measured with profilometry (DektakXT Stylus Profiler, Bruker Corp.). The respective single-layer films were created at the same time and under the same conditions as the films that were used for further processing and experiments. Apart from the HfO_x films, all thicknesses were determined by scanning across grooves that were scratched into the films. In case of HfO_x, the reference substrates were partially covered with photoresist prior to oxide deposition *via* ALD (see Section 3.1.3, the reference and FET samples were coated simultaneously). The height samples underwent a subsequent lift-off in NMP overnight and the film thicknesses were measured across the photolithographically patterned trenches.

3.2.3 Absorption spectroscopy

Absorption spectra were recorded in the UV-vis-nIR spectral range (300 – 1650 nm) using a Varian Cary 6000i absorption spectrometer equipped with a silicon (175 – 800 nm) and an InGaAs (800 – 1800 nm) detector. Dispersions were measured in quartz glass cuvettes with 1 cm path length (Hellma Analytics, QS material). All spectra were baseline-corrected with the absorption of the pure solvent-containing cuvette. Spectra of films on glass substrates were collected using a custom sample holder. The background correction was performed with a pristine glass substrate.

3.2.4 Raman microscopy

Hyperspectral Raman maps of (6,5) SWCNT networks were collected using a Renishaw inVia Reflex confocal Raman microscope and near-resonant excitation at 532 nm (grating: 2400 lines mm^{-1}). The system was calibrated to a silicon standard (520.6 cm^{-1}) prior to each measurement series. A typical Raman spectrum of a (6,5) SWCNT network is presented in **Figure 3.3**. The radial breathing mode occurs in the low-frequency range and originates from the in-phase, radial vibration of all carbon atoms. The Raman shift is approximately inversely dependent on the SWCNT diameter and can thus be used to determine the chiral purity of a sample.[229] For (6,5) SWCNTs, the RBM appears at ~ 309 cm^{-1}. A defect-activated mode (D-mode) is present at ~ 1310 cm^{-1}, resulting from a double-resonant Raman scattering event that involves scattering at a defect site. The high-frequency range of the spectrum is caused by tangential modes where carbon atoms move tangentially to the nanotube wall, giving rise to multiple G modes (G^-, E_2, G^+) between 1500 and 1625 cm^{-1}. The ratio of D and G^+ mode intensity is associated with the number of lattice defects,[230] and a linear dependence of the sp^3 defect density on the D/G^+ ratio increment upon defect introduction has been reported.[207]

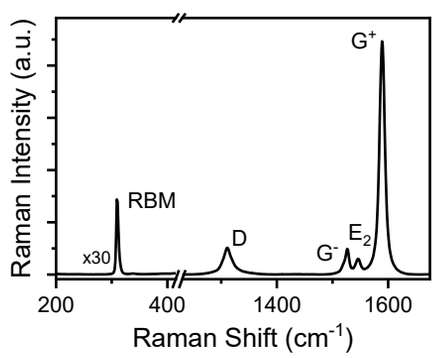

Figure 3.3: Representative Raman spectrum of a sparse (6,5) SWCNT network (532 nm excitation). The intensity in the RBM range was scaled by a factor of 30 for visibility.

The chiral purity of the (6,5) SWCNT stock dispersions (see Section 3.1.2) was assessed from thick networks, drop-cast on aluminum foil. Spectra in the RBM range where mapped and averaged across an SWNCT network area of 100×100 μm^2 with more than 1000 spectra using a 50× long-working distance objective (Olympus, N.A. 0.50). Raman spectra of SWCNTs for oxygen defect functionalization (see Chapter 5) were collected in the D and G^+ mode range with a 50× short working distance objective (Olympus, NA 0.75) to improve the signal

intensity from the sparse spincoated networks. Spectra were acquired in three different positions from 1500 spots across 40×70 μm^2, respectively. Renishaw Wire 3.4 software was used to fit each spectrum with mixed Lorentzian and Gaussian fit functions. Average D/G^+ ratios were obtained from the D/G^+ ratios calculated in each spot. When the single-spot spectral quality was insufficient for reliable fitting (at D band maximum intensities < 100 counts), the average D/G^+ ratio was generated through fitting of the averaged Raman spectrum.

3.2.5 Electrical characterization

The electrical properties of the (6,5) SWCNT network-based FETs were characterized in a dry nitrogen atmosphere. Current-voltage characteristics were recorded with an Agilent 4155C semiconductor parameter analyzer. The capacitances were determined in the transistor on-state[153] using an LCR meter (E4980A, Agilent Technologies Inc.) with a 0.5 V AC modulation amplitude of the gate voltage at a frequency of 1 kHz. The source and drain electrodes were shorted and grounded, forming a metal-insulator-semiconductor plate capacitor. A representative capacitance-voltage sweep is shown in **Figure 3.4**. The non-zero capacitance in the off-state arises from the metal-insulator-metal capacitance of the metallic bottom electrodes. The areal capacitance C_i was calculated from the measured capacitance value using the total capacitor area, that is, the overlap between the gate electrode and the semiconductor layer.

Trap densities and linear field-effect mobilities were calculated following Equations (12) and (13). The linear field-effect mobilities of the charge carriers in SWCNTs are gate voltage-

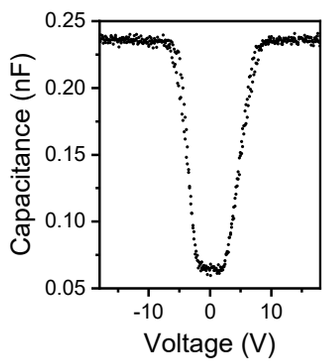

Figure 3.4: Capacitance-voltage characteristics of a (6,5) SWCNT network-based field-effect transistor (forward and reverse sweep), acquired at an AC modulation frequency of 1 kHz.

dependent as a consequence of their one-dimensional density of states,[162] and the values presented in this work correspond to the mobilities at the maximum.

3.2.6 Photoluminescence spectroscopy

Photoluminescence spectra were collected in an in-house setup with two different sample stages for room-temperature and temperature-dependent experiments as visualized in **Figure 3.5**. The SWCNTs were excited at 640 nm with a continuous-wave laser diode (OBIS, Coherent) that was cut off at 750 nm using a short-pass filter (**SP**). Multiple gold mirrors (**M**) guided the excitation and emission beam through the objective and through a dichroic long-pass filter (**DLP**, cut-on 875 nm) towards the desired sample stage and through a tube lens (**TL**) towards the detector, respectively. The dichroic long-pass filter and an additional 850 nm long-pass filter (**LP**) blocked reflected excitation laser light from the detection setup that consisted of a Princeton Instruments IsoPlane SCT 320 spectrograph (**SG**, blaze wavelength 1300 nm, 85 lines mm^{-1}) and a thermo-electrically cooled two-dimensional (2D) InGaAs camera (NIRvana 640ST, Princeton Instruments, 512×640 pixels, detection range 950 – 1600 nm). Note that the excitation laser beam was expanded with a plano-convex lens

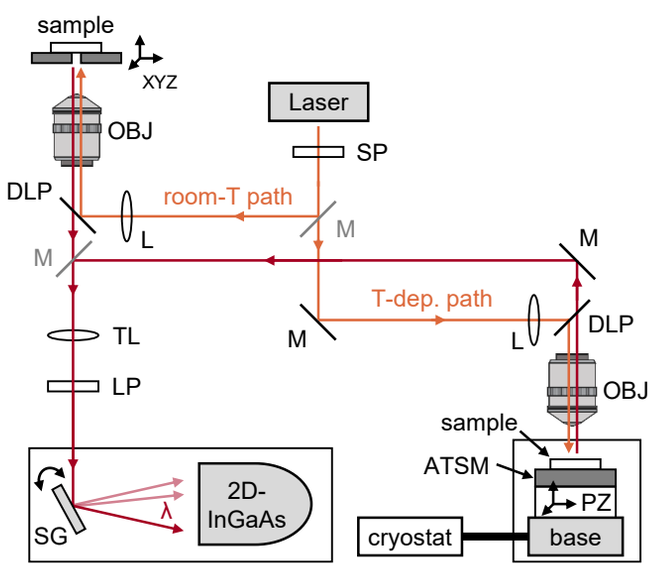

Figure 3.5: Schematic photoluminescence setup with a sample stage for room-temperature measurements and a cryo-stage for temperature-dependent experiments. The corresponding beam path can be selected through flip-mirrors (grey). The setup was simplified for clarity by omitting several mirrors. SP – short-pass filter, M – mirror, L – lense, DLP – dichroic long-pass filter, OBJ – objective, TL – tube lense, LP – long-pass filter, SG – spectrograph, ATSM – agile temperature sample mount.

(**L**, focal length f = 125 mm) in front of the near-infrared optimized objective (**OBJ**, room-temperature measurements: 20× Olympus objective, temperature-dependent measurements: 50× Mitutoyo objective) to average the PL spectra across an area of 600 to 800 μm^2 and thus minimize spot-to-spot variations resulting from SWCNT network inhomogeneities (see **Figure 3.6**). Additionally, the measurement times were reduced and temporal variations due to potentially instable FET operation (see below) were avoided compared to single acquisitions in multiple spots. Averaged PL spectra were acquired from three different positions per sample to ensure reproducibility. Furthermore, PL spectra acquired in a single spectral acquisition along the 2D detector array could be analyzed in each spot with respect to the SWCNT density that was inferred from the respective pristine, uncharged PL intensity.

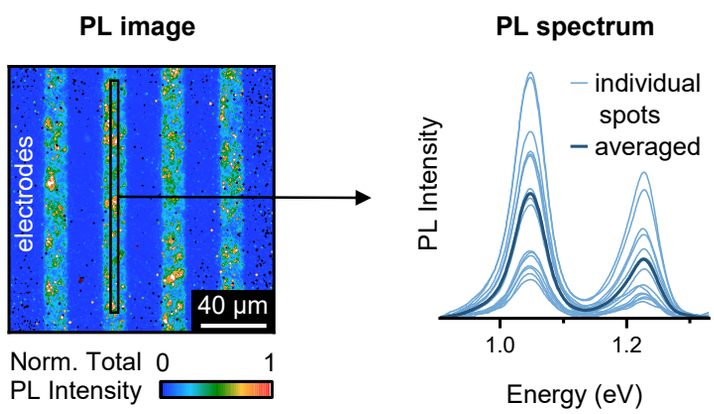

Figure 3.6: Normalized total PL intensity image (spectrograph in mirror mode) from an extended area of the SWCNT network through expansion of the exciting laser beam. Selecting a certain range as indicated by the black box, PL spectra can be collected and averaged across a larger part of the 2D detector to enhance reproducibility and measurement time efficiency.

Room-temperature experiments were carried out on a manually controllable XYZ stage with the excitation and emission passing through the substrate. For gated PL measurements as employed in Chapter 4, FETs were electrically connected to a Keysight B1500A semiconductor parameter analyzer. Spectra were acquired under various constant gate voltages while a small drain voltage V_d = 0.01 V was applied to monitor the current flow and ensure the integrity of the gate dielectric without significantly influencing the charge carrier distribution across the channel length.

Temperature-dependent PL measurements were performed using a closed-cycle liquid helium-cooled cryostat (Montana Cryostation s50, 4.6 K base temperature) at high vacuum

(< 10^{-5} mbar). The setup included an agile temperature sample mount (ATSM) with a Lakeshore Model 335 temperature controller on a three-dimensional piezo stage (**PZ**).

Strong PL quenching upon gating (see Chapter 4) and very low SWCNT densities (see Chapter 5) resulted in a generally weak PL signal. The thus required high exposure times of up to 30 s enabled low-noise PL spectra, but also caused a significant impact of the constant thermal detector background on the acquired spectra. Moreover, the background increased throughout a gated-PL measurement series (see Chapter 4) due to heating of the detector during the hours-long experiment. Hence, additional data processing as detailed in **Figure 3.7** was essential. A detector background spectrum was recorded after each PL acquisition, and the background was manually subtracted from the recorded spectrum. Furthermore, reflection and scattering of the excitation laser beam at the sample interfaces was significant compared to the weak SWCNT PL, leading to an additional background that increased non-linearly towards lower wavelengths. Accordingly, laser reflection spectra were collected from each bare substrate type (without deposited SWCNTs) and subtracted from the respective detector background-corrected SWCNT PL spectra with a factor that would account for spot-dependent laser reflection intensities. The thermal background- and laser reflection-corrected spectra were finally corrected for detector sensitivity and absorption of the optics in the detection path, and converted from wavelength to energy scale using Jacobian conversion as detailed elsewhere.[231] For further analysis, the PL spectra were fitted with three and two Lorentzian peaks in Chapter 4 and 5, respectively.

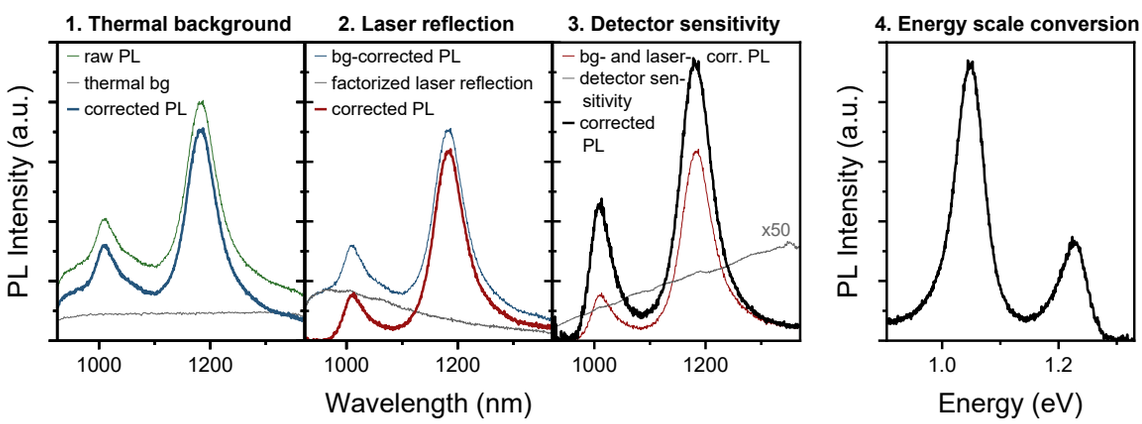

Figure 3.7: Processing of raw PL spectra. Correction for (1) the thermal background (bg) and (2) the reflection and scattering of the excitation laser beam. (3) Correction of the thermal background- and laser reflection-corrected spectrum for detector sensitivity and absorption of the optics in the detection path (correction function scaled by factor 50 for better visibility), and (4) conversion from wavelength to energy scale.

3.2.7 Time-correlated single-photon counting

The PL decay of oxygen defects in SWCNT networks was recorded *via* time-correlated single-photon counting (TCSPC) in a measurement setup similar to the room-temperature PL spectroscopy setup (see **Figure 3.6**). A 640 nm picosecond-pulsed supercontinuum laser (NKT Photonics SuperK Extreme) served as the excitation source and as the electrical trigger of a photon counting module (PicoQuant PicoHarp 300) and a gated InGaAs/InP single-photon avalanche photodiode (Micro Photon Devices) to detect the arrival of photons with temporal resolution. The wavelength of the detected photons was selected with a spectrograph (Princeton Instruments Acton SpectraPro SP2358) and corresponded to the maximum of the oxygen defect peak under investigation. The resulting time traces were fitted biexponentially with a short and a long lifetime component using the reconvolution mode in the SymPhoTime64 software. The fast, instrument-limited E_{11} decay of a drop-cast (6,5) SWCNT network at 1000 nm served as the instrument response function (IRF) with a full width at half maximum of 84 ps.

4. Influence of the environment on charge transport and trions in SWCNTs

This chapter investigates the impact of the dielectric environment of (6,5) SWCNT networks in field-effect transistors, represented by the gate dielectric material, on transistor performance and photoluminescence properties. Special attention is directed towards understanding the impact of charge traps, introduced by the nanotube environment, on trion (charged exciton) emission. Parts of this chapter, including versions of figures and tables, were published by the American Chemical Society in the article Wieland *et al.*, *J. Phys. Chem. C* **2023**, *127*, 3112 – 3122.[232]

4.1 Introduction

The luminescence spectra of pristine single-walled carbon nanotubes are commonly governed by the radiative decay of optically bright excitons, resulting in a characteristic E_{11} emission peak in the near-infrared. As detailed in Section 2.2, advances in SWCNT sorting and purification have facilitated the observation of trion emission from nanotubes in the presence of chemically,[17,22] electrochemically[23–26] or electrostatically [16,27,28] induced charges. A trion is a three-particle bound state of an excitonic electron-hole pair with an additional positive or negative charge carrier. Compared to the exciton, the trion emission energy is lowered by the diameter-dependent singlet-triplet exchange splitting and trion binding energy (100 – 200 meV).[17,23] Apart from trion formation, excess charge carriers also cause nonradiative exciton decay in an Auger-type quenching process.[14,233] Since the extent of trion emission and exciton quenching depends on the number of charges induced in the nanotubes, comparing the trion emission intensity relative to the exciton emission intensity (trion/exciton ratio) may enable the optical assessment of charge carrier densities.[32]

The limited dielectric screening in the quasi one-dimensional SWCNTs makes their optical and electronic properties highly susceptible to external influences. The strong interaction of the

excited states with the dielectric environment already manifests in the observation of substantial E_{11} broadening. This has previously been attributed to an increase in inhomogeneity of the environment for deposited compared to dispersed SWCNTs, and for individual carbon nanotubes compared to nanotube networks.[126–128] Furthermore, various theoretical and experimental studies reported a reduction in PLQY and decreasing exciton transition energies with increasing dielectric constant of the environment of dispersed[123,129,131] and individual[35,121] SWCNTs due to screening effects.

Whereas numerous studies investigated the impact of the nanotube environment on excitons, its specific interaction with trions (see **Figure 4.1**) is barely understood. Trion emission has been studied in different external environments, such as in aqueous dispersions or in ionic liquids,[141,183–185] and also in differing intrinsic dielectric environments through variation of the nanotube chirality.[23] Theory predicts reduced trion binding energies with increasing dielectric constant of the external environment,[21] and experimental studies have been conducted in various different environments (*e.g.* in air, vacuum, ionic liquid, and aqueous dispersion).[17,24,35,36] Yet, systematic experimental investigations remain scarce, even though a better understanding of the factors influencing trions in SWCNTs is crucial especially for optoelectronic devices, where the presence of excess charge carriers may lead to trion electroluminescence.[16,31,188] This additional red-shifted emission can be detrimental to optoelectronic applications which require high exciton purity and external quantum efficiency and should therefore ideally be suppressed.

While adjustment of the nanotube environment might offer opportunities to control trion emission from electronic devices based on SWCNTs, it is essential to also consider the impact of the dielectric environment on charge transport within networks of carbon nanotubes. Theoretical calculations suggested that strong surface polar phonon scattering on highly polar substrates, such as hafnia, can impede intratube charge transport,[175] similar to the effect of

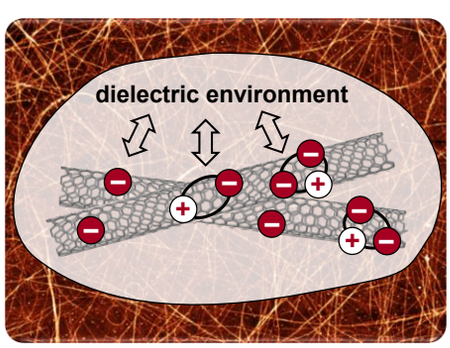

Figure 4.1: Schematic of charge carriers, excitons and trions (from left to right) interacting with the dielectric environment of carbon nanotube networks, shown here for negative excess charge carriers.

charge localization induced by Fröhlich polarons in single crystals.[234] Experimental investigations have corroborated these findings, further suggesting that reduction of intertube charge transport caused by randomly oriented dipoles in highly polar substrates constitutes another significant element influencing charge carrier mobilities in networks of carbon nanotubes.[166] These studies also documented differences in drain currents and field-effect mobilities of holes compared to electrons. Although a correlation with the dielectric environment seems likely, its precise role remains uncertain.[166] Additional factors such as trap states inherent in the dielectric material or generated during the deposition process, add to the intricacies involved in the analysis of such devices.[177]

Top-gate/bottom-contact field-effect transistors (FETs) with carbon nanotube networks as the semiconducting layer, discussed in detail in Section 2.4, enable simple modification of the nanotube environment through variation of the gate dielectric material that is in direct contact with the nanotubes and the active channel,[166,235,236] where trion formation is expected to take place. Precise study of the charge carrier density-dependent optoelectronic properties is possible through adjustment of the applied gate voltage, and both holes and electrons can be injected into small-diameter nanotubes like (6,5) SWCNTs with high efficiencies and without changing the material of the injecting electrode. Importantly, while chemical or electrochemical hole and electron doping includes relocating or introducing counterions or chemical dopants that affect the immediate nanotube environment, electrostatic doping in an FET geometry allows for the injection of both polarities of charge carriers into devices with the same gate dielectric material, *i.e.*, the same dielectric environment.

This chapter explores the effects of the dielectric environment on the optical and electronic properties of random (6,5) SWCNT networks in top-gate FETs. Both exciton and positive and negative trion photoluminescence is analyzed under electrostatic gating for five different polymeric and inorganic gate dielectric materials, selected to cover a broad range of dielectric constants ε (from 1.9 to over 20) and varying charge trapping properties. The specific influence of charge traps is further assessed by a systematic reduction of electron traps with 1,2,4,5-tetrakis(tetramethylguanidino)benzene (ttmgb).

4.2 Device fabrication and gate dielectric variation

The influence of environmental factors on the electrical and optical properties of (6,5) carbon nanotubes was investigated through integration of various gate dielectrics into top-

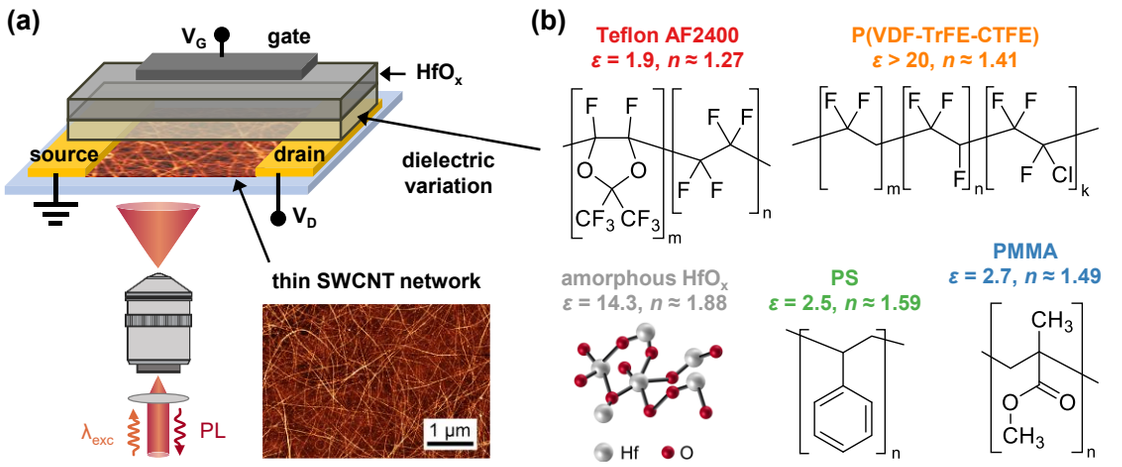

Figure 4.2: a) Schematic top-gate/bottom-contact field-effect transistor layout with atomic force micrograph of a thin, random (6,5) SWCNT network used as the semiconductor. The nanotubes are optically excited with an expanded laser beam. b) Molecular structures, static dielectric constants ε and refractive indices n of the different dielectric materials investigated as gate dielectrics in contact with the nanotubes.

gate/bottom-contact field-effect transistors with carbon nanotubes as the semiconductor (see **Figure 4.2**). The different gate dielectrics functioned as the immediate surroundings of the nanotube networks.

Random (6,5) SWCNT networks were deposited onto photolithographically patterned gold source and drain electrodes. The deposition process involved triple spincoating of chirality-pure nanotube dispersions as detailed in Section 3.1.2. To confine the SWCNTs to the channel area, they were protected photolithographically while nanotubes outside the channel area were removed through reactive oxygen plasma etching (see Section 3.1.3), thus minimizing gate leakage. A low network density of 30 nanotubes per µm with an average SWCNT length of 1.2 ±0.4 µm was chosen to ensure contact of all SWCNTs with the gate dielectric for effective interaction while maintaining percolation for uniform charge transport.[153,158] The presence of some network inhomogeneities, *e.g.*, small degree of nanotube bundling, is also expected to affect the immediate dielectric environment of the SWCNTs and the nanotube gating efficiency. However, such smaller local variations should not affect the global device performance, and any influence on photoluminescence (PL) was mitigated by averaging the PL spectra across a larger area through beam expansion (see **Figure 4.2a**) as discussed in more detail in Section 4.4. Furthermore, the wrapping polymer, covering ~ 10 % of the nanotube surface,[237] and glass substrate present additional components of the SWCNT dielectric

environment. Since all devices within the gate dielectric variation series were fabricated from one batch of polymer-sorted SWCNTs and at the same time under identical conditions, these factors can be expected to be uniform across the samples.

The selection of dielectric materials was based on their broad range of dielectric constants and molecular structures, which included fluorinated, polar, or aromatic side groups, as well as their successful prior application in nanotube-[166,238] or organic semiconductor-based[239,240] FETs. The polymeric dielectrics were further chosen for their solution-processability while keeping the underlying SWCNT layer intact due to orthogonal solubilities. The polymeric dielectrics Teflon AF2400, poly(vinylidene fluoride-*co*-trifluoroethylene-*co*-chlorotrifluoroethylene) (P(VDF-TrFE-CTFE)), poly(methyl methacrylate) (PMMA), and polystyrene (PS) were deposited *via* spincoating and post-processing as detailed in Section 3.1.3. The polymers formed uniform, pinhole-free films with sub-nanometer root mean square roughness (rms), except for the copolymer P(VDF-TrFE-CTFE), which exhibited an rms of 2.3 nm (see **Figure 4.3**) due to phase segregation.[166] The polymer layer thickness was set relatively high (50 nm) to prevent any potential influence from the overlying HfO_x dielectric in the hybrid dielectric device layout. HfO_x was deposited *via* atomic layer deposition for its encapsulating effect, enabling *n*-type

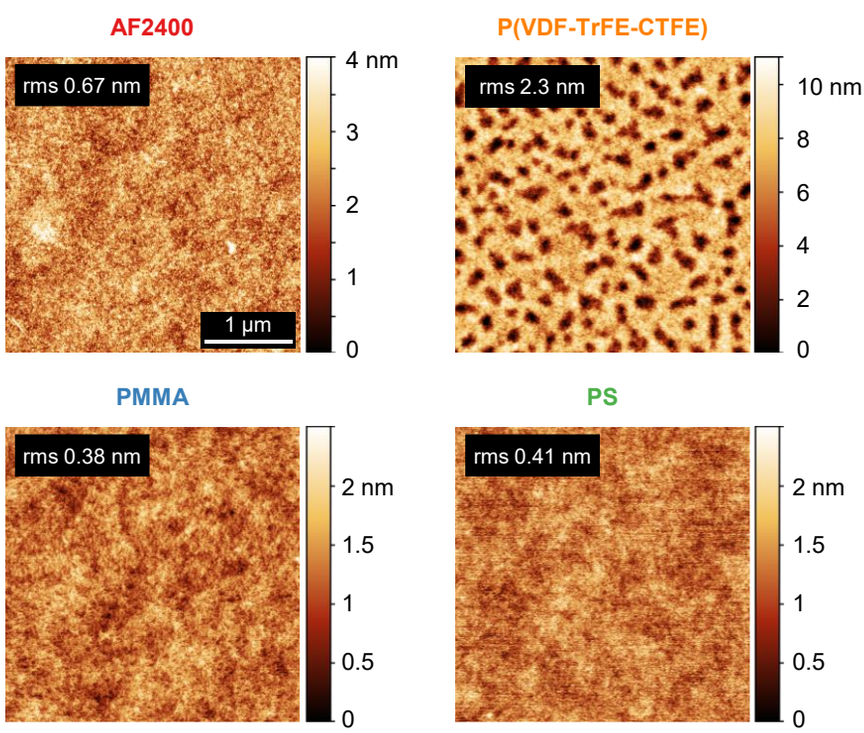

Figure 4.3: Atomic force micrographs of the polymer dielectric layers with the corresponding root mean square roughness (rms).

FET operation under the ambient conditions of the laser setup (see Section 3.2.6), with the additional benefit of enhanced operational stability due to the high electric breakdown strength of the oxide.[177] In addition to the hybrid dielectric approach, devices solely utilizing HfO_x as the gate dielectric were built to specifically study the effects of this frequently used SWCNT-FET dielectric material.[238,241] This approach further aimed at assessing any potential undesired impact of the oxide on the properties of nanotubes in hybrid dielectric devices. The dielectric material in direct contact with the SWCNTs, which is expected to influence the nanotube PL, is referred to as primary dielectric hereafter.

4.3 Transistor performance

Representative transfer characteristics of nanotube network-FETs with the five selected gate dielectrics at low drain voltage are shown in **Figure 4.4**. For devices based on dielectrics with lower dielectric constants, wider gate voltage ranges were applied because of their lower areal capacitances C_i. Hence, transistor turn-on and maximum charge carrier mobilities were achieved at higher gate voltages compared to FETs employing gate dielectrics with higher dielectric constants. The experimentally determined areal capacitances corresponded well to the areal capacitances calculated from the dielectric constants under the assumption of a parallel-plate capacitor (see **Table 4.1**). Ambipolar transport was observed in all devices, displaying high on/off ratios of up to 10^5 and low gate leakage currents. Consequently, gate leakage should not significantly affect the measurements. Variations in on-currents were

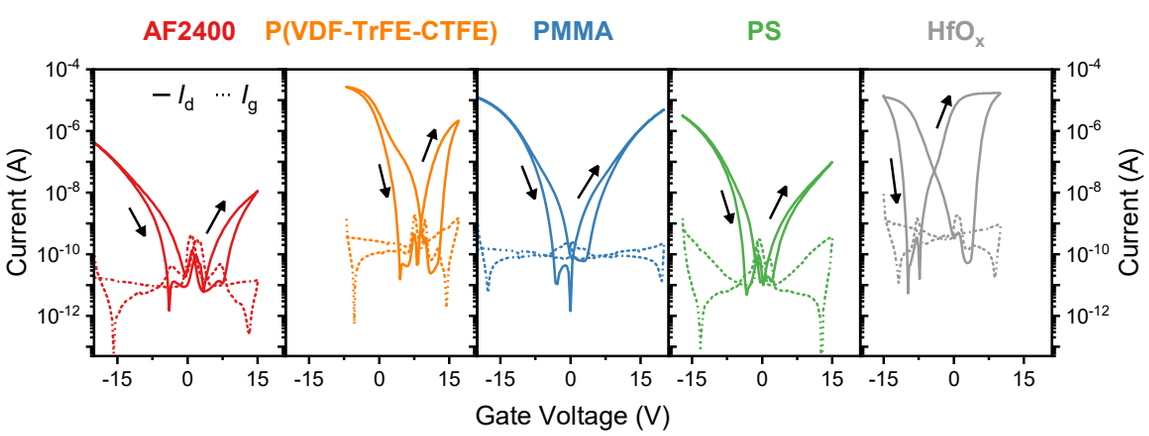

Figure 4.4: Ambipolar transfer characteristics of FETs with different gate dielectrics in contact with random (6,5) SWCNT networks (channel length L = 20 µm, channel width W = 10 mm) acquired at V_d = 0.01 V.

Table 4.1: Static dielectric constants ε of the different gate dielectrics with areal capacitances C_i and charge carrier mobilities μ_{lin} of the corresponding FETs. Capacitances were extracted in FET on-state experiments and calculated from the respective dielectric constants assuming a parallel plate capacitor with two dielectric layers in case of the devices with a hybrid dielectric. The asterisk (*) indicates that the maximum mobility was not reached because of early device breakdown.

	AF2400	P(VDF-TrFE-CTFE)	PMMA	PS	HfO_x
ε	1.9	> 20	2.7	2.5	14.3
$C_{i,\,meas.}$ (nF cm^{-2})	26	123	39	32	198
$C_{i,\,calc.}$ (nF cm^{-2})	27	125	38	35	181
$\mu_{lin,h}$ (cm^2 V^{-1} s^{-1})	8.0 ± 0.8	13.7 ± 1.2	15.0 ± 1.2	7.1 ± 0.6	3.8 ± 0.3
$\mu_{lin,e}$ (cm^2 V^{-1} s^{-1})	2.0 ± 0.1 (*)	1.6 ± 0.3	13.5 ± 0.8	2.7 ± 0.2	5.2 ± 0.4

observed when comparing hole and electron transport for the same dielectric, as well as when comparing FETs with different dielectrics but of the same charge carrier type (holes or electrons). Likewise, variations in linear field-effect mobilities occurred (see **Table 4.1**). Note that the mobilities reported here do not take contact resistance into account, leading to an underestimation by approximately 20 – 30%. The transistor output characteristics revealed varying degrees of non-Ohmic charge carrier injection (see **Figure 4.5**), indicative of an influence of the dielectric materials on charge injection.[239] Linear mobility values derived from gated four-point probe measurements, which include correction for such non-ideal behavior, would offer additional insights.[162] However, such investigations were beyond the scope of this study.

FETs with the fluorinated polymers Teflon AF2400 and P(VDF-TrFE-CTFE) and with PS as the primary hybrid dielectric components exhibited significantly higher hole compared to electron mobilities. P(VDF-TrFE-CTFE) further caused a strong onset-voltage shift towards positive gate voltages, along with notable drain current hysteresis that diminished when sweeping the gate voltage in a range that induced hole accumulation only, but remained nearly unchanged upon exclusive electron sweep (see **Figure 4.6**). This observation suggests the presence of electron traps, a characteristic well-documented for fluorinated polymers.[242,243] In contrast to that, devices with PS as the primary dielectric displayed no substantial onset-voltage shifts, and the already small hysteresis observed in the full-range gate voltage sweep became negligible when sweeping a smaller gate voltage range, inducing solely on hole or electron current. Consequently, no indications of significant charge carrier trapping, just as in devices with PMMA, were noted for FETs with PS as the primary gate dielectric.

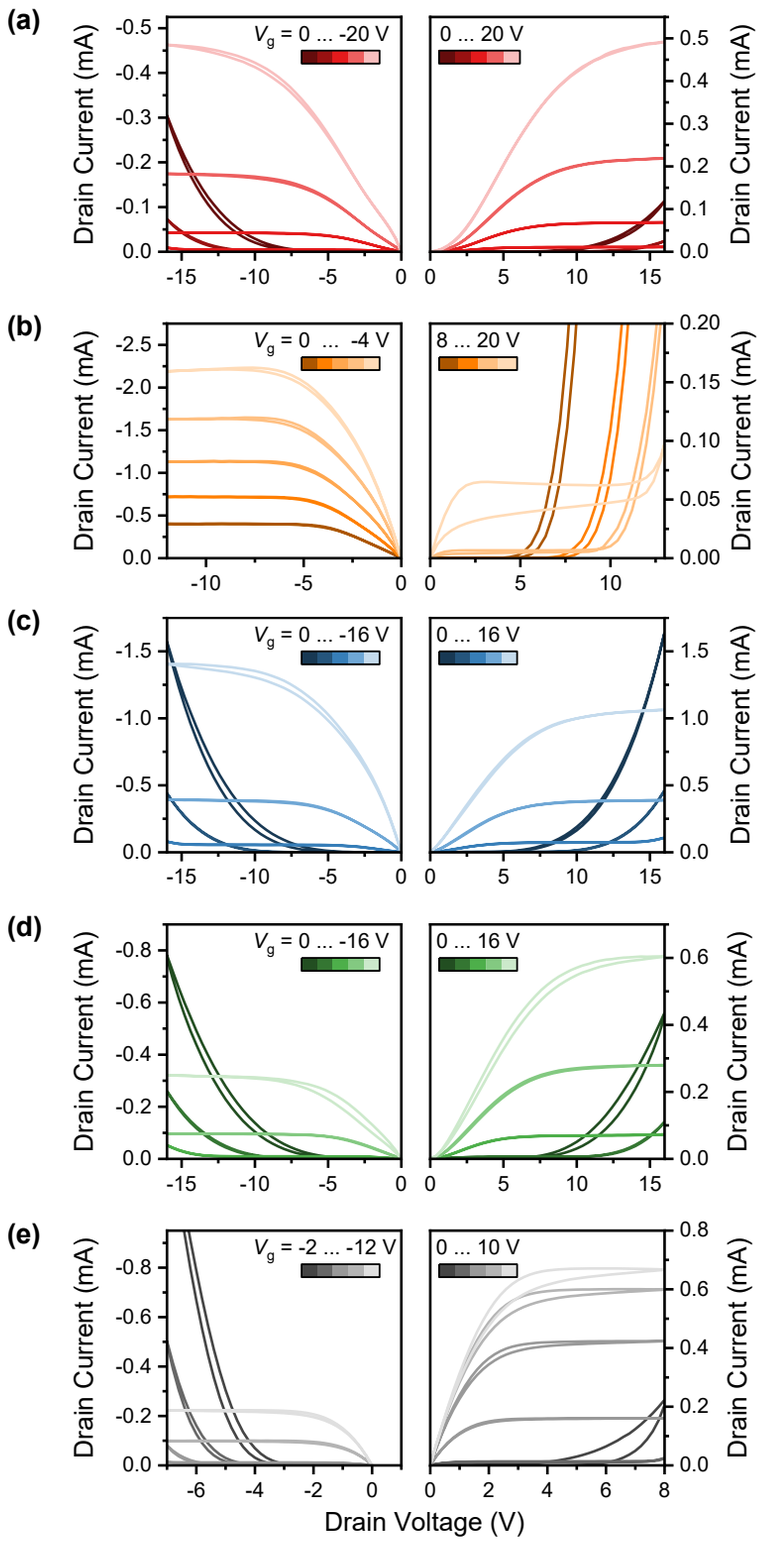

Figure 4.5: Output characteristics of FETs with a) Teflon AF2400, b) P(VDF-TrFE-CTFE), c) PMMA, d) PS and e) HfO_x gate dielectrics in direct contact with random (6,5) SWCNT networks for hole (left) and electron injection (right) from the source electrode.

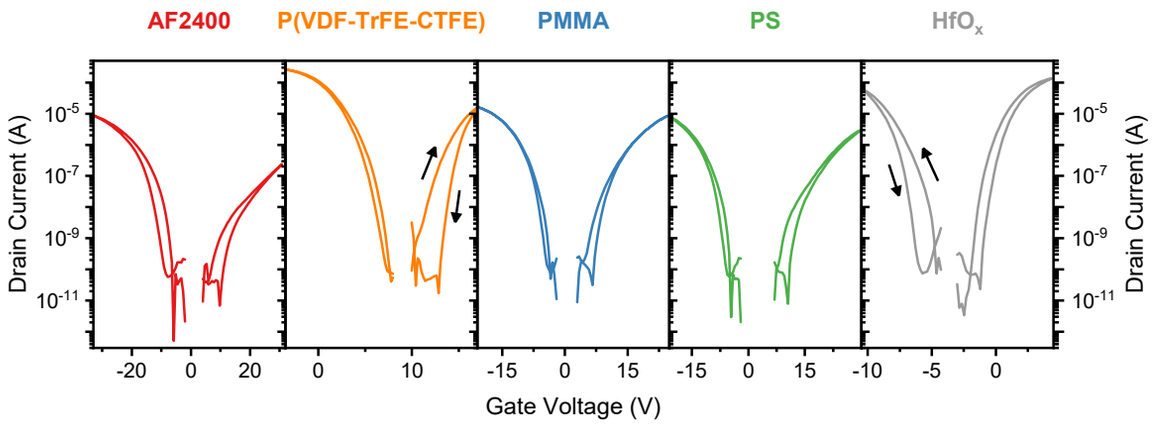

Figure 4.6: Varying degrees of current hysteresis in the transfer characteristics of FETs (L = 10 µm, W = 10 mm, V_d = -0.01 V) depending on the primary gate dielectric. A dependence on the polarity of the induced charge carriers was also observed as the gate voltage range was adjusted to selectively induce either holes or electrons within one V_g sweep.

Devices employing PMMA and HfO_x as primary dielectrics exhibited balanced ambipolar transport. Yet, their distinct gate-voltage-dependent behavior and mobilities differed. PMMA caused minimal current hysteresis, onset voltages close to zero, and very symmetrical hole and electron transport, yielding the highest mobilities among the tested primary dielectrics (up to 15 $cm^2 V^{-1} s^{-1}$). This nearly ideal performance of hybrid dielectrics with PMMA as the layer contacting the SWCNTs is widely recognized and has been utilized in numerous previous studies.[153,162,177] In contrast to that, FETs with HfO_x gate dielectric exhibited pronounced hysteresis that persisted during the hole-only sweep but was substantially reduced when exclusively introducing electrons. Additionally, the onset-voltage shifted towards negative gate voltages. These observations suggest hole-trapping in agreement with previous findings, as HfO_x has been employed in exclusively *n*-channel SWCNT transistors for its hole-trapping properties in earlier studies.[244] Moreover, the pronounced differences in charge transport of FETs with HfO_x compared to the hybrid dielectric devices suggest that the 50 nm polymer thickness effectively suppresses the impact of HfO_x onto the SWCNTs.

Generally, a substantial impact of the primary gate dielectric material on device performance was observed, although no discernible trend was identified concerning the dielectric constant of the gate dielectric. Consequently, dipolar disorder alone cannot account for these variations, suggesting that the above-discussed specific charge trapping properties of the dielectric materials present a more significant factor influencing the overall device behavior.

4.4 Establishing consistency in photoluminescence studies of gated SWCNT networks

While the distinct charge transport properties varied among FETs with the different dielectrics, all devices exhibited ambipolar charge transport. This characteristic makes them well-suited for gated photoluminescence experiments aimed at studying positive and negative trions in (6,5) SWCNTs in different dielectric environments. However, PL spectroscopy in devices and at nanotube networks requires special experimental and analytical methods to ensure comparability and reproducibility, which will be introduced in this section.

Gated PL experiments were carried out in an ambient PL setup with an expanded laser beam to excite and collect emission from a larger area as described in Section 3.2.6. The positive or negative gate voltage was increased stepwise and PL spectra were acquired at each voltage step from the same position within the transistor channel. Due to the different electric breakdown strengths of the gate dielectrics, the maximum reachable gate voltages varied. Throughout the measurement series, a small drain voltage $V_d = 0.01$ V was applied to monitor the drain and gate current. The integrity of the FETs was thus ensured while maintaining quasi-capacitor operation with minimum disturbance to the charge carrier distribution along the channel length. Due to the different capacitances of the devices under investigation, the applied gate voltages were converted for comparability into densities $Q = C_i \cdot (V_g - V_g(Q = 0))$ of the combined mobile and static charge carriers using the measured areal capacitances C_i. Prior to conversion, the gate voltage values were reduced by the distinct off-state voltages $V_g(Q = 0)$ of the transistors. A similar approach was employed by Lee *et al.*[166] The off-state, defined as $Q = 0$ in this work, was determined spectroscopically as the voltage associated with the highest SWCNT photoluminescence (PL) intensity, which corresponded well with the gate voltage at the drain current minimum in the simultaneously collected transfer curves.

The choice of PL intensity as a metric for the zero charge carrier density state was motivated by the charging-induced reduction of the oscillator strength of the optical transitions and of the emission efficiency of the E_{11} transition as a result of Auger-type exciton quenching (see **Figure 4.7a** for FETs with PMMA as the primary gate dielectric).[14,26,135,183] The least-charged state was reached at positive gate voltages in case of FETs with the fluorinated polymers Teflon AF2400 and P(VDF-TrFE-CTFE) as primary gate dielectrics, and at negative voltages for PS and HfO_x devices, in agreement with the respective charge transport properties discussed in Section 4.3. Accordingly, the $Q = 0$ state equaled the $V_g = 0$ state for FETs with PMMA as the primary component of the hybrid dielectric.

It should further be noted that the uncharged SWCNT networks exhibited a broad PL feature between 1.180 and 1.226 eV that was composed of two distinct peaks, as exemplarily shown in **Figure 4.7b** for an FET with PMMA as the primary gate dielectric. Such broadened emission of nanotubes in devices compared to nanotubes in dispersion and single-layer deposited nanotubes results from the device processing which includes multiple heating steps.[55] Heating the networks at 300 °C under inert conditions removes substantial amounts of the electron-trapping water and oxygen adsorbed on the surface for enhanced device performance, but also causes structural defects in the SWCNT lattice that can deteriorate the PL quality.[55] Accordingly, while the peak between 1.220 and 1.226 eV originates from free excitonic E_{11} transitions, the red-shifted feature between 1.180 and 1.189 eV likely corresponds to defect-related emission like the Y sideband,[112] which was found to increase upon annealing.[55] The faster quenching of the Y band PL intensity compared to the E_{11} upon nanotube charging (see E_{11}-normalized gating-dependent PL spectra, **Figure 4.9**), similar to the previously observed behavior of luminescent sp^3 defects,[164] corroborated this notion. Since such defect-related emission is still of excitonic character, the combined fitted E_{11} and Y band intensity was used for the analysis of PL intensities in this study, neglecting possible differences in oscillator strengths of the two transitions. Note that separate treatment of the E_{11} and Y bands did not affect the observed trends.

Importantly, the gated-PL behavior was affected by the SWCNT network density as exemplarily shown in **Figure 4.8a** for devices with PMMA as component of the hybrid dielectric. Specifically, the above-mentioned gating-induced exciton quenching and the

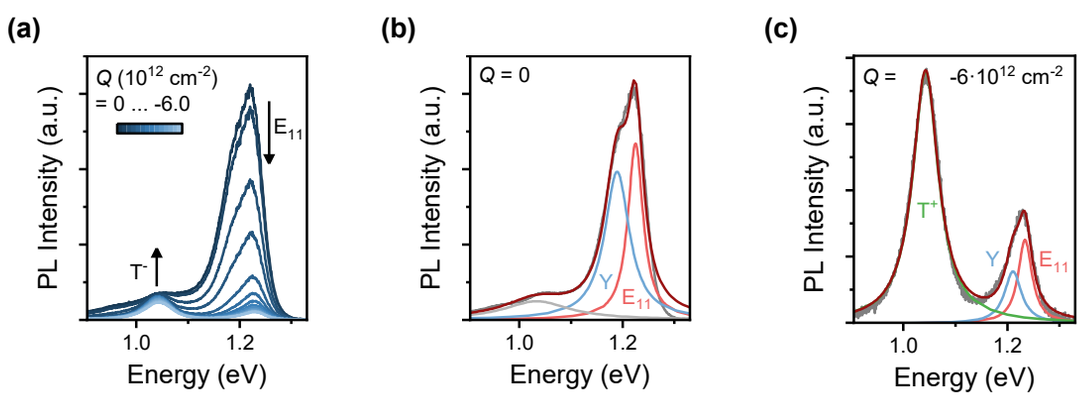

Figure 4.7: a) Evolution of gated PL spectra from (6,5) SWCNT network FETs with PMMA as the dielectric in direct contact with the nanotubes. b) Lorentzian multi-peak fit of the PL spectrum in the uncharged state (Q = 0). Note that a third, low-energy band (grey line) was added to the fit of the E_{11} (red line) and Y band (blue line) peaks. Red-shifted features in this energy range have previously been assigned phonon-coupled transitions of the bright and the K-momentum dark excitons.[104,112] c) Lorentzian fit of a gated PL spectrum, including trion (green line), Y band and E_{11} emission.

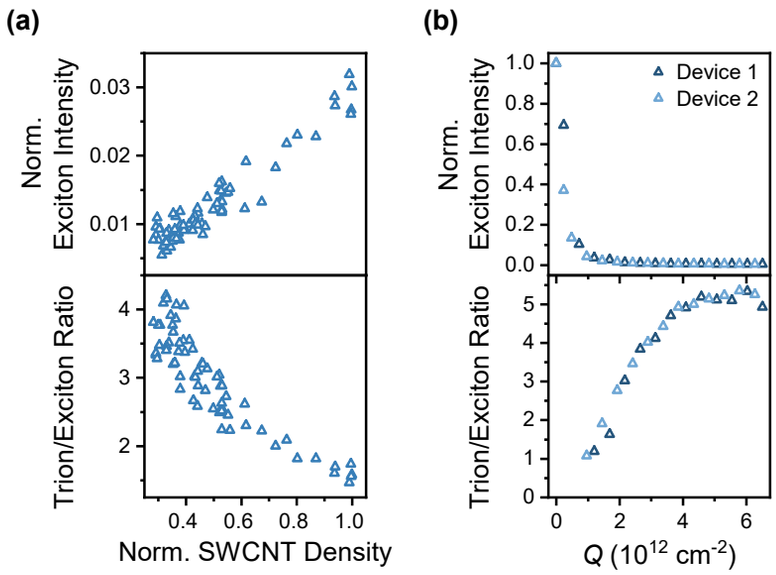

Figure 4.8: a) SWCNT density dependence of exciton quenching (exciton intensity relative to the intensity in the zero-charged state, top) and fitted trion/exciton ratios (bottom) at a constant $Q = 2.2 \times 10^{12}$ cm^{-2}. The normalized network density was obtained from the PL intensity in the uncharged state. b) PL spectra averaging creates reproducible charge carrier density-dependent exciton quenching (top) and trion/exciton ratios (bottom) on different devices, eliminating spot-to-spot variations.

trion/exciton ratio, both important metrics that will be investigated in Section 4.5, were reduced at higher nanotube densities by distributing the charge carriers to more nanotubes and shielding the electric gate field from the lower SWCNT layers. This strong dependence of the gating efficiency on the SWCNT density necessitated expansion of the excitation laser beam, in addition to eliminating spot-to-spot variations in the local dielectric environment of the nanotubes. Indeed, reproducible charge carrier density-dependent exciton quenching and trion/exciton ratios were obtained across different devices when employing this averaging concept (see **Figure 4.8b**).

4.5 Influence of the dielectric environment and gating on nanotube photoluminescence

The method established in Section 4.4 enabled the reproducible and comparable acquisition of exciton and trion PL from gated (6,5) SWCNT networks in field-effect transistors, now being modified with the five different primary gate dielectrics, as summarized in **Figure 4.9**.

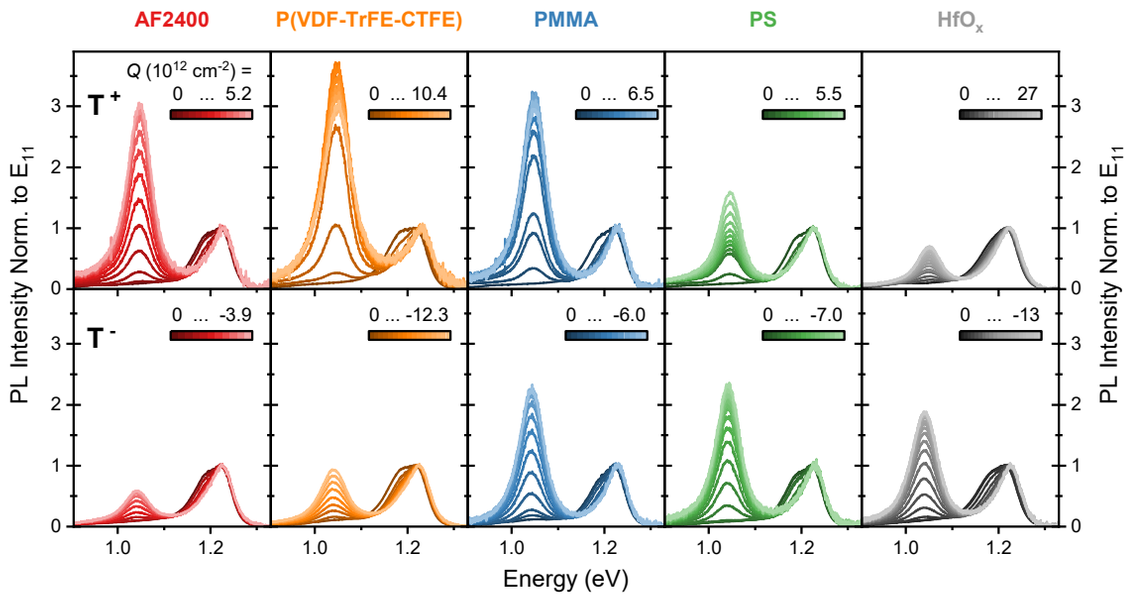

Figure 4.9: Dielectric material-dependent evolution of the nanotube PL spectra normalized to the E_{11} intensity upon hole (top row) and electron (bottom row) injection, showcasing different relative emission intensities of positive (T^+) and negative (T^-) trions.

In the uncharged state, the E_{11} transition energies and peak widths showed a strong dependence on the dielectric environment (see **Figure 4.10**). Overall, trends of decreasing emission energy ranging and increasing full width at half maximum (FWHM) towards higher dielectric constants were observed, which have previously been attributed to increased dielectric screening.[35,121,123,129,245]

Positive and negative gate voltages were applied to the FETs with different gate dielectrics to monitor the response of SWCNT emission to charge accumulation. Independent of the dielectric material, the emission intensity of the excitonic transition decreased nonlinearly upon nanotube charging as discussed in Section 4.4 and shown in **Figure 4.7a** for a gated FET with PMMA as the dielectric component in contact with the SWCNTs. While the PL spectra shown in **Figure 4.9** were normalized to the uncharged E_{11} emission intensity for better visualization of the relative intensity of the red-shifted trion emission feature that appeared upon gating (which will be discussed below), a plot of the gating-dependent relative exciton intensity (see **Figure 4.11a**) shows that such exciton quenching also occurred for FETs with the other primary dielectrics. The quenching efficiency varied strongly among the different dielectrics and additionally depended on the sign of the accumulated charge carriers. Therefore, the dielectric constant of the gate dielectric and the total number of charges cannot be the only

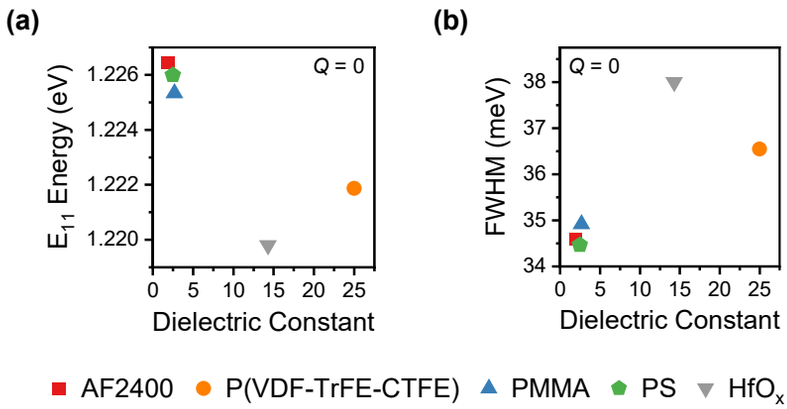

Figure 4.10: a) E_{11} emission energies and b) peak widths depending on the dielectric constant of the primary gate dielectric, obtained from Lorentzian peak fits in the uncharged state ($Q = 0$).

factors determining the extent of quenching. The refractive index, which has previously been used to describe trends in the optical properties of carbon nanotubes,[131] can also not explain these observations. The differences between quenching efficiency for hole and electron accumulation were most pronounced for FETs with P(VDF-TrFE-CTFE) and HfO_x as primary gate dielectrics. Hole-induced exciton quenching was significantly stronger than quenching upon electron injection in case of P(VDF-TrFE-CTFE) devices, and *vice versa* in case of their HfO_x counterparts. Electrical analysis (see Section 4.3) pointed towards the most pronounced electron and hole trapping for these gate dielectric materials, respectively, suggesting that exciton quenching is predominantly caused by free and not by trapped excitons, in agreement with previous observations of symmetrical exciton quenching in free-standing SWCNTs which were gated through vacuum.[27]

Moreover, the emission energy of the excitons shifted towards higher energies upon gating (see **Figure 4.11b**). As detailed in Section 2.1.5, this phenomenon has previously been attributed to combined effects of a strong decrease in exciton binding energy and a weaker self-energy reduction,[26,27,136,246] or to exciton confinement.[22,141] Interestingly, the magnitude of the maximum E_{11} shift was influenced not only by the dielectric material in contact with the SWCNTs but also by the type of accumulated charge carriers (see **Table 4.2**). Similar to the exciton PL quenching efficiency, the maximum blueshift for a particular dielectric was larger when the dielectric exhibited weak trapping of the corresponding charge carrier polarity. For instance, the blueshift was more pronounced under hole accumulation than electron

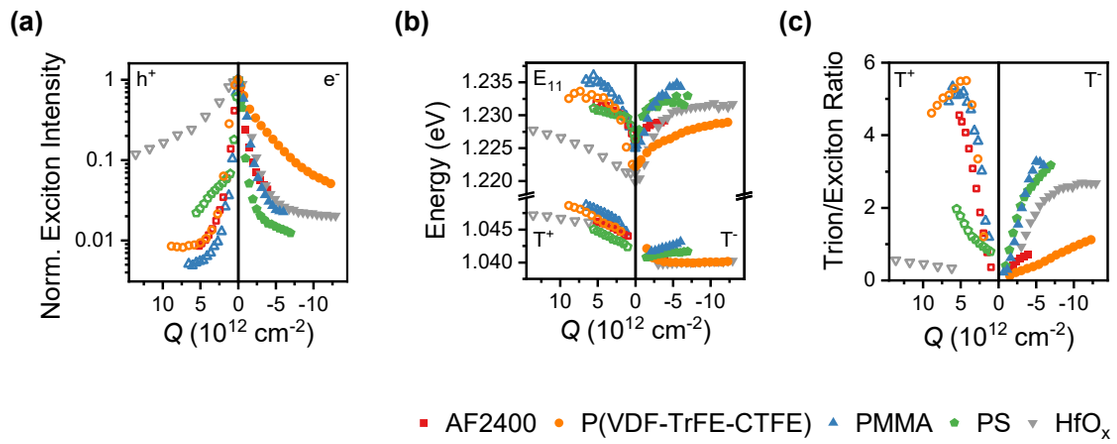

Figure 4.11: a) Exciton PL intensity, b) exciton and trion emission energy, and c) trion/exciton intensity ratio depending on the density and polarity of accumulated charge carriers and the dielectric material.

accumulation in FETs employing the strongly electron-trapping P(VDF-TrFE-CTFE) as primary gate dielectric.

While the exciton intensity decreased upon nanotube gating, a red-shifted peak emerged as evident from **Figure 4.7a, c** and from **Figure 4.9**, which shows the evolution of this low-energy peak relative to the E_{11} emission. It can be assigned to the formation of positive or negative trions depending on the sign of the gate bias. In agreement with previous studies,[24] the emission energy of the positive trion (1.045 eV) was slightly higher than the energy of the negative trion (1.040 eV). Increasing the gate bias resulted in a blueshift of the trion emission (see **Figure 4.11b**). Similar to the above-discussed blueshift of the exciton, this is likely caused by a reduced trion binding energy. As observed previously, the trion blueshift was generally smaller than the E_{11} blueshift possibly due to a concomitant charging-induced increase in singlet-triplet exciton splitting (see Section 2.2).[27]

The E_{11}-normalized gating-dependent PL spectra (see **Figure 4.9**) and a plot of the evolution of the fitted trion/exciton ratio (see **Figure 4.11c**) reveal an initial increase with charge carrier

Table 4.2: Maximum blueshifts of the E_{11} peak (in meV) upon accumulation of holes and electrons.

	AF2400	P(VDF-TrFE-CTFE)	PMMA	PS	HfO_x
hole accumulation	5.5	11.1	10.1	4.6	9.3
electron accumulation	2.7	6.7	9.4	6.9	11.9

density up to a maximum, followed by a subsequent decline upon further charge accumulation for many FETs. This behavior may arise from a substantial reduction in E_{22} absorption and additional Auger quenching of excitons at higher charge carrier densities, resulting in low numbers of excitons available for trion formation.[24,27] While such a trend can be expected for all FETs irrespective of the primary dielectric material, it could not be observed for some devices due to the lower dielectric breakdown strength. There, early device breakdown prevented the accumulation of sufficiently large amounts of charge carriers. In case of positive charging of SWCNTs in FETs with PS as the primary gate dielectric, the positive trion/exciton ratio seemed particularly far away from its maximum. This device was therefore excluded from the following analysis.

Figure 4.11c shows that much like the differences observed in exciton quenching and blueshift, the maximum trion/exciton ratios exhibited variations across the FETs with different primary gate dielectrics and further depended on the sign of the induced charge carriers. Furthermore, the maxima were reached at different carrier densities, usually below 10^{13} cm^{-2} except for devices with HfO_x dielectric, for which the maximum of relative positive trion intensity occurred at a particularly high hole density of 2.5×10^{13} cm^{-2} (not shown in Figure 4.11c for reasons of clarity, but evident from **Figure 4.9**). Again, no clear trend with the dielectric constant or refractive index of the immediate nanotube environment was observed, and a simple electrostatic stabilization of the charged trions over the charge-neutral excitons depending on the dielectric properties can be excluded. Instead, a correlation with the charge trapping properties of the primary dielectric materials seems likely, analogous to the charge-induced quenching and peak shifting discussed above. Specifically, the lowest negative trion/exciton ratios were reached for FETs with the electron-trapping fluorinated dielectrics Teflon AF2400 and P(VDF-TrFE-CTFE), and the lowest positive trion/exciton ratio occurred for SWCNTs in contact with the hole-trapping HfO_x. PMMA as primary gate dielectric supported the most equivalent positive and negative trion/exciton ratios, in agreement with its fairly balanced hole and electron transport properties (see **Figure 4.4** and **Table 4.1**).

4.6 Charge localization and energetic trion stabilization

As discussed above, the dielectric parameters of the environment alone have proven insufficient to explain the distinct trends in charge transport and PL that were observed upon variation of the gate dielectric material and gate voltage. A model introduced by Eckstein *et al.*,

which describes the photoluminescence properties of chemically and electrochemically doped (6,5) SWCNTs in the context of inhomogeneous charge carrier doping, might help to understand this unexpected behavior of electrostatically gated carbon nanotubes in different environments.[141,247] According to their analysis, charge carriers become localized on the nanotubes in charge puddles due to interactions with poorly screened exohedral counterions that induce shallow local charge traps. Thus, the SWCNT becomes segmented into charged and uncharged compartments. While trion emission originates from the charged segments, excitons are formed in the uncharged areas which exhibit variable lengths. If the charge puddles are well-separated, that is, at low doping levels, excitons are likely to radiatively decay in the uncharged segments. Increasing the doping level, a diffusive encounter of excitons with a charge localized in a charge puddle becomes more likely, enhancing non-radiative exciton transition through either Auger quenching-induced decay or trion formation. The spatial confinement of excitons in uncharged nanotube segments further increases their energy, thus adding to the spectral blueshift.

Electrostatic doping in a solid-dielectric field-effect transistor configuration does not rely on ionic interactions. It should thus present an example of homogeneous nanotube doping, with free charge carriers distributed along the nanotube length (see **Figure 4.12a**). As a consequence, the diffusing exciton should encounter charge carriers with a high probability

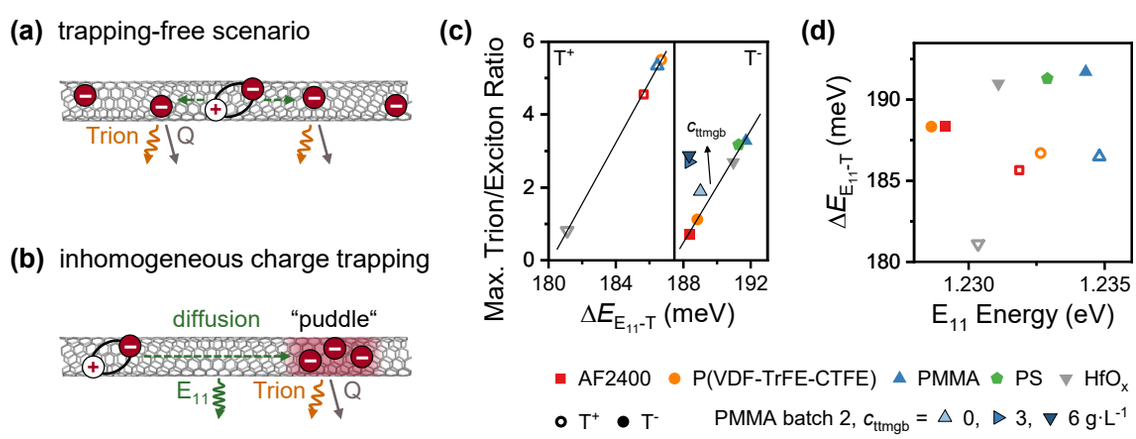

Figure 4.12: a) Schematic of homogenous charge carrier distribution in a trap-free SWCNT proposedly leading to pronounced trion formation and exciton quenching (Q) as opposed to b) localization of charge carriers in charge puddles which would enhance the probability of radiative E_{11} decay. c) Linear fits of the correlation of the maximum positive (open symbols) and negative (solid symbols) trion/exciton ratios with the trion-exciton energy separation. Framed symbols represent results from ttmgb treatment of FETs with PMMA as primary dielectric (see Section 4.7), prepared from another batch of SWCNTs. d) Exciton-trion energy separation versus E_{11} emission energy.

everywhere on the SWCNT, leading to strong exciton quenching and a high relative trion intensity. The strong exciton confinement resulting from the short average diffusion lengths should further cause a pronounced exciton blueshift. Such PL behavior was observed for FETs with primary dielectrics that did not induce significant charge trapping, like PMMA for both holes and electrons, P(VDF-TrFE-CTFE) for holes, and HfO_x for electrons as discussed above.

However, in case of strong charge trapping, *i.e.*, for electrons in FETs with fluorinated polymers and holes in FETs with HfO_x as primary dielectrics, reduced exciton quenching and lower relative trion intensities were observed. Applying the model of inhomogeneous trapping, these charge carriers would be localized in puddles inhomogeneously distributed along the SWCNT, leading to an increase in average exciton diffusion length compared to the homogenous scenario (see **Figure 4.12b**). Thus, excitons should be less likely to interact with charge carriers within their lifetime, resulting in reduced exciton quenching and lower relative trion intensities besides the reduced exciton blueshift, as observed in case of FETs with charge-trapping primary dielectrics.

An additional factor influencing trion formation and maximum relative emission intensities could be an energetic stabilization of the trion over the exciton, represented by the energy separation between excitons and trions, ΔE_{E11-T} (see Section 2.2). While no clear dependence of ΔE_{E11-T} on the dielectric constant of the nanotube environment was observed, the maximum trion/exciton PL ratio increased linearly with trion-exciton energy separation (see **Figure 4.12c**). Note that, in accordance with previous studies,[24] the energy separation was always smaller for positive (181 – 187 meV) than for negative trions (188 – 192 meV) as a result of the minor differences in effective mass of holes compared to electrons within small-diameter SWCNTs.[23] Nonetheless, the slopes of the respective linear correlations were similar for positive and negative trions (~ 0.8 per meV of ΔE_{E11-T}). This similarity suggests a common physical origin, which might be associated with the above-discussed segmentation of the nanotubes through localized charge carriers. Furthermore, the trion-exciton energy separation exhibited an overall increase with E_{11} energy (see **Figure 4.12d**). Previous investigations by Tanaka *et al.* across a wider E_{11} emission energy range revealed a linear dependence, which they attributed to a power-law scaling of the interaction energies of trions and excitons with the dielectric constant of the environment.[36] The non-linear behavior and the trion polarity-dependence shown in **Figure 4.12d** once more indicate that the dielectric environment may not be the only determining factor in case of SWCNT networks integrated into FETs, even though a definitive explanation of the observed behavior remains elusive.

4.7 Gated photoluminescence after removal of charge traps

As discussed in the preceding sections, the investigations on the dielectric- and polarity-dependent electrical and optical properties of carbon nanotube networks in FETs point towards charge trapping as a critical factor for suppression of both trion formation and exciton quenching. Yet, some effects from the dielectric constant of the nanotube environment cannot be excluded. Precise control of the trap density within a selected dielectric environment could provide additional insights into the role of charge carrier trapping. Such a study will further bear the advantage of better comparability of trap densities, since the different non-ideal electrical characteristics of the various dielectrics used in the previous sections (see **Figure 4.4**) did not allow for consistent trap density extraction from the subthreshold swing following Equation (12).

1,2,4,5-Tetrakis(tetramethylguanidino)benzene (ttmgb) has previously been used to improve electron transport in FETs based on (6,5) SWCNT networks.[143,228] The guanidino-functionalized aromatic ttmgb is a strong base and reducing agent capable of donating two electrons, thus removing external electron traps related to residual adsorbed water or oxygen (see **Figure 4.13a**). The compound was further found to improve electron injection and block hole injection by lowering the work function of gold electrodes by around 1 eV.

To investigate the impact of different trap densities on the optical properties of gated (6,5) SWCNTs, FETs with PMMA as the primary gate dielectric were fabricated. Prior to the deposition of PMMA, the substrates (SWCNT networks on gold electrodes) were dip-coated

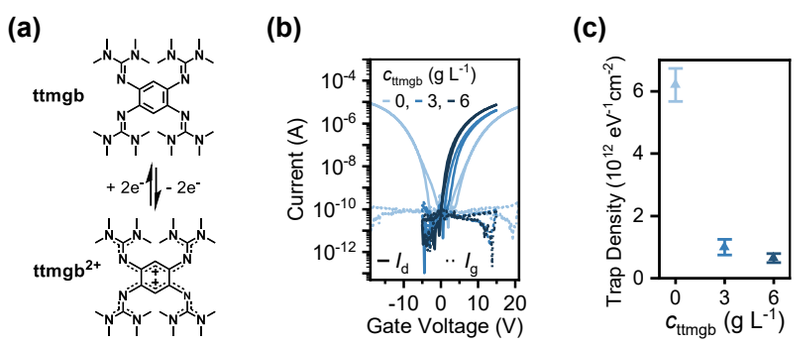

Figure 4.13: a) Molecular structure and reversible redox behavior of ttmgb. b) Transfer characteristics of (6,5) SWCNT network FETs with PMMA as the dielectric in contact with the nanotubes (L = 20 µm, W = 10 mm, V_d = 0.01 V), treated with different concentrations of ttmgb. c) Density of electron traps versus the ttmgb concentration, calculated from the subthreshold swing.

into anhydrous toluene solutions with different ttmgb concentrations c_{ttmgb} = 0 (reference), 3 and 6 g·L^{-1} (see Section 3.1.4).

Figure 4.13b shows the usual impact of ttmgb treatment on the FET transfer characteristics, that is, purely *n*-type charge transport without hole current and a slight shift of onset voltages towards negative gate voltage with increasing ttmgb concentration[143,228] Analysis of the slopes in the subthreshold regime (see Section 3.2.5) further revealed the expected significant reduction of electron trap densities by nearly an order of magnitude upon treatment with ttmgb (see **Figure 4.13c**).

The untreated reference sample exhibited PL quenching, E_{11} and trion blueshift and peaking trion/exciton ratios upon gating as expected and discussed in the previous sections. The maximum negative trion/exciton ratio (see **Figure 4.14**) was, however, lower than the maximum observed for the nanotubes in contact with PMMA in the dielectric comparison series. Yet, the trion-exciton energy separation was also reduced in the ttmgb reference sample, thus fitting well into the linear correlation of maximum trion/exciton ratios and trion-exciton separation established in the dielectric comparison study (see **Figure 4.12c**). This observation further suggests that the role of the dielectric environment in trion stabilization cannot be neglected, since the nanotube networks from the ttmgb and the dielectric variation series can be expected to experience slightly different environments as they were deposited from different SWCNT stock dispersions.

The ttmgb-treated samples also showed the expected gating-dependent emission behavior. The maximum trion/exciton PL ratios differed from the reference nanotubes. As evident from **Figure 4.14**, increasing the concentration of ttmgb resulted in higher relative trion PL

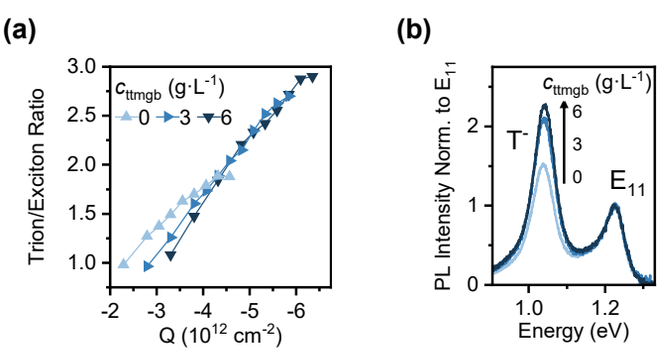

Figure 4.14: a) Evolution of the trion/exciton ratio with charge carrier density for FETs with PMMA dielectric for different ttmgb concentrations. b) Corresponding PL spectra at the respective maximum trion/exciton ratios.

intensities as expected from samples with reduced electron trap densities (see Section 4.6). The charge carrier density at which the respective maximum was reached also increased with c_{ttmgb}, possibly because of the lower share of localized charge carriers.

Note that the rise in maximum trion/exciton ratio with increasing c_{ttmgb} was not accompanied by an increase in trion-exciton energy separation (see **Figure 4.12c**). While this finding is surprising and should be further investigated, the effects observed upon ttmgb treatment overall support the proposed crucial role of charge carrier localization on trion formation and stabilization. Since the effects were rather moderate compared to the broad range of maximum trion/exciton ratios upon dielectric variation, it can further be assumed that dielectric environment-induced charge traps have a greater impact on charge localization than charge traps that are intrinsic to the network or substrate.

4.8 Summary and conclusion

This chapter presented a systematic study of the influence of the dielectric properties and charge traps associated with the environment on trion and exciton photoluminescence in electrostatically charged (6,5) SWCNT networks. The networks were integrated into top-gate/bottom-contact field-effect transistors, allowing for the investigation of both positive and negative trions within the same environment. The material of the gate dielectric in contact with the nanotubes as the adjustable component of their immediate environment was varied to cover a broad range of dielectric constants. Moreover, the nanotubes were treated with the reducing agent ttmgb to remove shallow electron traps and thus gain further insights into the impact of charge localization on the emission of charged SWCNTs.

In the uncharged state, only excitonic PL was observed from the (6,5) SWCNT networks. The E_{11} emission energies (widths) roughly showed the expected decrease (increase) with the dielectric constant of the nanotube environment. A trion peak emerged upon electrostatic gating of the nanotubes as a result of the formation and subsequent radiative decay of an exciton decorated with an additional hole or electron, as determined by the sign of the gating-induced charge carriers. Importantly, the gating-dependent exciton and trion PL properties did not exhibit a clear trend with the dielectric environment and even varied within one dielectric material depending on the polarity of the induced charges. Combined analysis of the electrical and optical characteristics pointed towards a correlation with the electron and hole trapping properties of the primary gate dielectrics instead. The electron-trapping fluorinated polymers

caused weaker exciton quenching, smaller exciton blueshift and lower trion/exciton ratios upon accumulation of electrons than upon hole accumulation. Devices with the hole-trapping HfO_x as gate dielectric showed the opposite trends. The balanced ambipolar transport of FETs with PMMA as primary gate dielectric accordingly resulted in a more symmetrical gated-PL behavior. The crucial role of charge carrier trapping was further corroborated by the observed increase in maximum trion/exciton ratio when external electron traps were reduced using ttmgb.

The findings may be attributed to the localization (trapping) of charge carriers in so-called charge puddles, a model initially developed to explain the specific optical properties of excitons in chemically doped SWCNTs as a consequence of the Coulomb interactions of charges on the nanotubes with counterions.[141,247] The resulting segmentation of the nanotubes into neutral and heavily charged sections could explain the different gating-dependent emission behavior compared to the interaction of the excited states with homogeneously distributed charge carriers in a trap-free scenario. In complex systems like FETs, trion and exciton PL from SWCNTs are therefore not only governed by their environment, but also by the operated charge carrier polarity. Unwanted trion emission from optoelectronic devices could consequently be suppressed through the deliberate introduction of charge traps, however, at the expense of charge carrier mobility. Moreover, the results show that neither the trion/exciton ratio nor the E_{11} blueshift in emission can serve as a universal metric for carrier density quantification as it already varies within different devices and for different charge carrier polarities.

5. Introduction of luminescent oxygen defects into (6,5) SWCNT networks

This chapter describes a solid-state approach to creating luminescent oxygen defects in networks of polymer-wrapped SWCNTs on reactive transition metal oxides. The presented method eliminates the necessity for wet-chemical processes and enables the introduction of defects with spatial precision. The content of this chapter, including versions of the presented figures and tables, was published by the American Chemical Society in the article Wieland *et al.*, *J. Phys. Chem. C* 2024, 128, 2012 – 2021.[248]

5.1 Introduction

The introduction of luminescent defects to single-walled carbon nanotubes offers the opportunity to enhance their optical properties and tune their emission energy within the near-infrared spectrum as detailed in Section 2.3. Specifically, the photoluminescence quantum yield (PLQY) of SWCNTs can be improved by capturing mobile excitons at energetically lower-lying defect sites, thereby preventing the nonradiative decay of excitons at quenching sites.[20,52] Such exciton trapping at local potential minima results in near-infrared (nIR) emission that is red-shifted compared to free exciton emission.

A common type of defects are sp^3 defects, where the specific energy of the transition (E_{11}* and E_{11}*$^-$) relies on the precise defect binding configuration,[41] modifiable through choice of synthetic method.[42–44] Similarly, oxygen defects in SWCNTs (see **Figure 5.1a**) exhibit configuration-dependent emission spectra and improved PLQY.[19,195,204] Calculations suggest that the typically observed ether-d defect represents the most stable configuration.[19,195] The formation of the even more red-shifted epoxide-l configuration has also been reported. Solution-based methods commonly involve reactive species like ozone[19,45,195,201] and other oxidants,[19,205] while solid-state introduction of oxygen defects has been achieved through

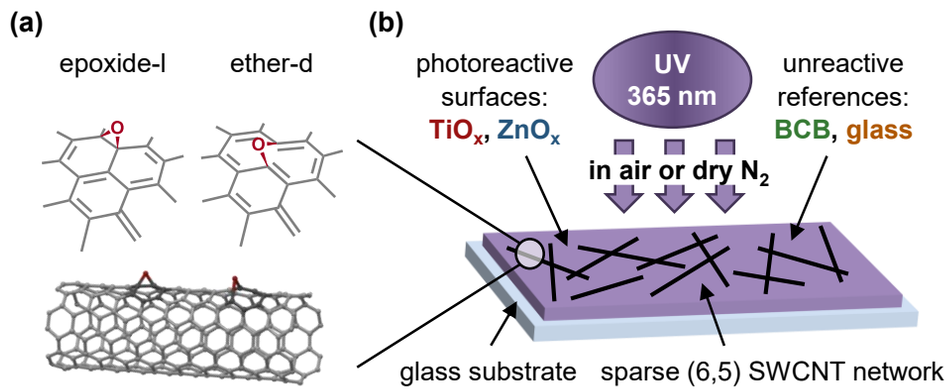

Figure 5.1: a) Luminescent defect configurations reported in literature. b) Schematic of the solid-state oxygen defect functionalization approach. A sparse, annealed (6,5) SWCNT network on a series of photoreactive and unreactive substrate materials is exposed to UV light in air or dry nitrogen atmosphere.

electron-beam evaporation of metal oxides[46,208] and upon treatment of SWCNT thin films in a conventional UV-ozone cleaner.[213]

As opposed to the deliberate oxygen functionalization, unintentional oxidation of carbon nanotubes during sample processing and storage under ambient conditions can pose a significant challenge for long-term stability.[15] Even though SWCNTs are generally perceived as highly stable with respect to optical and thermal stressors,[1,2] carbon nanotubes can exhibit altered charge transport and emissive properties that often display signs of defect formation in proximity to polar substrates.[55] Yet, this apparent ease of defect introduction also presents an opportunity to create oxygen defects with simple methods that do not require intricate chemical methods and reaction work-up procedures. Interfacing SWCNTs with reactive materials such as titanium dioxide and zinc oxide could open up ways to simplify carbon nanotube functionalization, which is critical for potential applications in fields like room-temperature single-photon emission.[46]

The transition metal oxides TiO_2 and ZnO are known for their photocatalytic activity, which has been investigated in various contexts, including the degradation of organic pollutants and water splitting to generate hydrogen and green fuels.[249,250] Excitation of the oxides above their bandgap (~ 3.2 eV) generates electron-hole pairs that undergo surface redox reactions with water and oxygen to form hydroxy radicals $HO^{\bullet}$ and superoxide radical anions $O_2^{-\bullet}$ as shown in **Figure 5.2**.[251–253] These highly reactive oxygen species (ROS) readily react with conjugated aromatic systems.[250] Combination of the photoreactive TiO_2 and ZnO with (6,5) SWCNTs, which exhibit a relatively small diameter and therefore high strain that enhances their lattice

reactivity,[20,254] presents a promising approach to controlled oxygen functionalization of carbon nanotubes.

This chapter focuses on the UV-induced introduction of luminescent, red-shifted oxygen defects into sparse networks of (6,5) SWCNTs deposited on photoreactive oxidic surfaces as outlined in **Figure 5.1b**. The investigation covers the exploration of different experimental conditions, optical and thermal trap depths, and decay dynamics associated with these defects. The presented solid-state approach is further used to introduce patterns of luminescent defects with micrometer precision. In contrast to prior strategies for defect photopatterning,[53,255] this method does not necessitate the use of additional chemicals or solvents.

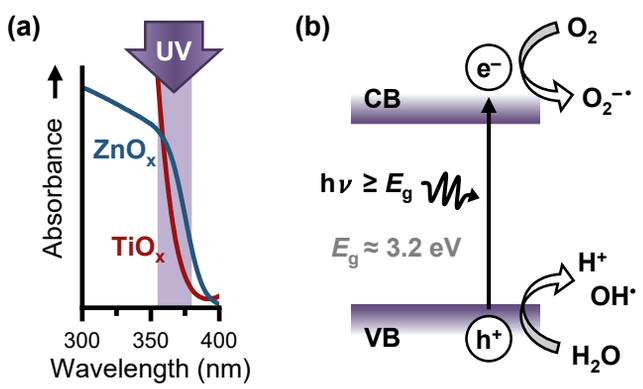

Figure 5.2: a) UV-Vis spectra from the band edge of TiO_x and ZnO_x thin films (purple box and arrow: UV wavelength range used in this study) and b) energetics of their photoexcitation, inducing a redox reaction of the photogenerated electrons and holes with oxygen and water to form reactive oxygen species (CB – conduction band, VB – valence band).

5.2 Functionalization strategy and sample preparation

As schematically shown in **Figure 5.1b**, a range of photoreactive (TiO_x, ZnO_x) and non-reactive reference materials (cross-linked divinyltetramethylsiloxane-bis-benzocyclobutene (BCB), glass) served as substrates to investigate the introduction of oxygen defects into networks of polymer-wrapped (6,5) SWCNTs upon UV irradiation at the band edge of the photoreactive oxidic substrates.

Pinhole-free thin films of all substrate materials were created on glass substrates from organic and inorganic precursors through solution-deposition techniques with successive post-treatment (see Section 3.1.1). Note that the amorphous nature of the transition metal oxides, as specified by the supplier in case of titanium dioxide and apparent from the absence of a sharp absorption peak at 350 nm for zinc oxide (see **Figure 5.2a**),[256] implies variations in their exact stoichiometry. The oxides are thus denoted as TiO_x and ZnO_x throughout this chapter. While the transition metal oxides were selected for their oxidizing capabilities upon photo-excitation as discussed above, glass was chosen as a reference due to its widespread use as substrate for optoelectronic devices.[55] BCB has recently been found to beneficially impact nanotube spectroscopy due to its low polarity and reduced dipolar disorder,[55] and was hence included in the measurement series.

Nearly monochiral (6,5) SWCNT dispersions were prepared by shear-force mixing in the presence of PFO-BPy as the chirality-selective wrapping polymer and subsequent redispersion in toluene to remove excess PFO-BPy (see Section 3.1.2). Representative atomic force micrographs of SWCNT networks, deposited onto the different substrates by triple spincoating of the dispersions, are displayed in **Figure 5.3**. The surface material did not significantly influence the network density of ~ 10 nanotubes per µm even though the surface roughness of the materials varied strongly, with the oxidic surfaces exhibiting a much higher roughness than the polymeric BCB layer and pristine glass. The surface and potential network density inhomogeneities did not significantly affect the experimental results or reproducibility due to averaging of Raman spectra across an extended area and the use of an expanded beam configuration for the photoluminescence (PL) measurements (see Sections 3.2.4 and 3.2.6). The low nanotube density enabled efficient UV absorption by the underlying substrate and

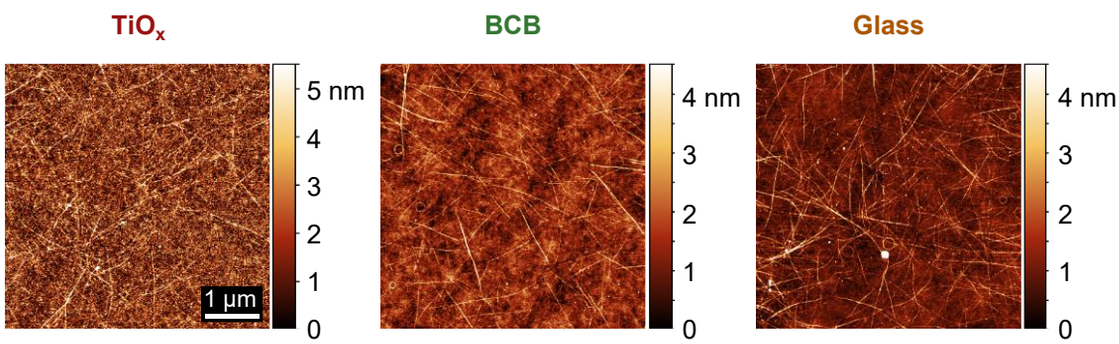

Figure 5.3: Atomic force micrographs of TiO_x, BCB and glass surfaces with spincoated sparse networks of (6,5) SWCNTs. The surface roughness of the ZnO_x network was too high to allow for characterization by AFM.

ensured that all SWCNTs were in contact with the underlying surface. Close proximity between the nanotubes and the reactive surface is essential as the photoreaction is expected to take place near the surface due to the short lifetime and accordingly limited diffusion distance of the ROS.[251,257] Further, the coverage of the nanotube surface with wrapping polymer (~ 10 % surface coverage)[237] and the minor residual content of excess polymer that might still be present even after thorough washing of the SWCNT filter cake (see Section 3.1.2) are identical within one sample batch. Note that although coverage with polymer or surfactant can potentially limit the access of reagents to the carbon lattice,[205,208] and certain wrapping agents may participate in reactions competing with the SWCNT functionalization,[215] Larson *et al.* found the efficiency of oxidative (6,5) nanotube degradation to be independent of the amount of excess PFO-BPy.[15] They attributed their observation to a substantial oxygen permeability of the wrapping polymer.

The pristine SWCNTs exhibited PL spectra with the distinct and narrow excitonic E_{11} emission at 1.229 eV, accompanied by red-shifted sidebands that are common to nanotube networks

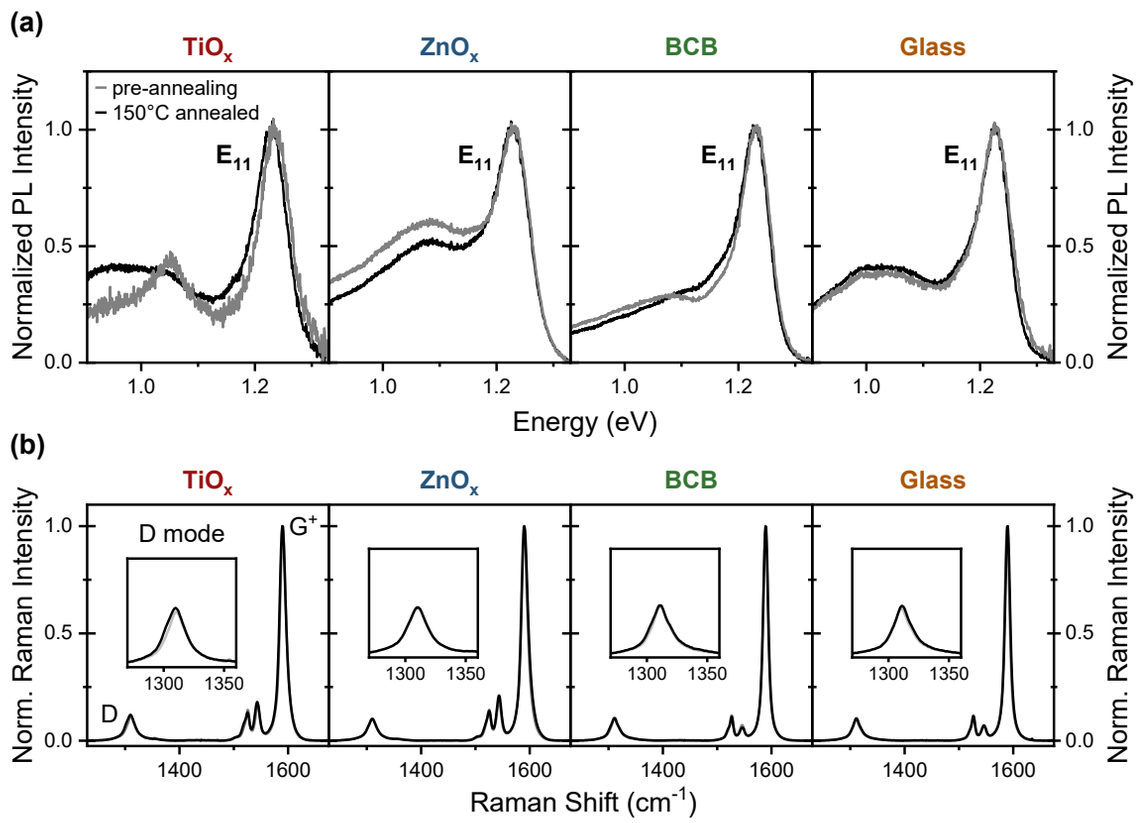

Figure 5.4: a) PL spectra and b) averaged Raman spectra of (6,5) SWCNT networks on the surfaces under investigation before and after mild annealing at 150 °C, normalized to the E_{11} PL and Raman G^+ mode intensity, respectively.

(see **Figure 5.4a**). These sidebands have been associated with the coupling of momentum-forbidden dark excitons to phonons and shallow extrinsic defects in the nanotube lattice that are formed as a consequence of interactions with reactive groups primarily present on polar surfaces.[104,112,113] The contributions of the sidebands to the PL spectra correspondingly increased from non-polar to polar, and from inert to reactive substrates (see **Figure 5.4a**) in agreement with previous investigations.[55,258] Notably, the discernible feature at 1.051 eV in the TiO_x sample likely arises from trion (charged exciton) emission from the (6,5) SWCNTs due to a *p*-doping effect from the underlying oxide.[232] The relatively high sideband intensities even for the non-polar BCB samples probably results from the very low carbon nanotube network density. As a result, the nanotubes experience less shielding from adjacent SWCNTs than in dense networks, making them more susceptible to interactions with their environment and unintended reactions.

Prior to further functionalization experiments, all SWCNT networks underwent gentle annealing at 150 °C in a dry nitrogen environment. The annealing step was included to remove adsorbed water and oxygen from both the SWCNT and the substrate surfaces, ensuring consistent initial conditions for all samples. Both the SWCNT PL emission profiles and Raman D/G^+ ratios, which serve as indicators for lattice defects in carbon nanotubes (see Section 3.2.4),[207,230] remained largely unaffected by the annealing process (see **Figure 5.4**), implying negligible impact of the thermal treatment on the nanotube integrity. Only for the highly reactive TiO_x, minor signs of thermally induced defect formation were observed as the distinct trion feature vanished while a broad red-shifted sideband, similar to the sideband on glass, appeared together with a slight increase in the Raman D/G^+ ratio.

5.3 UV-induced lattice oxidation in air

The simplicity of an experimental method plays a crucial role in making it practical for larger-scale applications. Exposure of SWCNT networks on reactive surfaces to UV light in ambient air could present such a low-effort approach to the introduction of specific oxygen defects. The distinct features of luminescent defects were however not observed in any of the PL spectra (see **Figure 5.5a**). Instead, the PL of these SWCNTs was quenched upon UV exposure in air together with a strong increase in Raman D/G^+ ratios (see **Figure 5.5b**). These changes to PL and Raman spectra occurred within a very short period of less than 30 minutes and even less than 2 minutes in case of TiO_x. Specifically, the PL intensity decayed nearly linearly with UV illumination time for SWCNTs on the reference substrates BCB and glass down to 16%

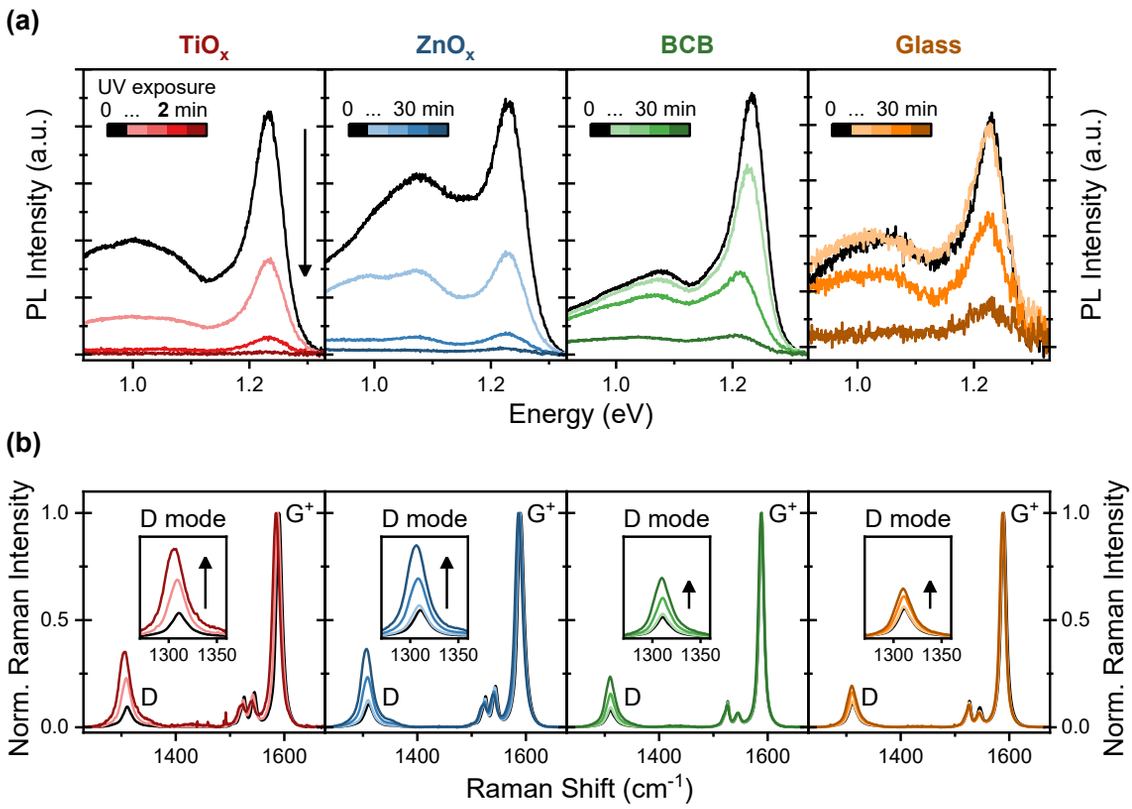

Figure 5.5: Time-dependent a) PL and b) Raman spectra of (6,5) SWCNTs on photoreactive and unreactive surfaces upon UV illumination in air for 0, 2, 15 and 30 min (TiO_x: 0, 5, 25, 120 sec).

of the initial PL intensity, while the PL resembled an exponential drop with near-complete PL quenching on the oxides (down to 1 and 3 % of initial PL intensity for TiO_x and ZnO_x, respectively, see **Figure 5.6a**). In contrast, the D/G^+ ratios increased approximately linearly for SWCNTs on all substrate types (see **Figure 5.6b**). The different slopes of these changes to the D/G^+ ratios resulted in a final D/G^+ ratio increase of 0.2 to 0.3 on the reference substrates, and of up to around 0.5 on the photoreactive transition metal oxides.

The very high Raman D/G^+ ratio increase, strong PL quenching and the absence of distinct defect bands suggest the rapid creation of structural defects in the nanotube lattice upon UV exposure in air since lattice degradation can lead to significant non-radiative decay of excitons in SWCNTs.[15,259] The different temporal dependencies of the PL intensities of SWCNTs deposited on the oxides compared to the BCB and glass reference substrates (see **Figure 5.6a**), in contrast to the near-linear D/G^+ ratio evolution on all substrates (see **Figure 5.6b**), could indicate different mechanisms of defect introduction.

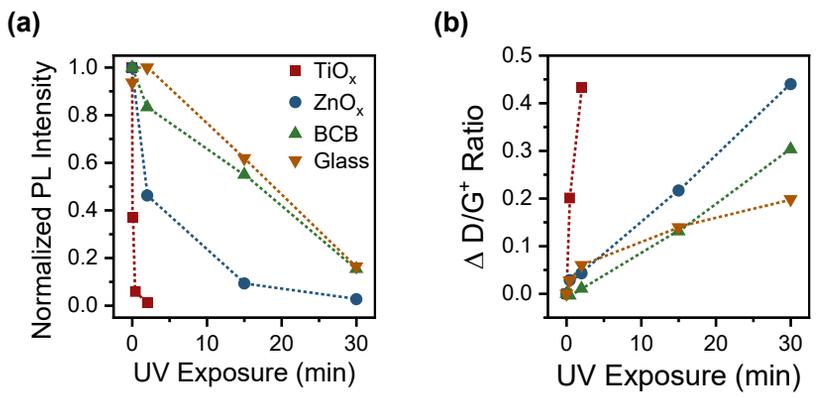

Figure 5.6: Temporal evolution of a) integrated total PL intensities, normalized to the pristine intensities, and b) Raman D/G^+ ratio changes of (6,5) SWCNTs on photoreactive and unreactive surfaces upon UV illumination in air.

The significant photodegradation of SWCNTs on the nominally passive reference substrates might be caused by UV-induced singlet oxygen sensitization or direct excitation of the SWCNTs and concomitant superoxide formation from oxygen, as proposed by Larson *et al.*[15] These ROS could potentially initialize a chain reaction with the excess of oxygen and/or water present in air, leading to the formation of highly oxidized compounds similar to findings in less-extended aromatic species.[250] Specifically, sidewall damage comparable to the effects observed from superoxide treatment and oxidative cutting of carbon nanotubes can be expected. These processes typically involve the generation of hydroxyl, ketone, aldehyde, and carboxylic acid defects which are capable of exciton quenching, consequently reducing PL intensity.[15,260,261] Note that the direct ROS creation from air through UV activation of molecular oxygen as demonstrated by Xhyliu *et al.*[215] is unlikely. The energy of the 365 nm (3.4 eV) light utilized in the presented work is below the threshold necessary for this particular process, which would require excitation with wavelengths of around 254 nm (4.88 eV).[215] However, the energy of the employed UV light is notably higher than the bandgap energies of TiO_x (3.19 eV) and ZnO_x (3.29 eV) as determined by Tauc plots.[262] Consequently, the presence of an additional, prevailing mechanism seems plausible for nanotubes deposited on TiO_x and ZnO_x. and would explain the more rapid SWCNT decay on the photoreactive compared to the reference substrates. The degradation mechanism could rely on the generation of surplus amounts of reactive oxygen species, such as $HO^{\bullet}$ and $O_2^{-\bullet}$, as a result of metal oxide photoexcitation in the water- and oxygen-rich ambient atmosphere. These ROS are expected to initiate chain reactions as discussed above.

5.4 UV-induced luminescent oxygen defect introduction under inert conditions

The amount of oxygen present during the UV exposure should be reduced to enable oxygen defect introduction in a more controlled manner as compared to the photoreaction in air (see Section 5.3). Utilizing the dry nitrogen atmosphere of a glovebox, the photoreaction can be performed under defined conditions in the presence of sub-ppm levels of oxygen and water. In addition, the mild annealing of the SWCNT networks (see Section 5.2) will further remove adsorbed oxygen and water. Yet, trace amounts of both molecules will remain present on the surface even after such treatment and are consequently expected to participate in the photoreaction.

Figure 5.7 shows the temporal evolution of PL emission from (6,5) SWCNTs on photoreactive and unreactive substrates upon UV treatment for up to 30 minutes in dry nitrogen atmosphere, together with the corresponding Raman spectra in the D and G mode range. Under these conditions, the shapes of the PL spectra of nanotube networks on BCB and glass exhibited minimal changes, and the D/G^+ ratios remained largely unchanged, indicating no significant introduction of luminescent or exciton-quenching defects. Only some PL intensity variations were observed on glass substrates. Since these variations showed no consistent trend with UV exposure time and were not accompanied by changes in the relative Raman D band intensity, they could be attributed to nanotube deposition and density issues rather than to damaging of the carbon lattice.

The resilience of nanotubes on the reference substrates against UV exposure contrasts sharply with their counterparts on photoreactive oxidic surfaces. Specifically, following the UV treatment of (6,5) SWCNTs on TiO_x and ZnO_x, two additional red-shifted emission peaks, labeled as E_{11}^* (1.10 eV, 1130 nm) and E_{11}^{*-} (0.95 – 0.97 eV, 1280 – 1300 nm), emerged and gained spectral weight as the exposure time increased (see **Figure 5.7a, b**). The D/G^+ ratios increased by around 0.2 after 30 min of UV illumination (see **Figure 5.7c**), however, not to an extent that would inherently imply severe lattice damage.[42,197] Therefore, the concomitant changes of the PL emission profile can be attributed to trapping of excitons at luminescent defect sites.

The full width at half maximum (FWHM) of the E_{11}^* and E_{11}^{*-} emission was higher than the FWHM of the E_{11} band (E_{11}^{*-}: 214 meV and 163 meV, E_{11}^*: 96 meV and 86 meV, E_{11}: 50 meV and 55 meV on ZnO_x and TiO_x, respectively). Ma *et al.* attributed similar observations to a higher sensitivity of the defect peaks to the local environment.[195] They argued that the localized

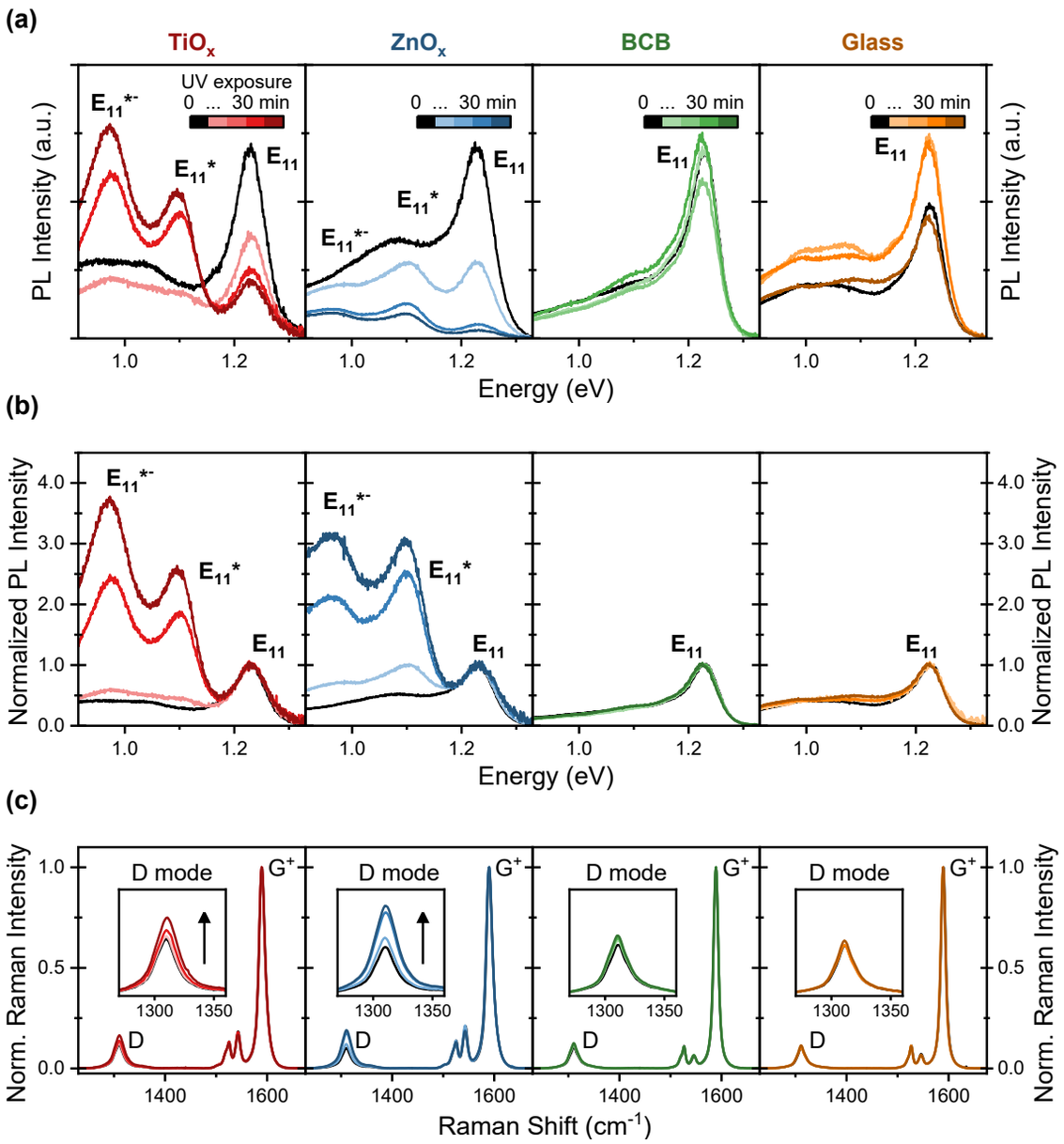

Figure 5.7: a) PL spectra, b) PL spectra normalized to E_{11}, and c) Raman spectra of the pristine (6,5) SWCNTs on different surfaces after UV illumination for 0, 2, 15 and 30 min.

nature of defect-trapped excitons makes them more susceptible to fluctuations in the local potential or dielectric constant, unlike to free excitons, which are less affected as they experience such variations averaged across the spatial extent of their wavefunction.

Notably, the spectral shapes as well as the absolute and relative intensities of the two different defect emission features depended strongly on the underlying substrate. Both E_{11}^* and E_{11}^{*-} emission were significantly broadened for SWCNTs on ZnO_x with respect to the TiO_x

samples. Since the phenomenon of peak broadening has previously been associated with dipolar disorder,[125,258] this observation could be due to the rougher ZnO_x surface and thus higher dipolar disorder compared to TiO_x. The relative oxygen defect intensities were higher for nanotubes on ZnO_x compared to their TiO_x counterparts (see **Figure 5.7c** and **Figure 5.8a, b**). However, the functionalized SWCNTs on ZnO_x showed an overall PL intensity reduction compared to the pristine state, whereas the TiO_x samples where brightened by a factor of around 3 after 30 min of UV exposure (see **Figure 5.8c**). This loss of PL intensity on ZnO_x could possibly result from a higher number of non-emissive defects compared to their counterparts on TiO_x, which would lower both the free and trapped exciton emission intensities.[205]

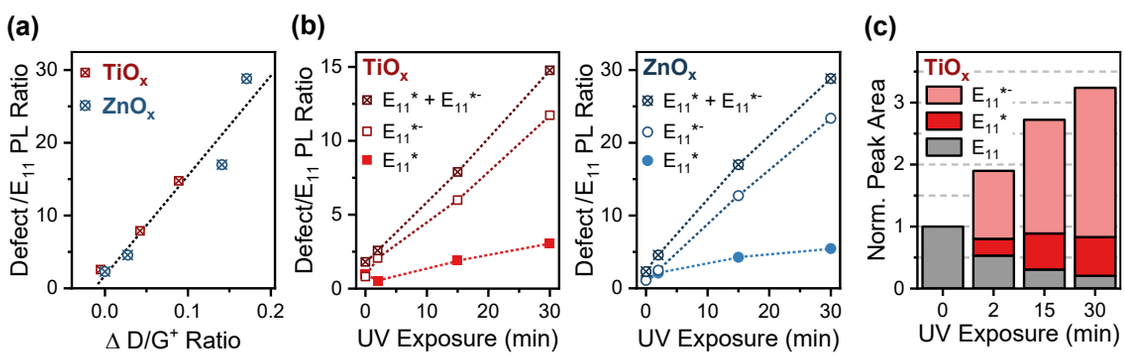

Figure 5.8: a) Correlation between the combined E_{11}^* and E_{11}^{*-} defect/E_{11} PL ratio and increase in Raman D/G^+ ratio. b) UV exposure time-dependent defect/E_{11} PL ratios of (6,5) SWCNT networks on TiO_x and ZnO_x. Dotted lines as guides. c) Free exciton and defect contributions to PL intensity of (6,5) SWCNTs on TiO_x upon UV irradiation, normalized to the exciton intensity of pristine SWCNTs. The PL intensities were obtained from Lorentzian multi-peak fits as described in Section 3.2.6.

The E_{11}^* and E_{11}^{*-} defect emission occurred with optical trap depths of 140 and 288 meV for oxygen defects on ZnO_x and 137 and 268 meV on TiO_x, respectively. These values closely resemble the trap depths of previously reported oxygen defect configurations denoted as ether-d (135 meV) and epoxide-l (300 meV).[195] Interestingly, the presence of both defect types has also been reported in previous investigations on solid-state defect introduction,[46,208,213] whereas most solution-based approaches to oxygen functionalization indicated the prevalent formation of ether-d defects.[19,205,208,210] While an environment-dependence of relative defect emission intensities[263] might contribute to this trend, reaction in dispersion could facilitate rearrangement into the more stable ether-d form.

The combined relative PL intensity of the two oxygen defect configurations scaled nearly linearly with the Raman D/G^+ ratio, and the slope was independent of the underlying oxide type (see **Figure 5.8a**). Such a linear correlation was observed previously for luminescent sp^3 defects,[42,197] where it could be used to quantify the absolute number of defects.[207] A similar correlation between D/G^+ ratio increase and the number of introduced defects presumably applies to oxygen defects as well. However, the gradient might diverge from that observed for sp^3 defects due to the differing hybridization states of the carbon atoms at oxygen defects.

The sub ppm-concentrations of water and oxygen maintained by the dry nitrogen atmosphere likely play a crucial role in the selective introduction of luminescent oxygen defects. The correspondingly low quantities of photogenerated ROS entail milder reaction conditions, in contrast to an abundance of ROS created in ambient conditions that causes significant lattice damage and substantial PL quenching (see Section 5.3). The near-linear increase of the defect PL intensities relative to the E_{11} emission (see **Figure 5.8b**) with exposure time indicates that the quantity of ROS directly relates to the illumination dose, implying the absence of an autocatalytic process or chain reaction. While discerning the specific roles of hydroxy radicals versus superoxide radical anions (see Section 5.1) remains challenging, a dominant role of the hydroxy radicals seems plausible due to their higher reactivity.[251–253] Additionally, water molecules are more persistent on polar surfaces even upon annealing, as opposed to the more facile removal of oxygen.

Previous research has employed direct bandgap excitation of carbon nanotubes to initiate electron transfer-related photoreactions, eliminating the necessity of high-energy UV light or reactive surfaces.[15,264] Yet, UV exposure of (6,5) SWCNTs yielded no alterations in the PL and

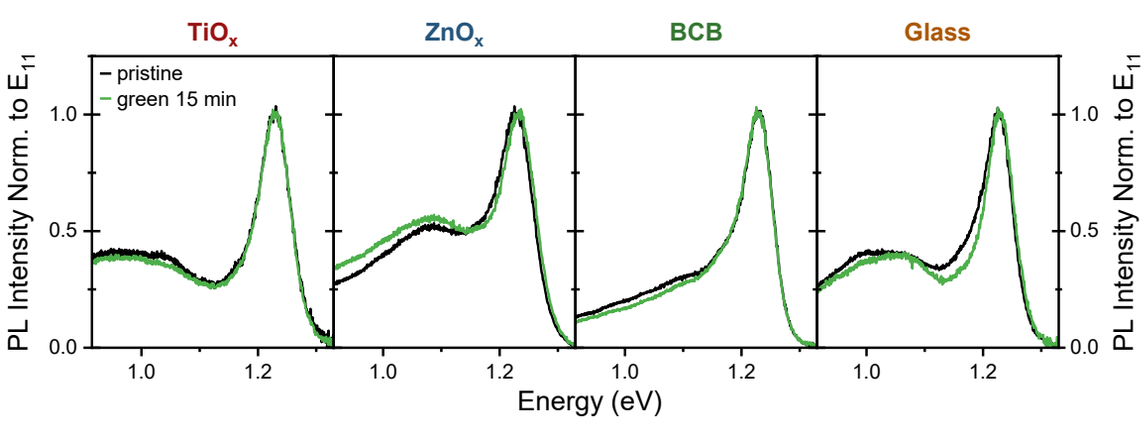

Figure 5.9: PL spectra of (6,5) SWCNT networks on the various surfaces under investigation before and after green light illumination for 15 min in dry nitrogen atmosphere.

Raman spectra of the nanotubes on inert substrates in this work (see **Figure 5.7**), even though the energy of the applied UV light was in resonance with the nanotube E_{33} transition. To explore possible effects of nanotube excitation further, SWCNTs were exposed to green light (525 nm, 2.36 eV) in a dry nitrogen atmosphere at intensities comparable to the previous UV irradiation to excite the nanotubes at the E_{22} and the phonon sideband. After 15 minutes of illumination, no discernible effect was observed in the PL spectra even for SWCNTs on the reactive surfaces (see **Figure 5.9**). This observation strongly suggests that excitation of the reactive oxides indeed plays a crucial role in oxygen functionalization of carbon nanotubes.

5.5 Properties of oxygen defects in SWCNT networks

The distinct characteristics of luminescent defects govern their characteristic PL dynamics and their temperature-dependent emission behavior. Time-correlated single photon counting and temperature-dependent PL experiments can therefore help to gain a deeper understanding of the created oxygen defects.

The E_{11}^{*-} defects exhibited longer radiative lifetimes (TiO_x 60 ps, ZnO_x 42 ps) than the E_{11}^{*} defects (TiO_x 26 ps, ZnO_x 25 ps), in agreement with their deeper optical trap depths (see **Table 5.1**).[200] Also, the defects on TiO_x displayed longer PL lifetimes in comparison to their counterparts on ZnO_x. This difference implies the presence of additional non-radiative decay routes, such as multiphonon decay (MPD) and electronic-to-vibrational energy transfer to the substrate and correlates with the observed stronger reduction in PL intensity for SWCNTs on ZnO_x versus on TiO_x.[134,200] For nanotubes on both oxides, the obtained lifetimes are shorter than previously observed (90 ps to 180 ps).[46,201,265] Note, however, that the reported lifetimes were mostly collected from functionalized nanotubes in dispersion, and that PL lifetime values are strongly affected by differences in shielding between network and dispersion, as well as between dense and sparse networks. The enhancement of nonradiative decay paths is well-known for pristine and sp^3-functionalized SWCNTs and has been linked to environmental effects.[55,129] For instance, sp^3 defects with lifetimes of 222 ps in toluene dispersion exhibited a significant lifetime reduction to 60 and 32 ps when deposited on nonpolar BCB and polar silicon dioxide substrates, respectively.[55]

To explore the thermal de-trapping behavior and associated thermal trap depths, temperature-dependent measurements between 25 and 300 K were performed on (6,5) SWCNTs on the photoactive surfaces, functionalized through 30 minutes of UV exposure in dry nitrogen.

Table 5.1: Optical (ΔE_{opt}) and thermal (ΔE_{therm}) trap depths and radiative lifetimes of oxygen defects in SWCNTs on TiO_x and ZnO_x substrates. The average lifetime values (τ_{avg}) consist of a long (τ_{long}) and short (τ_{short}) component with their respective amplitudes (A_{long}, A_{short}). n.d. – not determined.

		ΔE_{opt} (meV)	ΔE_{therm} (meV)	τ_{avg} (ps)	τ_{long} (ps)	A_{long}	τ_{short} (ps)	A_{short}
E_{11}*	**TiO_x**	137	100	26	184	0.01	25	0.99
	ZnO_x	140	14	25	183	0.01	24	0.99
E_{11}*$^-$	**TiO_x**	268	36	60	194	0.08	49	0.92
	ZnO_x	288	n.d.	42	162	0.05	35	0.95

Increasing the temperature from 25 K led to a rise in both E_{11}* and E_{11}*$^-$ defect emission intensity (see **Figure 5.10a**, **b**). This observation can be attributed to mobile excitons entering into trap states as their increasing thermal energy becomes sufficient to surpass potential barriers at the trap sites, and to the existence of an optically dark state below the bright defect state.[46,195,199,201] The relative defect emission intensity is expected to exhibit a peak and subsequent decline upon a further increase in temperature. Such reduction of the defect *versus* free excitonic emission should occur as the further increasing thermal energy enables thermal de-trapping of the localized excitons. On TiO_x, this peak occurred around 225 K for E_{11}* and E_{11}*$^-$ defects, while ZnO_x exhibited a maximum between 175 and 225 K for the E_{11}* defect configuration. Notably, a reduction of the relative E_{11}*$^-$ intensity was not observed within the experimentally accessible temperature range. Van't Hoff plots were constructed using the temperature-dependent defect emission intensity relative to the free-exciton E_{11} emission in the high-temperature range to extract the specific thermal trap depths of the distinct defects (see **Figure 5.10c** and **Table 5.1**).[19,196] On TiO_x, they were determined to be 100 and 36 meV for E_{11}* and E_{11}*$^-$ defects, respectively, while a thermal trap depth of 14 meV was extracted for the E_{11}* configuration on ZnO_x.

The obtained thermal trap depths are comparable to the wide range of previously reported thermal trap depths of oxygen defects[19,196] and are substantially smaller than the corresponding optical trap depths due to the defect site perturbation of both the excited and the ground state (see Section 2.3.1).[19] However, the absence of relative E_{11}*$^-$ intensity reduction on ZnO_x towards higher temperatures is unexpected. Likewise, the lower thermal trap depth of the E_{11}*$^-$ compared to the E_{11}* defect on TiO_x that stands in contrast to the observed higher E_{11}*$^-$ PL lifetime, and the dissimilar thermal trap depths of the presumably identical E_{11}* (ether-d) defect configurations on the different oxidic substrates (see **Table 5.1**) are unanticipated. If MPD is large compared to the rate of thermal detrapping, it may present a competing process in the

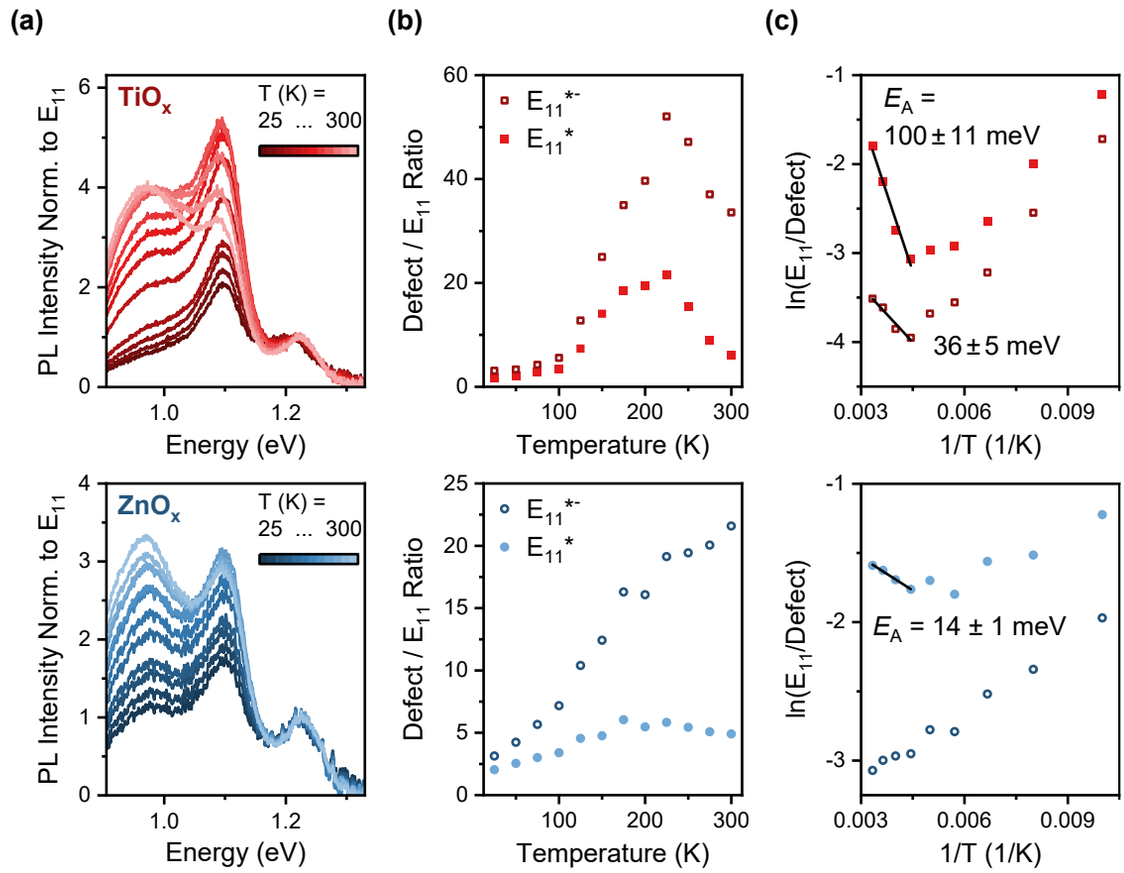

Figure 5.10: Temperature-dependent a) PL spectra of (6,5) SWCNTs normalized to the E_{11} intensity, b) integrated defect/E_{11} PL intensity ratios, and c) van't Hoff plots of E_{11}* and E_{11}*$^-$ defects in networks of (6,5) SWCNTs on TiO_x (top row) and ZnO_x (bottom row). Temperature steps of 25 K between 25 and 300 K.

temperature range investigated in this work and lead to a reduction of the relative defect PL intensity already at temperatures below the threshold for thermal detrapping. MPD is expected to become more relevant for the deeper E_{11}*$^-$ compared to the E_{11}* trap states due to the reduced energy difference between defect and ground state and resulting enhanced exciton-phonon coupling.[134] Thermal trap depths extracted from van't Hoff plots would accordingly be smaller than the actual thermal trap depths.[42] Differences in surface polarities of TiO_x and ZnO_x might also influence the MPD rates.[200] Furthermore, variations in defect density[196] and distribution, resulting in different defect-defect interactions, could potentially present another factor affecting the observed temperature-dependent PL behavior. A conclusive explanation of the highly complex temperature-dependent phenomena in functionalized SWCNTs remains however challenging to provide at the current state of knowledge.

5.6 Oxygen functionalization with spatial resolution

The functionalization strategy for SWCNT networks developed in this work might be further advanced by confining the UV irradiation to specific areas of the sample. This approach is especially interesting for nanotubes deposited on TiO_x, offering the potential for both spatially confined defect emission and PL brightening. To explore this prospect, (6,5) SWCNT networks on TiO_x were illuminated with UV light for 30 minutes in dry nitrogen through a metal shadow mask featuring multiple circular apertures of 60 µm diameter (see **Figure 5.11a**).

The PL map revealed a corresponding circular defect pattern, showing the expected increase in relative defect intensity in the UV-exposed areas (see **Figure 5.11b**). The contrast in total PL intensity appeared less pronounced, probably owing to inherent SWCNT network inhomogeneities and resulting variations in PL intensities (see **Figure 5.11c**). The Raman D/G^+ map revealed a distinct circular feature, 50 to 55 µm in diameter that indicated the anticipated increase in defect density (see **Figure 5.11d**). The observed patterns were slightly

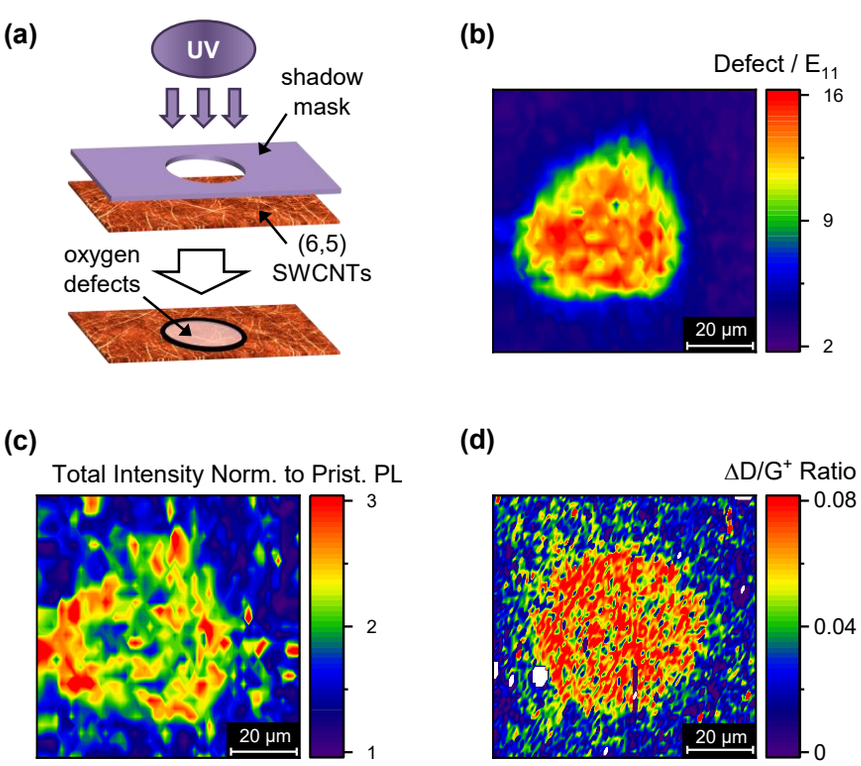

Figure 5.11: a) Schematic of the patterned introduction of oxygen defects into a (6,5) SWCNT network by UV exposure through a shadow mask in dry nitrogen atmosphere. b) Map of the combined defect intensity relative to E_{11} PL intensity and c) of the total normalized to the pristine PL intensity. d) Map of the Raman D/G^+ ratio with respect to non-exposed areas.

smaller than the mask aperture, likely due to shadowing effects arising from the non-zero thickness (60 μm) of the shadow mask. Discrepancies in pattern shapes between the PL and Raman maps may be attributed to mapping at different locations on the sample, having different shadowing effects. It seems feasible to achieve even smaller features, constrained solely by the irradiation wavelength (365 nm) and optics owing to the highly localized functionalization process. However, this would require an appropriate setup such as a mask aligner or direct laser-writer, operating under the dry nitrogen conditions essential for successful defect introduction.

5.7 Summary and conclusion

A solid-state approach to the functionalization of (6,5) SWCNT networks on photoactive substrates with two types of luminescent, red-shifted oxygen defects was presented in this chapter. The experimental constraints of the presented solid-state method are minimal, as it does not rely on solvents or additional reactants, and does not require tedious removal of reaction byproducts. Instead, the defect introduction is based on a photoreaction that creates reactive oxygen species in a dry nitrogen glovebox atmosphere, that is, in the presence of ppm levels of water and oxygen. Specifically, the ROS are formed from these trace amounts of water and oxygen through redox reaction at the surface of the UV-excited photoreactive transition metal oxide substrates TiO_x and ZnO_x. The ROS subsequently react with the SWCNTs, initiating the introduction of luminescent oxygen defects into the nanotube lattice. Similar reaction can be expected for other nanotube species, although with reactivities depending on the nanotube diameter.

The optical trap depths of the two observed types of luminescent oxygen defects are similar on TiO_x and ZnO_x and align well with the emission energies of previously reported ether-d (E_{11}^*) and epoxide-l (E_{11}^{*-}) defect configurations. However, PL brightening was observed only for the functionalized SWCNTs on TiO_x. Besides possible effects of different surface properties on the decay of the excited states, energy level differences in the reactive oxides might influence the preferential formation of certain ROS (hydroxy radicals *versus* superoxide radical anions). The distinct energetics and ROS reactivities could thus result in in the creation of different (luminescent or exciton-quenching) defect types, different defect type ratios or densities. This possibility could further be explored by investigation of the photoreaction on oxidic substrates with substantially different bandgaps, conduction and valence band energies, such as WO_3 or In_2O_3,[266] and through the deposition of already functionalized SWCNTs on

the oxidic surfaces. Moreover, single-nanotube spectroscopy and microscopy, investigating the spatial defect distribution as well as the distinct emission energies and intensities of individual defects on the different surfaces in the absence of screening by adjacent nanotubes, could further enhance the understanding of the defect formation.

Even though the exact origin of PL brightening on TiO_x as opposed to ZnO_x substrates remained elusive, the brightening effect was further utilized to create patterned emission from (6,5) SWCNT networks on TiO_x through spatially confined UV exposure in dry nitrogen. These patterns predominantly exhibited the red-shifted defect PL with brightened emission and good contrast. Notably, this strategy does not necessitate any additional processing steps like photoresist-based shielding of nanotube network areas from irradiation. While the presented patterns were tens of μm in lateral size, even finer features may be achieved using photolithography or direct laser-writing.

Finally, this chapter also demonstrated that care should be taken when photoactive layers are integrated into SWCNT-based optoelectronic systems. Unintended, extensive oxidative degradation of the nanotube lattice can occur during device processing and operation in the presence of atmospheric water and oxygen even on inert substrates like glass and BCB. This emphasizes the importance of establishing and maintaining precise conditions that ensure the desired device performance and stability.

6. Conclusion and outlook

This work investigated the controlled introduction and the photoluminescence properties of trions and defect-localized excitons in networks of (6,5) SWCNTs under different environmental conditions. Despite their different physical origins, both exhibit emission bands that are red-shifted with respect to the exciton and are highly sensitive towards changes in the local nanotube environment.

Chapter 4 systematically studied the dependence of the optical properties of trions and excitons in electrostatically charged (6,5) SWCNT networks on their dielectric environment. In contrast to the more commonly employed chemical doping techniques, electrostatic charging in the field-effect transistor geometry employed in this work enables the investigation of both positive and negative trions within the same environment. Here, the environment consisted of the glass substrate, neighboring polymer-wrapped nanotubes and the gate dielectric material as the variable component. Five different polymeric and oxidic materials, spanning a wide range of dielectric constants and functional groups, were used as the primary gate dielectrics in direct contact with the nanotube. While the uncharged excitonic emission was more dominated by the dielectric constant of the nanotube environment, the combined analysis of optical and electrical characteristics revealed the significant influence of environment-induced charge carrier trapping on the excited states upon FET charge accumulation. Hole-trapping environments led to weaker exciton quenching and blueshift, and lower trion/exciton ratios upon hole than upon electron accumulation. The opposite behavior was observed for environments with electron-trapping properties. This notion was further supported when electron traps were systematically removed with the reducing agent ttmgb. The observations were explained with an existing model that discriminates between homogeneous and inhomogeneous nanotube charging, which corresponds to trap-free and charge-trapping environments in this work. Future research should be devoted to the impact of the environment on trion electroluminescence, which is relevant for electrically driven devices. Trion electroluminescence was recently reported to become detectable from SWCNT networks in FETs through substrate surface passivation with thin films of highly apolar materials.[55] The reduced polar interactions substantially decrease undesired emission from red-shifted sidebands that impedes observation and analysis of weak trion features on glass substrates. Moreover, the introduction of reversibly photoswitchable charge trapping into the gate dielectric material using, *e.g.*, spiropyrans, might present a way to control trion emission

through both gate voltage and optical stimulation, the latter offering potential for spatial trion control.[267]

In **Chapter 5**, a new solid-state approach towards the controlled introduction of luminescent oxygen defects into networks of (6,5) SWCNTs, inspired by previous observations of oxidative SWCNT damaging under UV illumination, was presented and their emissive properties were investigated. Two different transition metal oxides were used as substrates for the nanotube networks and photoexcited with UV light to produce reactive oxygen species (ROS) in the presence of trace amounts of water and oxygen. The ROS reacted with the SWCNTs to initiate the formation of luminescent lattice defects. A dry-nitrogen glovebox atmosphere proved essential for the controlled defect introduction, since UV irradiation in the presence of abundant water and oxygen led to oxidative degradation of the nanotubes even on photocatalytically inert substrates like glass and BCB, which ultimately eliminated any photoluminescence. The method was also used to introduce defects with μm-spatial resolution, which is not feasible for SWCNTs functionalized in dispersion. Thus, this solid-state approach could help to introduce arrays of oxygen defects as single-photon emitters into nanotube networks. Irrespective of the photoreactive substrate material, the functionalization reaction yielded two types of defects with emission energies corresponding to previously reported ether-d (E_{11}^*) and epoxide-l (E_{11}^{*-}) configurations. Yet, PL brightening, their relative emission intensities, peak widths, PL decay and temperature dependence varied with the underlying metal oxide. Whether the observed variations originate from oxide-dependent variations in the defect introduction itself, *e.g.* due to their different electronic structures, or from distinct interactions of the metal oxides with the excited states, remained unclear. Yet, an enhanced understanding of the factors determining the reaction outcome might ultimately help to gain control over the selective occurrence of a certain defect configuration, and thus, spectral purity at a desired emission energy. Further insights into the reaction mechanism could be obtained by deposition of already oxygen-functionalized SWCNTs on the oxidic surfaces or by application of other photoreactive oxides. Single-nanotube spectroscopy and microscopy could reveal the precise distribution of the defects on each tube and provide details of the substrate-dependent emission energies and intensities of the single defects.

Both chapters explored emission features that are red-shifted compared to the free, mobile exciton. The trions investigated in Chapter 4 are induced reversibly, offering opportunities for gate-switchable emission characteristics, and possess non-zero spin and charge, which makes them interesting for spintronics.[39] In contrast to that, the covalent attachment of the luminescent oxygen defects to the nanotube lattice discussed in Chapter 5 creates permanent

changes. These zero-dimensional defects serve as promising candidates for single-photon emitters in optical quantum technologies, especially since the (6,5) SWCNT E_{11}^{*-} oxygen defect emits at energies within the telecommunication O-band (1260 – 1360 nm).[7] However, the essential enhancement of spectral purity and emission efficiency requires further investigations of configuration-selective defect introduction and the limitations to defect-induced PL brightening. Additionally, alignment of the emission from (6,5) SWCNTs with the more red-shifted telecommunication C-band (1530 – 1565 nm),[7] which is prevalent in optical signal processing compared to the O-band, is not possible. Thus, transfer of the presented concepts to larger-diameter tubes, which intrinsically emit further in the infrared, is necessary. Yet, it is important to note that increased tube diameters correlate with reduced strain and, consequently, a decrease in reactivity.[19,41,42] Furthermore, previous studies have indicated reduced defect-state PL quantum yields and lower trap depths in large-diameter nanotubes relative to smaller diameters.[20,47] This requires a compromise between brightness and red-shift, and, once again, highlights the importance of controlled introduction of distinct defect configurations.

Moreover, this thesis showcased the intricacies involved in manipulating the properties of SWCNTs for optoelectronic device applications, revealing a need to balance optical and electrical performance. Specifically, Chapter 4 demonstrated a trade-off where the suppression of trions led to reduced charge carrier mobilities, which is usually undesired. Chapter 5 illustrated how the introduction of luminescent defects on oxidic substrates enhanced photoluminescence, but charge carrier trapping and scattering on the highly polar substrates is anticipated to impede electrical charge transport.[166,175]

Achieving uniform emission across nanotube networks, which is also important for optoelectronic applications, was found to be complicated by the varied components of their local environment, such as substrates, adjacent nanotubes, and the gate dielectric layer in field-effect transistors. A multitude of interactions must therefore be accounted for in the spectroscopic and electrical analysis of carbon nanotube networks. Furthermore, bundled nanotubes are expected to be less susceptible to external influences than individual SWCNTs. This was thoroughly investigated in Chapter 4, where a reduced efficiency in charging was observed for bundled SWCNTs. Similar outcomes are expected for the nanotube density dependence of the oxygen functionalization reaction presented in Chapter 5, which should be validated through the corresponding experiments. Given all these considerations, reproducible optical spectroscopy of carbon nanotube networks necessitates specialized measurement

techniques that combine microscopic investigations with large-area averaging as employed here.

Overall, the controlled introduction and investigation of trions and luminescent oxygen defects presents opportunities for enhancing the optoelectronic properties of SWCNTs, particularly if the high sensitivity of SWCNTs to their environment and the presence of charge carriers is effectively managed. A better understanding of these interactions could not only enhance the applicability of SWCNTs in sensing applications, but is also necessary to mitigate adverse effects from unintended environmental alterations on the optoelectronic nanotube properties and to ensure reproducibility and comparability across different studies and labs.

Bibliography

(1) Heller, D. A.; Baik, S.; Eurell, T. E.; Strano, M. S. Single-Walled Carbon Nanotube Spectroscopy in Live Cells: Towards Long-Term Labels and Optical Sensors. *Adv. Mater.* **2005**, *17*, 2793–2799. DOI: 10.1002/adma.200500477.

(2) Miyata, Y.; Mizuno, K.; Kataura, H. Purity and Defect Characterization of Single-Wall Carbon Nanotubes Using Raman Spectroscopy. *J. Nanomater.* **2011**, *2011*, 1–7. DOI: 10.1155/2011/786763.

(3) Zaumseil, J. Single-walled carbon nanotube networks for flexible and printed electronics. *Semicond. Sci. Technol.* **2015**, *30*, 74001. DOI: 10.1088/0268-1242/30/7/074001.

(4) Zaumseil, J. Semiconducting Single-Walled Carbon Nanotubes or Very Rigid Conjugated Polymers: A Comparison. *Adv. Electron. Mater.* **2018**, *5*, 1800514. DOI: 10.1002/aelm.201800514.

(5) Li, C.; Wang, Q. Challenges and Opportunities for Intravital Near-Infrared Fluorescence Imaging Technology in the Second Transparency Window. *ACS Nano* **2018**, *12*, 9654–9659. DOI: 10.1021/acsnano.8b07536.

(6) Hong, G.; Antaris, A. L.; Dai, H. Near-infrared fluorophores for biomedical imaging. *Nat. Biomed. Eng.* **2017**, *1*, 1–22. DOI: 10.1038/s41551-016-0010.

(7) Senior, J. M. Optical fiber communications: Principles and practice, 3rd edition; Prentice Hall International series in optoelectronics; Prentice Hall, 2009. ISBN: 9780130326812.

(8) Iijima, S. Helical microtubules of graphitic carbon. *Nature* **1991**, *354*, 56. DOI: 10.1038/354056a0.

(9) Hertel, T.; Himmelein, S.; Ackermann, T.; Stich, D.; Crochet, J. Diffusion limited photoluminescence quantum yields in 1-D semiconductors: single-wall carbon nanotubes. *ACS Nano* **2010**, *4*, 7161–7168. DOI: 10.1021/nn101612b.

(10) Dresselhaus, M. S.; Dresselhaus, G.; Saito, R.; Jorio, A. Exciton photophysics of carbon nanotubes. *Annu. Rev. Phys. Chem.* **2007**, *58*, 719–747. DOI: 10.1146/annurev.physchem.58.032806.104628.

(11) Graf, A.; Zakharko, Y.; Schießl, S. P.; Backes, C.; Pfohl, M.; Flavel, B. S.; Zaumseil, J. Large scale, selective dispersion of long single-walled carbon nanotubes with high photoluminescence quantum yield by shear force mixing. *Carbon* **2016**, *105*, 593–599. DOI: 10.1016/j.carbon.2016.05.002.

(12) Qian, Q.; Li, G.; Jin, Y.; Liu, J.; Zou, Y.; Jiang, K.; Fan, S.; Li, Q. Trap-state-dominated suppression of electron conduction in carbon nanotube thin-film transistors. *ACS Nano* **2014**, *8*, 9597–9605. DOI: 10.1021/nn503903y.

(13) Zorn, N. F.; Settele, S.; Sebastian, F. L.; Lindenthal, S.; Zaumseil, J. Tuning Electroluminescence from Functionalized SWCNT Networks Further into the Near-Infrared. *ACS Appl. Opt. Mater.* **2023**, *1*, 1706–1714. DOI: 10.1021/acsaom.3c00261.

(14) Steiner, M.; Freitag, M.; Perebeinos, V.; Naumov, A.; Small, J. P.; Bol, A. A.; Avouris, P. Gate-variable light absorption and emission in a semiconducting carbon nanotube. *Nano Lett.* **2009**, *9*, 3477–3481. DOI: 10.1021/nl9016804.

(15) Larson, B. W.; Thurman, K. A.; Kang, H. S.; Ferguson, A. J.; Blackburn, J. L.; Steger, M. Arresting Photodegradation in Semiconducting Single-Walled Carbon Nanotube Thin Films. *ACS Appl. Nano Mater.* **2022**, *5*, 3502–3511. DOI: 10.1021/acsanm.1c04140.

(16) Graf, A.; Murawski, C.; Zakharko, Y.; Zaumseil, J.; Gather, M. C. Infrared Organic Light-Emitting Diodes with Carbon Nanotube Emitters. *Adv. Mater.* **2018**, *30*, 1706711. DOI: 10.1002/adma.201706711.

(17) Matsunaga, R.; Matsuda, K.; Kanemitsu, Y. Observation of charged excitons in hole-doped carbon nanotubes using photoluminescence and absorption spectroscopy. *Phys. Rev. Lett.* **2011**, *106*, 37404. DOI: 10.1103/PhysRevLett.106.037404.

(18) Santos, S. M.; Yuma, B.; Berciaud, S.; Shaver, J.; Gallart, M.; Gilliot, P.; Cognet, L.; Lounis, B. All-optical trion generation in single-walled carbon nanotubes. *Phys. Rev. Lett.* **2011**, *107*, 187401. DOI: 10.1103/PhysRevLett.107.187401.

(19) Ghosh, S.; Bachilo, S. M.; Simonette, R. A.; Beckingham, K. M.; Weisman, R. B. Oxygen doping modifies near-infrared band gaps in fluorescent single-walled carbon nanotubes. *Science* **2010**, *330*, 1656–1659. DOI: 10.1126/science.1196382.

(20) Piao, Y.; Meany, B.; Powell, L. R.; Valley, N.; Kwon, H.; Schatz, G. C.; Wang, Y. Brightening of carbon nanotube photoluminescence through the incorporation of sp^3 defects. *Nat. Chem.* **2013**, *5*, 840–845. DOI: 10.1038/nchem.1711.

(21) Rønnow, T. F.; Pedersen, T. G.; Cornean, H. D. Correlation and dimensional effects of trions in carbon nanotubes. *Phys. Rev. B* **2010**, *81*, 205446. DOI: 10.1103/PhysRevB.81.205446.

(22) Eckstein, K. H.; Oberndorfer, F.; Achsnich, M. M.; Schöppler, F.; Hertel, T. Quantifying Doping Levels in Carbon Nanotubes by Optical Spectroscopy. *J. Phys. Chem. C* **2019**, *123*, 30001–30006. DOI: 10.1021/acs.jpcc.9b08663.

(23) Park, J. S.; Hirana, Y.; Mouri, S.; Miyauchi, Y.; Nakashima, N.; Matsuda, K. Observation of negative and positive trions in the electrochemically carrier-doped single-walled carbon nanotubes. *J. Am. Chem. Soc.* **2012**, *134*, 14461–14466. DOI: 10.1021/ja304282j.

(24) Jakubka, F.; Grimm, S. B.; Zakharko, Y.; Gannott, F.; Zaumseil, J. Trion electroluminescence from semiconducting carbon nanotubes. *ACS Nano* **2014**, *8*, 8477–8486. DOI: 10.1021/nn503046y.

(25) Möhl, C.; Graf, A.; Berger, F. J.; Lüttgens, J.; Zakharko, Y.; Lumsargis, V.; Gather, M. C.; Zaumseil, J. Trion-Polariton Formation in Single-Walled Carbon Nanotube Microcavities. *ACS Photonics* **2018**, *5*, 2074–2080. DOI: 10.1021/acsphotonics.7b01549.

(26) Hartleb, H.; Späth, F.; Hertel, T. Evidence for Strong Electronic Correlations in the Spectra of Gate-Doped Single-Wall Carbon Nanotubes. *ACS Nano* **2015**, *9*, 10461–10470. DOI: 10.1021/acsnano.5b04707.

(27) Yoshida, M.; Popert, A.; Kato, Y. K. Gate-voltage induced trions in suspended carbon nanotubes. *Phys. Rev. B* **2016**, *93*, 41402. DOI: 10.1103/PhysRevB.93.041402.

(28) Zorn, N. F.; Scuratti, F.; Berger, F. J.; Perinot, A.; Heimfarth, D.; Caironi, M.; Zaumseil, J. Probing Mobile Charge Carriers in Semiconducting Carbon Nanotube Networks by Charge Modulation Spectroscopy. *ACS Nano* **2020**, *14*, 2412–2423. DOI: 10.1021/acsnano.9b09761.

(29) Gaulke, M.; Janissek, A.; Peyyety, N. A.; Alamgir, I.; Riaz, A.; Dehm, S.; Li, H.; Lemmer, U.; Flavel, B. S.; Kappes, M. M.; Hennrich, F.; Wei, L.; Chen, Y.; Pyatkov, F.; Krupke, R. Low-Temperature Electroluminescence Excitation Mapping of Excitons and Trions in Short-Channel Monochiral Carbon Nanotube Devices. *ACS Nano* **2020**, *14*, 2709–2717. DOI: 10.1021/acsnano.9b07207.

(30) Liang, S.; Ma, Z.; Wei, N.; Liu, H.; Wang, S.; Peng, L.-M. Solid state carbon nanotube device for controllable trion electroluminescence emission. *Nanoscale* **2016**, *8*, 6761–6769. DOI: 10.1039/C5NR07468A.

(31) Liang, S.; Wei, N.; Ma, Z.; Wang, F.; Liu, H.; Wang, S.; Peng, L.-M. Microcavity-Controlled Chirality-Sorted Carbon Nanotube Film Infrared Light Emitters. *ACS Photonics* **2017**, *4*, 435–442. DOI: 10.1021/acsphotonics.6b00856.

(32) Balcı Leinen, M.; Klein, P.; Sebastian, F. L.; Zorn, N. F.; Adamczyk, S.; Allard, S.; Scherf, U.; Zaumseil, J. Spiropyran-Functionalized Polymer–Carbon Nanotube Hybrids for Dynamic Optical Memory Devices and UV Sensors. *Adv. Electron. Mater.* **2020**, *6*, 2000717. DOI: 10.1002/aelm.202000717.

(33) Kuang, Z.; Berger, F. J.; Lustres, J. L. P.; Wollscheid, N.; Li, H.; Lüttgens, J.; Leinen, M. B.; Flavel, B. S.; Zaumseil, J.; Buckup, T. Charge Transfer from Photoexcited Semiconducting Single-Walled Carbon Nanotubes to Wide-Bandgap Wrapping Polymer. *J. Phys. Chem. C* **2021**, *125*, 8125–8136. DOI: 10.1021/acs.jpcc.0c10171.

(34) Kang, H. S.; Peurifoy, S.; Zhang, B.; Ferguson, A. J.; Reid, O. G.; Nuckolls, C.; Blackburn, J. L. Linking optical spectra to free charges in donor/acceptor heterojunctions: cross-correlation of transient microwave and optical spectroscopy. *Mater. Horiz.* **2021**, *8*, 1509–1517. DOI: 10.1039/D0MH01810D.

(35) Uda, T.; Tanaka, S.; Kato, Y. K. Molecular screening effects on exciton-carrier interactions in suspended carbon nanotubes. *Appl. Phys. Lett.* **2018**, *113*, 121105. DOI: 10.1063/1.5046433.

(36) Tanaka, S.; Otsuka, K.; Kimura, K.; Ishii, A.; Imada, H.; Kim, Y.; Kato, Y. K. Organic Molecular Tuning of Many-Body Interaction Energies in Air-Suspended Carbon Nanotubes. *J. Phys. Chem. C* **2019**, *123*, 5776–5781. DOI: 10.1021/acs.jpcc.8b12496.

(37) Galland, C.; Imamoğlu, A. All-optical manipulation of electron spins in carbon-nanotube quantum dots. *Phys. Rev. Lett.* **2008**, *101*, 157404. DOI: 10.1103/PhysRevLett.101.157404.

(38) Akizuki, N.; Iwamura, M.; Mouri, S.; Miyauchi, Y.; Kawasaki, T.; Watanabe, H.; Suemoto, T.; Watanabe, K.; Asano, K.; Matsuda, K. Nonlinear photoluminescence properties of trions in hole-doped single-walled carbon nanotubes. *Phys. Rev. B* **2014**, *89*, 195432. DOI: 10.1103/PhysRevB.89.195432.

(39) Bai, Y.; Olivier, J.-H.; Bullard, G.; Liu, C.; Therien, M. J. Dynamics of charged excitons in electronically and morphologically homogeneous single-walled carbon nanotubes. *PNAS* **2018**, *115*, 674–679. DOI: 10.1073/pnas.1712971115.

(40) Janas, D. Perfectly imperfect: a review of chemical tools for exciton engineering in single-walled carbon nanotubes. *Mater. Horiz.* **2020**, *7*, 2860–2881. DOI: 10.1039/D0MH00845A.

(41) Saha, A.; Gifford, B. J.; He, X.; Ao, G.; Zheng, M.; Kataura, H.; Htoon, H.; Kilina, S.; Tretiak, S.; Doorn, S. K. Narrow-band single-photon emission through selective aryl functionalization of zigzag carbon nanotubes. *Nat. Chem.* **2018**, *10*, 1089–1095. DOI: 10.1038/s41557-018-0126-4.

(42) Settele, S.; Berger, F. J.; Lindenthal, S.; Zhao, S.; El Yumin, A. A.; Zorn, N. F.; Asyuda, A.; Zharnikov, M.; Högele, A.; Zaumseil, J. Synthetic control over the binding configuration of luminescent sp^3-defects in single-walled carbon nanotubes. *Nat. Commun.* **2021**, *12*, 2119. DOI: 10.1038/s41467-021-22307-9.

(43) Yu, B.; Naka, S.; Aoki, H.; Kato, K.; Yamashita, D.; Fujii, S.; Kato, Y. K.; Fujigaya, T.; Shiraki, T. ortho-Substituted Aryldiazonium Design for the Defect Configuration-Controlled Photoluminescent Functionalization of Chiral Single-Walled Carbon Nanotubes. *ACS Nano* **2022**, *16*, 21452–21461. DOI: 10.1021/acsnano.2c09897.

(44) Wang, P.; Fortner, J.; Luo, H.; Kłos, J.; Wu, X.; Qu, H.; Chen, F.; Li, Y.; Wang, Y. Quantum Defects: What Pairs with the Aryl Group When Bonding to the sp^2 Carbon Lattice of Single-Wall Carbon Nanotubes? *J. Am. Chem. Soc.* **2022**, *144*, 13234–13241. DOI: 10.1021/jacs.2c03846.

(45) Iwamura, M.; Akizuki, N.; Miyauchi, Y.; Mouri, S.; Shaver, J.; Gao, Z.; Cognet, L.; Lounis, B.; Matsuda, K. Nonlinear photoluminescence spectroscopy of carbon nanotubes with localized exciton states. *ACS Nano* **2014**, *8*, 11254–11260. DOI: 10.1021/nn503803b.

(46) Ma, X.; Hartmann, N. F.; Baldwin, J. K. S.; Doorn, S. K.; Htoon, H. Room-temperature single-photon generation from solitary dopants of carbon nanotubes. *Nat. Nanotechnol.* **2015**, *10*, 671–675. DOI: 10.1038/nnano.2015.136.

(47) He, X.; Hartmann, N. F.; Ma, X.; Kim, Y.; Ihly, R.; Blackburn, J. L.; Gao, W.; Kono, J.; Yomogida, Y.; Hirano, A.; Tanaka, T.; Kataura, H.; Htoon, H.; Doorn, S. K. Tunable room-temperature single-photon emission at telecom wavelengths from sp^3 defects in carbon nanotubes. *Nat. Photonics* **2017**, *11*, 577–582. DOI: 10.1038/nphoton.2017.119.

(48) Luo, Y.; He, X.; Kim, Y.; Blackburn, J. L.; Doorn, S. K.; Htoon, H.; Strauf, S. Carbon Nanotube Color Centers in Plasmonic Nanocavities: A Path to Photon Indistinguishability at Telecom Bands. *Nano Lett.* **2019**, *19*, 9037–9044. DOI: 10.1021/acs.nanolett.9b04069.

(49) Brozena, A. H.; Kim, M.; Powell, L. R.; Wang, Y. Controlling the optical properties of carbon nanotubes with organic colour-centre quantum defects. *Nat Rev Chem* **2019**, *3*, 375–392. DOI: 10.1038/s41570-019-0103-5.

(50) Shiraki, T.; Miyauchi, Y.; Matsuda, K.; Nakashima, N. Carbon Nanotube Photoluminescence Modulation by Local Chemical and Supramolecular Chemical Functionalization. *Acc. Chem. Res.* **2020**, *53*, 1846–1859. DOI: 10.1021/acs.accounts.0c00294.

(51) Gifford, B. J.; Kilina, S.; Htoon, H.; Doorn, S. K.; Tretiak, S. Controlling Defect-State Photophysics in Covalently Functionalized Single-Walled Carbon Nanotubes. *Acc. Chem. Res.* **2020**, *53*, 1791–1801. DOI: 10.1021/acs.accounts.0c00210.

(52) Zaumseil, J. Luminescent Defects in Single-Walled Carbon Nanotubes for Applications. *Adv. Opt. Mater.* **2022**, *10*, 2101576. DOI: 10.1002/adom.202101576.

(53) Huang, Z.; Powell, L. R.; Wu, X.; Kim, M.; Qu, H.; Wang, P.; Fortner, J. L.; Xu, B.; Ng, A. L.; Wang, Y. Photolithographic Patterning of Organic Color-Centers. *Adv. Mater.* **2020**, *32*, 1906517. DOI: 10.1002/adma.201906517.

(54) Zorn, N. F.; Zaumseil, J. Charge transport in semiconducting carbon nanotube networks. *Appl. Phys. Rev.* **2021**, *8*, 41318. DOI: 10.1063/5.0065730.

(55) Zorn, N. F.; Settele, S.; Zhao, S.; Lindenthal, S.; El Yumin, A. A.; Wedl, T.; Li, H.; Flavel, B. S.; Högele, A.; Zaumseil, J. Near-Intrinsic Photo- and Electroluminescence from Single-Walled Carbon Nanotube Thin Films on BCB-Passivated Surfaces. *Adv. Opt. Mater.* **2023**, 2300236. DOI: 10.1002/adom.202300236.

(56) Rother, M.; Schießl, S. P.; Zakharko, Y.; Gannott, F.; Zaumseil, J. Understanding Charge Transport in Mixed Networks of Semiconducting Carbon Nanotubes. *ACS Appl. Mater. Interfaces* **2016**, *8*, 5571–5579. DOI: 10.1021/acsami.6b00074.

(57) Mehlenbacher, R. D.; McDonough, T. J.; Grechko, M.; Wu, M.-Y.; Arnold, M. S.; Zanni, M. T. Energy transfer pathways in semiconducting carbon nanotubes revealed using two-dimensional white-light spectroscopy. *Nat. Commun.* **2015**, *6*, 6732. DOI: 10.1038/ncomms7732.

(58) Tan, P. H.; Rozhin, A. G.; Hasan, T.; Hu, P.; Scardaci, V.; Milne, W. I.; Ferrari, A. C. Photoluminescence Spectroscopy of Carbon Nanotube Bundles: Evidence for Exciton Energy Transfer. *Phys. Rev. Lett.* **2007**, *99*, 137402. DOI: 10.1103/PhysRevLett.99.137402.

(59) Wong, H.-S. P.; Akinwande, D. Carbon Nanotube and Graphene Device Physics; Cambridge University Press, 2010. ISBN: 9780511778124.

(60) Fujisawa, K.; Kim, H. J.; Go, S. H.; Muramatsu, H.; Hayashi, T.; Endo, M.; Hirschmann, T. C.; Dresselhaus, M. S.; Kim, Y. A.; Araujo, P. T. A Review of Double-Walled and Triple-Walled Carbon Nanotube Synthesis and Applications. *Appl. Sci.* **2016**, *6*, 109. DOI: 10.3390/app6040109.

(61) Avouris, P.; Chen, Z.; Perebeinos, V. Carbon-based electronics. *Nat. Nanotechnol.* **2007**, *2*, 605–615. DOI: 10.1038/nnano.2007.300.

(62) Avouris, P.; Freitag, M.; Perebeinos, V. Carbon-nanotube photonics and optoelectronics. *Nat. Photonics* **2008**, *2*, 341. DOI: 10.1038/nphoton.2008.94.

(63) Kataura, H.; Kumazawa, Y.; Maniwa, Y.; Ohtsuka, Y.; Sen, R.; Suzuki, S.; Achiba, Y. Diameter control of single-walled carbon nanotubes. *Carbon* **2000**, *38*, 1691–1697. DOI: 10.1016/S0008-6223(00)00090-7.

(64) Prasek, J.; Drbohlavova, J.; Chomoucka, J.; Hubalek, J.; Jasek, O.; Adam, V.; Kizek, R. Methods for carbon nanotubes synthesis - review. *J. Mater. Chem.* **2011**, *21*, 15872. DOI: 10.1039/c1jm12254a.

(65) Kitiyanan, B.; Alvarez, W. E.; Harwell, J. H.; Resasco, D. E. Controlled production of single-wall carbon nanotubes by catalytic decomposition of CO on bimetallic Co–Mo catalysts. *Chem. Phys. Lett.* **2000**, *317*, 497–503. DOI: 10.1016/S0009-2614(99)01379-2.

(66) Kim, K. S.; Cota-Sanchez, G.; Kingston, C. T.; Imris, M.; Simard, B.; Soucy, G. Large-scale production of single-walled carbon nanotubes by induction thermal plasma. *J. Phys. D: Appl. Phys.* **2007**, *40*, 2375–2387. DOI: 10.1088/0022-3727/40/8/S17.

(67) Guo, T.; Nikolaev, P.; Thess, A.; Colbert, D. T.; Smalley, R. E. Catalytic growth of single-walled manotubes by laser vaporization. *Chem. Phys. Lett.* **1995**, *243*, 49–54. DOI: 10.1016/0009-2614(95)00825-O.

(68) Journet, C.; Maser, W. K.; Bernier, P.; Loiseau, A.; La Chapelle, M. L. de; Lefrant, S.; Deniard, P.; Lee, R.; Fischer, J. E. Large-scale production of single-walled carbon nanotubes by the electric-arc technique. *Nature* **1997**, *388*, 756–758. DOI: 10.1038/41972.

(69) Sanchez-Valencia, J. R.; Dienel, T.; Gröning, O.; Shorubalko, I.; Mueller, A.; Jansen, M.; Amsharov, K.; Ruffieux, P.; Fasel, R. Controlled synthesis of single-chirality carbon nanotubes. *Nature* **2014**, *512*, 61–64. DOI: 10.1038/nature13607.

(70) Coleman, J. N. Liquid-Phase Exfoliation of Nanotubes and Graphene. *Adv. Funct. Mater.* **2009**, *19*, 3680–3695. DOI: 10.1002/adfm.200901640.

(71) Bergin, S. D.; Nicolosi, V.; Streich, P. V.; Giordani, S.; Sun, Z.; Windle, A. H.; Ryan, P.; Niraj, N. P. P.; Wang, Z.-T. T.; Carpenter, L.; Blau, W. J.; Boland, J. J.; Hamilton, J. P.; Coleman, J. N. Towards Solutions of Single-Walled Carbon Nanotubes in Common Solvents. *Adv. Mater.* **2008**, *20*, 1876–1881. DOI: 10.1002/adma.200702451.

(72) Janas, D. Towards monochiral carbon nanotubes: a review of progress in the sorting of single-walled carbon nanotubes. *Mater. Chem. Front.* **2018**, *2*, 36–63. DOI: 10.1039/C7QM00427C.

(73) Hersam, M. C. Progress towards monodisperse single-walled carbon nanotubes. *Nat. Nanotechnol.* **2008**, *3*, 387–394. DOI: 10.1038/nnano.2008.135.

(74) Nish, A.; Hwang, J.-Y.; Doig, J.; Nicholas, R. J. Highly selective dispersion of single-walled carbon nanotubes using aromatic polymers. *Nat. Nanotechnol.* **2007**, *2*, 640–646. DOI: 10.1038/nnano.2007.290.

(75) Samanta, S. K.; Fritsch, M.; Scherf, U.; Gomulya, W.; Bisri, S. Z.; Loi, M. A. Conjugated polymer-assisted dispersion of single-wall carbon nanotubes: the power of polymer wrapping. *Acc. Chem. Res.* **2014**, *47*, 2446–2456. DOI: 10.1021/ar500141j.

(76) Gao, J.; Loi, M. A.; Carvalho, E. J. F. de; Dos Santos, M. C. Selective wrapping and supramolecular structures of polyfluorene-carbon nanotube hybrids. *ACS Nano* **2011**, *5*, 3993–3999. DOI: 10.1021/nn200564n.

(77) Gomulya, W.; Costanzo, G. D.; Carvalho, E. J. F. de; Bisri, S. Z.; Derenskyi, V.; Fritsch, M.; Fröhlich, N.; Allard, S.; Gordiichuk, P.; Herrmann, A.; Marrink, S. J.; Dos Santos, M. C.; Scherf, U.; Loi, M. A. Semiconducting single-walled carbon nanotubes on demand by polymer wrapping. *Adv. Mater.* **2013**, *25*, 2948–2956. DOI: 10.1002/adma.201300267.

(78) Ozawa, H.; Ide, N.; Fujigaya, T.; Niidome, Y.; Nakashima, N. One-pot Separation of Highly Enriched (6,5)-Single-walled Carbon Nanotubes Using a Fluorene-based Copolymer. *Chem. Lett.* **2011**, *40*, 239–241. DOI: 10.1246/cl.2011.239.

(79) Lee, H. W.; Yoon, Y.; Park, S.; Oh, J. H.; Hong, S.; Liyanage, L. S.; Wang, H.; Morishita, S.; Patil, N.; Park, Y. J.; Park, J. J.; Spakowitz, A.; Galli, G.; Gygi, F.; Wong, P. H.-S.; Tok, J. B.-H.; Kim, J. M.; Bao, Z. Selective dispersion of high purity semiconducting single-walled carbon nanotubes with regioregular poly(3-alkylthiophene)s. *Nat. Commun.* **2011**, *2*, 541. DOI: 10.1038/ncomms1545.

(80) Lemasson, F. A.; Strunk, T.; Gerstel, P.; Hennrich, F.; Lebedkin, S.; Barner-Kowollik, C.; Wenzel, W.; Kappes, M. M.; Mayor, M. Selective dispersion of single-walled carbon nanotubes with specific chiral indices by poly(*N*-decyl-2,7-carbazole). *J. Am. Chem. Soc.* **2011**, *133*, 652–655. DOI: 10.1021/ja105722u.

(81) Schiessl, S. P.; Fröhlich, N.; Held, M.; Gannott, F.; Schweiger, M.; Forster, M.; Scherf, U.; Zaumseil, J. Polymer-sorted semiconducting carbon nanotube networks for high-performance ambipolar field-effect transistors. *ACS Appl. Mater. Interfaces* **2015**, *7*, 682–689. DOI: 10.1021/am506971b.

(82) Jakubka, F.; Schießl, S. P.; Martin, S.; Englert, J. M.; Hauke, F.; Hirsch, A.; Zaumseil, J. Effect of Polymer Molecular Weight and Solution Parameters on Selective Dispersion of Single-Walled Carbon Nanotubes. *ACS Macro Lett.* **2012**, *1*, 815–819. DOI: 10.1021/mz300147g.

(83) Hwang, J.-Y.; Nish, A.; Doig, J.; Douven, S.; Chen, C.-W.; Chen, L.-C.; Nicholas, R. J. Polymer structure and solvent effects on the selective dispersion of single-walled carbon nanotubes. *J. Am. Chem. Soc.* **2008**, *130*, 3543–3553. DOI: 10.1021/ja0777640.

(84) Ding, J.; Li, Z.; Lefebvre, J.; Du, X.; Malenfant, P. R. L. Mechanistic Consideration of pH Effect on the Enrichment of Semiconducting SWCNTs by Conjugated Polymer Extraction. *J. Phys. Chem. C* **2016**, *120*, 21946–21954. DOI: 10.1021/acs.jpcc.6b05965.

(85) Naumov, A. V.; Tsyboulski, D. A.; Bachilo, S. M.; Weisman, R. B. Length-dependent optical properties of single-walled carbon nanotube samples. *Chem. Phys.* **2013**, *422*, 255–263. DOI: 10.1016/j.chemphys.2012.12.033.

(86) Reich, S.; Maultzsch, J.; Thomsen, C.; Ordejón, P. Tight-binding description of graphene. *Phys. Rev. B* **2002**, *66*, 2794. DOI: 10.1103/PhysRevB.66.035412.

(87) Charlier, J.-C.; Blase, X.; Roche, S. Electronic and transport properties of nanotubes. *Rev. Mod. Phys.* **2007**, *79*, 677. DOI: 10.1103/RevModPhys.79.677.

(88) Saito, R.; Dresselhaus, G.; Dresselhaus, M. S. Trigonal warping effect of carbon nanotubes. *Phys. Rev. B* **2000**, *61*, 2981–2990. DOI: 10.1103/PhysRevB.61.2981.

(89) Kleiner, A.; Eggert, S. Curvature, hybridization, and STM images of carbon nanotubes. *Phys. Rev. B* **2001**, *64*. DOI: 10.1103/PhysRevB.64.113402.

(90) Wilder, J. W. G.; Venema, L. C.; Rinzler, A. G.; Smalley, R. E.; Dekker, C. Electronic structure of atomically resolved carbon nanotubes. *Nature* **1998**, *391*, 59–62. DOI: 10.1038/34139.

(91) Schießl, S. P.; Vries, X. de; Rother, M.; Massé, A.; Brohmann, M.; Bobbert, P. A.; Zaumseil, J. Modeling carrier density dependent charge transport in semiconducting carbon nanotube networks. *Phys. Rev. Mater.* **2017**, *1*, 46003. DOI: 10.1103/PhysRevMaterials.1.046003.

(92) Statz, M.; Schneider, S.; Berger, F. J.; Lai, L.; Wood, W. A.; Abdi-Jalebi, M.; Leingang, S.; Himmel, H.-J.; Zaumseil, J.; Sirringhaus, H. Charge and Thermoelectric Transport in Polymer-Sorted Semiconducting Single-Walled Carbon Nanotube Networks. *ACS Nano* **2020**, *14*, 15552–15565. DOI: 10.1021/acsnano.0c06181.

(93) Weisman, R. B.; Bachilo, S. M. Dependence of Optical Transition Energies on Structure for Single-Walled Carbon Nanotubes in Aqueous Suspension: An Empirical Kataura Plot. *Nano Lett.* **2003**, *3*, 1235–1238. DOI: 10.1021/nl034428i.

(94) Amori, A. R.; Hou, Z.; Krauss, T. D. Excitons in Single-Walled Carbon Nanotubes and Their Dynamics. *Annu. Rev. Condens. Matter Phys.* **2018**, *69*, 81–99. DOI: 10.1146/annurev-physchem-050317-014241.

(95) Blancon, J.-C.; Paillet, M.; Tran, H. N.; Than, X. T.; Guebrou, S. A.; Ayari, A.; San Miguel, A.; Phan, N.-M.; Zahab, A.-A.; Sauvajol, J.-L.; Del Fatti, N.; Vallée, F. Direct measurement of the absolute absorption spectrum of individual semiconducting single-wall carbon nanotubes. *Nat. Commun.* **2013**, *4*, 2542. DOI: 10.1038/ncomms3542.

(96) O'Connell, M. J.; Bachilo, S. M.; Huffman, C. B.; Moore, V. C.; Strano, M. S.; Haroz, E. H.; Rialon, K. L.; Boul, P. J.; Noon, W. H.; Kittrell, C.; Ma, J.; Hauge, R. H.; Weisman, R. B.; Smalley, R. E. Band Gap Fluorescence from Individual Single-Walled Carbon Nanotubes. *Science* **2002**, *297*, 593–596. DOI: 10.1126/science.1072631.

(97) Kane, C. L.; Mele, E. J. Ratio problem in single carbon nanotube fluorescence spectroscopy. *Phys. Rev. Lett.* **2003**, *90*, 207401. DOI: 10.1103/PhysRevLett.90.207401.

(98) Spataru, C. D.; Ismail-Beigi, S.; Benedict, L. X.; Louie, S. G. Excitonic Effects and Optical Spectra of Single-Walled Carbon Nanotubes. *Phys. Rev. Lett.* **2004**, *92*, 77402. DOI: 10.1103/PhysRevLett.92.077402.

(99) Wang, F.; Dukovic, G.; Brus, L. E.; Heinz, T. F. The Optical Resonances in Carbon Nanotubes Arise from Excitons. *Science* **2005**, *308*, 838–841. DOI: 10.1126/science.1110265.

(100) Maultzsch, J.; Pomraenke, R.; Reich, S.; Chang, E.; Prezzi, D.; Ruini, A.; Molinari, E.; Strano, M. S.; Thomsen, C.; Lienau, C. Exciton binding energies in carbon nanotubes from two-photon photoluminescence. *Phys. Rev. B* **2005**, *72*, 241402. DOI: 10.1103/PhysRevB.72.241402.

(101) Miyauchi, Y. Photoluminescence studies on exciton photophysics in carbon nanotubes. *J. Mater. Chem. C* **2013**, *1*, 6499–6521. DOI: 10.1039/C3TC00947E.

(102) Perebeinos, V.; Tersoff, J.; Avouris, P. Radiative lifetime of excitons in carbon nanotubes. *Nano Lett.* **2005**, *5*, 2495–2499. DOI: 10.1021/nl051828s.

(103) Mortimer, I. B.; Nicholas, R. J. Role of bright and dark excitons in the temperature-dependent photoluminescence of carbon nanotubes. *Phys. Rev. Lett.* **2007**, *98*, 27404. DOI: 10.1103/PhysRevLett.98.027404.

(104) Blackburn, J. L.; Holt, J. M.; Irurzun, V. M.; Resasco, D. E.; Rumbles, G. Confirmation of K-momentum dark exciton vibronic sidebands using ^{13}C-labeled, highly enriched (6,5) single-walled carbon nanotubes. *Nano Lett.* **2012**, *12*, 1398–1403. DOI: 10.1021/nl204072x.

(105) Capaz, R. B.; Spataru, C. D.; Ismail-Beigi, S.; Louie, S. G. Excitons in carbon nanotubes: Diameter and chirality trends. *Phys. Status Solidi B* **2007**, *244*, 4016–4020. DOI: 10.1002/pssb.200776200.

(106) Palotás, J.; Negyedi, M.; Kollarics, S.; Bojtor, A.; Rohringer, P.; Pichler, T.; Simon, F. Incidence of Quantum Confinement on Dark Triplet Excitons in Carbon Nanotubes. *ACS Nano* **2020**, *14*, 11254–11261. DOI: 10.1021/acsnano.0c03139.

(107) Soavi, G.; Scotognella, F.; Lanzani, G.; Cerullo, G. Ultrafast Photophysics of Single-Walled Carbon Nanotubes. *Adv. Opt. Mater.* **2016**, *4*, 1670–1688. DOI: 10.1002/adom.201600361.

(108) Harrah, D. M.; Schneck, J. R.; Green, A. A.; Hersam, M. C.; Ziegler, L. D.; Swan, A. K. Intensity-dependent exciton dynamics of (6,5) single-walled carbon nanotubes: momentum selection rules, diffusion, and nonlinear interactions. *ACS Nano* **2011**, *5*, 9898–9906. DOI: 10.1021/nn203604v.

(109) Jones, M.; Engtrakul, C.; Metzger, W. K.; Ellingson, R. J.; Nozik, A. J.; Heben, M. J.; Rumbles, G. Analysis of photoluminescence from solubilized single-walled carbon nanotubes. *Phys. Rev. B* **2005**, *71*, 115426. DOI: 10.1103/PhysRevB.71.115426.

(110) Amori, A. R.; Rossi, J. E.; Landi, B. J.; Krauss, T. D. Defects Enable Dark Exciton Photoluminescence in Single-Walled Carbon Nanotubes. *J. Phys. Chem. C* **2018**, *122*, 3599–3607. DOI: 10.1021/acs.jpcc.7b10565.

(111) Tumiel, T. M.; Amin, M.; Krauss, T. D. Single-Walled Carbon Nanotube Dark Exciton Photoluminescence Dynamics. *J. Phys. Chem. C* **2021**, *125*, 25022–25029. DOI: 10.1021/acs.jpcc.1c05818.

(112) Kadria-Vili, Y.; Bachilo, S. M.; Blackburn, J. L.; Weisman, R. B. Photoluminescence Side Band Spectroscopy of Individual Single-Walled Carbon Nanotubes. *J. Phys. Chem. C* **2016**, *120*, 23898–23904. DOI: 10.1021/acs.jpcc.6b08768.

(113) Lüttgens, J. M.; Berger, F. J.; Zaumseil, J. Population of Exciton-Polaritons via Luminescent sp^3 Defects in Single-Walled Carbon Nanotubes. *ACS Photonics* **2021**, *8*, 182–193. DOI: 10.1021/acsphotonics.0c01129.

(114) Cognet, L.; Tsyboulski, D. A.; Rocha, J.-D. R.; Doyle, C. D.; Tour, J. M.; Weisman, R. B. Stepwise quenching of exciton fluorescence in carbon nanotubes by single-molecule reactions. *Science* **2007**, *316*, 1465–1468. DOI: 10.1126/science.1141316.

(115) Crochet, J. J.; Duque, J. G.; Werner, J. H.; Lounis, B.; Cognet, L.; Doorn, S. K. Disorder limited exciton transport in colloidal single-wall carbon nanotubes. *Nano Lett.* **2012**, *12*, 5091–5096. DOI: 10.1021/nl301739d.

(116) Harrah, D. M.; Swan, A. K. The role of length and defects on optical quantum efficiency and exciton decay dynamics in single-walled carbon nanotubes. *ACS Nano* **2011**, *5*, 647–655. DOI: 10.1021/nn1031214.

(117) Berger, S.; Iglesias, F.; Bonnet, P.; Voisin, C.; Cassabois, G.; Lauret, J.-S.; Delalande, C.; Roussignol, P. Optical properties of carbon nanotubes in a composite material: The role of dielectric screening and thermal expansion. *J. Appl. Phys.* **2009**, *105*, 94323. DOI: 10.1063/1.3116723.

(118) Ando, T. Environment Effects on Excitons in Semiconducting Carbon Nanotubes. *J. Phys. Soc. Jpn.* **2010**, *79*, 24706. DOI: 10.1143/JPSJ.79.024706.

(119) Dyatlova, O. A.; Gomis-Bresco, J.; Malic, E.; Telg, H.; Maultzsch, J.; Zhong, G.; Geng, J.; Woggon, U. Dielectric screening effects on transition energies in aligned carbon nanotubes. *Phys. Rev. B* **2012**, *85*, 245449. DOI: 10.1103/PhysRevB.85.245449.

(120) Perebeinos, V.; Tersoff, J.; Avouris, P. Scaling of excitons in carbon nanotubes. *Phys. Rev. Lett.* **2004**, *92*, 257402. DOI: 10.1103/PhysRevLett.92.257402.

(121) Miyauchi, Y.; Saito, R.; Sato, K.; Ohno, Y.; Iwasaki, S.; Mizutani, T.; Jiang, J.; Maruyama, S. Dependence of exciton transition energy of single-walled carbon nanotubes on surrounding dielectric materials. *Chem. Phys. Lett.* **2007**, *442*, 394–399. DOI: 10.1016/j.cplett.2007.06.018.

(122) Walsh, A. G.; Vamivakas, A. N.; Yin, Y.; Cronin, S. B.; Unlü, M. S.; Goldberg, B. B.; Swan, A. K. Screening of excitons in single, suspended carbon nanotubes. *Nano Lett.* **2007**, *7*, 1485–1488. DOI: 10.1021/nl070193p.

(123) Silvera-Batista, C. A.; Wang, R. K.; Weinberg, P.; Ziegler, K. J. Solvatochromic shifts of single-walled carbon nanotubes in nonpolar microenvironments. *Phys. Chem. Chem. Phys.* **2010**, *12*, 6990–6998. DOI: 10.1039/b927053a.

(124) Machiya, H.; Uda, T.; Ishii, A.; Kato, Y. K. Spectral tuning of optical coupling between air-mode nanobeam cavities and individual carbon nanotubes. *Appl. Phys. Lett.* **2018**, *112*, 21101. DOI: 10.1063/1.5008299.

(125) Raynaud, C.; Claude, T.; Borel, A.; Amara, M. R.; Graf, A.; Zaumseil, J.; Lauret, J.-S.; Chassagneux, Y.; Voisin, C. Superlocalization of Excitons in Carbon Nanotubes at Cryogenic Temperature. *Nano Lett.* **2019**, *19*, 7210–7216. DOI: 10.1021/acs.nanolett.9b02816.

(126) Otsuka, K.; Fang, N.; Yamashita, D.; Taniguchi, T.; Watanabe, K.; Kato, Y. K. Deterministic transfer of optical-quality carbon nanotubes for atomically defined technology. *Nat. Commun.* **2021**, *12*, 3138. DOI: 10.1038/s41467-021-23413-4.

(127) Sarpkaya, I.; Zhang, Z.; Walden-Newman, W.; Wang, X.; Hone, J.; Wong, C. W.; Strauf, S. Prolonged spontaneous emission and dephasing of localized excitons in air-bridged carbon nanotubes. *Nat. Commun.* **2013**, *4*, 2152. DOI: 10.1038/ncomms3152.

(128) Schweiger, M.; Zakharko, Y.; Gannott, F.; Grimm, S. B.; Zaumseil, J. Photoluminescence enhancement of aligned arrays of single-walled carbon nanotubes by polymer transfer. *Nanoscale* **2015**, *7*, 16715–16720. DOI: 10.1039/c5nr05163k.

(129) Larsen, B. A.; Deria, P.; Holt, J. M.; Stanton, I. N.; Heben, M. J.; Therien, M. J.; Blackburn, J. L. Effect of solvent polarity and electrophilicity on quantum yields and

solvatochromic shifts of single-walled carbon nanotube photoluminescence. *J. Am. Chem. Soc.* **2012**, *134*, 12485–12491. DOI: 10.1021/ja2114618.

(130) Lefebvre, J.; Homma, Y.; Finnie, P. Bright band gap photoluminescence from unprocessed single-walled carbon nanotubes. *Phys. Rev. Lett.* **2003**, *90*, 217401. DOI: 10.1103/PhysRevLett.90.217401.

(131) Campo, J.; Cambré, S.; Botka, B.; Obrzut, J.; Wenseleers, W.; Fagan, J. A. Optical Property Tuning of Single-Wall Carbon Nanotubes by Endohedral Encapsulation of a Wide Variety of Dielectric Molecules. *ACS Nano* **2021**, *15*, 2301–2317. DOI: 10.1021/acsnano.0c08352.

(132) MacLeod, B. A.; Stanton, N. J.; Gould, I. E.; Wesenberg, D.; Ihly, R.; Owczarczyk, Z. R.; Hurst, K. E.; Fewox, C. S.; Folmar, C. N.; Holman Hughes, K.; Zink, B. L.; Blackburn, J. L.; Ferguson, A. J. Large *n*- and *p*-type thermoelectric power factors from doped semiconducting single-walled carbon nanotube thin films. *Energy Environ. Sci.* **2017**, *10*, 2168–2179. DOI: 10.1039/C7EE01130J.

(133) Kinder, J. M.; Mele, E. J. Nonradiative recombination of excitons in carbon nanotubes mediated by free charge carriers. *Phys. Rev. B* **2008**, *78*, 155429. DOI: 10.1103/PhysRevB.78.155429.

(134) Perebeinos, V.; Avouris, P. Phonon and electronic nonradiative decay mechanisms of excitons in carbon nanotubes. *Phys. Rev. Lett.* **2008**, *101*, 57401. DOI: 10.1103/PhysRevLett.101.057401.

(135) Eckstein, K. H.; Kunkel, P.; Voelckel, M.; Schöppler, F.; Hertel, T. Trions, Exciton Dynamics, and Spectral Modifications in Doped Carbon Nanotubes: A Singular Defect-Driven Mechanism. *J. Phys. Chem. C* **2023**, *127*, 19659–19667. DOI: 10.1021/acs.jpcc.3c04889.

(136) Spataru, C. D.; Léonard, F. Tunable band gaps and excitons in doped semiconducting carbon nanotubes made possible by acoustic plasmons. *Phys. Rev. Lett.* **2010**, *104*, 177402. DOI: 10.1103/PhysRevLett.104.177402.

(137) Spataru, C. D.; Léonard, F. Quasiparticle and exciton renormalization effects in electrostatically doped semiconducting carbon nanotubes. *Chem. Phys.* **2013**, *413*, 81–88. DOI: 10.1016/j.chemphys.2012.08.021.

(138) Yasukochi, S.; Murai, T.; Moritsubo, S.; Shimada, T.; Chiashi, S.; Maruyama, S.; Kato, Y. K. Gate-induced blueshift and quenching of photoluminescence in suspended single-walled carbon nanotubes. *Phys. Rev. B* **2011**, *84*, 121409. DOI: 10.1103/PhysRevB.84.121409.

(139) Mouri, S.; Miyauchi, Y.; Iwamura, M.; Matsuda, K. Temperature dependence of photoluminescence spectra in hole-doped single-walled carbon nanotubes: Implications of trion localization. *Phys. Rev. B* **2013**, *87*, 45408. DOI: 10.1103/PhysRevB.87.045408.

(140) Li, M.-K.; Riaz, A.; Wederhake, M.; Fink, K.; Saha, A.; Dehm, S.; He, X.; Schöppler, F.; Kappes, M. M.; Htoon, H.; Popov, V. N.; Doorn, S. K.; Hertel, T.; Hennrich, F.; Krupke, R. Electroluminescence from Single-Walled Carbon Nanotubes with Quantum Defects. *ACS Nano* **2022**, *16*, 11742–11754. DOI: 10.1021/acsnano.2c03083.

(141) Eckstein, K. H.; Hartleb, H.; Achsnich, M. M.; Schöppler, F.; Hertel, T. Localized Charges Control Exciton Energetics and Energy Dissipation in Doped Carbon Nanotubes. *ACS Nano* **2017**, *11*, 10401–10408. DOI: 10.1021/acsnano.7b05543.

(142) Eckstein, K. H.; Hertel, T. Electronic Structure and Scaling of Coulomb Defects in Carbon Nanotubes from Modified Hückel Calculations. *J. Phys. Chem. C* **2023**, *127*, 23760–23767. DOI: 10.1021/acs.jpcc.3c06007.

(143) Gotthardt, J. M.; Schneider, S.; Brohmann, M.; Leingang, S.; Sauter, E.; Zharnikov, M.; Himmel, H.-J.; Zaumseil, J. Molecular *n*-Doping of Large- and Small-Diameter Carbon Nanotube Field-Effect Transistors with Tetrakis(tetramethylguanidino)benzene. *ACS Appl. Electron. Mater.* **2021**, *3*, 804–812. DOI: 10.1021/acsaelm.0c00957.

(144) Misewich, J. A.; Martel, R.; Avouris, P.; Tsang, J. C.; Heinze, S.; Tersoff, J. Electrically Induced Optical Emission from a Carbon Nanotube FET. *Science* **2003**, *300*, 783–786. DOI: 10.1126/science.1081294.

(145) Jakubka, F.; Backes, C.; Gannott, F.; Mundloch, U.; Hauke, F.; Hirsch, A.; Zaumseil, J. Mapping charge transport by electroluminescence in chirality-selected carbon nanotube networks. *ACS Nano* **2013**, *7*, 7428–7435. DOI: 10.1021/nn403419d.

(146) Javey, A.; Guo, J.; Wang, Q.; Lundstrom, M.; Dai, H. Ballistic carbon nanotube field-effect transistors. *Nature* **2003**, *424*, 654. DOI: 10.1038/nature01797.

(147) Zhou, X.; Park, J.-Y.; Huang, S.; Liu, J.; McEuen, P. L. Band Structure, Phonon Scattering, and the Performance Limit of Single-Walled Carbon Nanotube Transistors. *Phys. Rev. Lett.* **2005**, *95*, 146805. DOI: 10.1103/PhysRevLett.95.146805.

(148) Perebeinos, V.; Tersoff, J.; Avouris, P. Electron-Phonon Interaction and Transport in Semiconducting Carbon Nanotubes. *Phys. Rev. Lett.* **2005**, *94*, 86802. DOI: 10.1103/PhysRevLett.94.086802.

(149) Zhao, Y.; Candebat, D.; Delker, C.; Zi, Y.; Janes, D.; Appenzeller, J.; Yang, C. Understanding the impact of Schottky barriers on the performance of narrow bandgap

nanowire field effect transistors. *Nano Lett.* **2012**, *12*, 5331–5336. DOI: 10.1021/nl302684s.

(150) Ilani, S.; Donev, L. A. K.; Kindermann, M.; McEuen, P. L. Measurement of the quantum capacitance of interacting electrons in carbon nanotubes. *Nat. Phys.* **2006**, *2*, 687–691. DOI: 10.1038/nphys412.

(151) Shimotani, H.; Tsuda, S.; Yuan, H.; Yomogida, Y.; Moriya, R.; Takenobu, T.; Yanagi, K.; Iwasa, Y. Continuous Band-Filling Control and One-Dimensional Transport in Metallic and Semiconducting Carbon Nanotube Tangled Films. *Adv. Funct. Mater.* **2014**, *24*, 3305–3311. DOI: 10.1002/adfm.201303566.

(152) Perebeinos, V.; Tersoff, J.; Avouris, P. Mobility in semiconducting carbon nanotubes at finite carrier density. *Nano Lett.* **2006**, *6*, 205–208. DOI: 10.1021/nl052044h.

(153) Schießl, S. P.; Rother, M.; Lüttgens, J.; Zaumseil, J. Extracting the field-effect mobilities of random semiconducting single-walled carbon nanotube networks: A critical comparison of methods. *Appl. Phys. Lett.* **2017**, *111*, 193301. DOI: 10.1063/1.5006877.

(154) Cao, Q.; Xia, M.; Kocabas, C.; Shim, M.; Rogers, J. A.; Rotkin, S. V. Gate capacitance coupling of singled-walled carbon nanotube thin-film transistors. *Appl. Phys. Lett.* **2007**, *90*, 23516. DOI: 10.1063/1.2431465.

(155) Rosenblatt, S.; Yaish, Y.; Park, J.; Gore, J.; Sazonova, V.; McEuen, P. L. High Performance Electrolyte Gated Carbon Nanotube Transistors. *Nano Lett.* **2002**, *2*, 869–872. DOI: 10.1021/nl025639a.

(156) Behnam, A.; Guo, J.; Ural, A. Effects of nanotube alignment and measurement direction on percolation resistivity in single-walled carbon nanotube films. *J. Appl. Phys.* **2007**, *102*, 44313. DOI: 10.1063/1.2769953.

(157) Islam, A. E.; Rogers, J. A.; Alam, M. A. Recent Progress in Obtaining Semiconducting Single-Walled Carbon Nanotubes for Transistor Applications. *Adv. Mater.* **2015**, *27*, 7908–7937. DOI: 10.1002/adma.201502918.

(158) Malhofer, A.; Rother, M.; Zakharko, Y.; Graf, A.; Schießl, S. P.; Zaumseil, J. Direct visualization of percolation paths in carbon nanotube/polymer composites. *Org. Electron.* **2017**, *45*, 151–158. DOI: 10.1016/j.orgel.2017.03.010.

(159) Fuhrer, M. S.; Nygård, J.; Shih, L.; Forero, M.; Yoon, Y.-G.; Mazzoni, M. S. C.; Choi, H. J.; Ihm, J.; Louie, S. G.; Zettl, A.; McEuen, P. L. Crossed Nanotube Junctions. *Science* **2000**, *288*, 494–497. DOI: 10.1126/science.288.5465.494.

(160) Nirmalraj, P. N.; Lyons, P. E.; De, S.; Coleman, J. N.; Boland, J. J. Electrical connectivity in single-walled carbon nanotube networks. *Nano Lett.* **2009**, *9*, 3890–3895. DOI: 10.1021/nl9020914.

(161) Znidarsic, A.; Kaskela, A.; Laiho, P.; Gaberscek, M.; Ohno, Y.; Nasibulin, A. G.; Kauppinen, E. I.; Hassanien, A. Spatially Resolved Transport Properties of Pristine and Doped Single-Walled Carbon Nanotube Networks. *J. Phys. Chem. C* **2013**, *117*, 13324–13330. DOI: 10.1021/jp403983y.

(162) Brohmann, M.; Rother, M.; Schießl, S. P.; Preis, E.; Allard, S.; Scherf, U.; Zaumseil, J. Temperature-Dependent Charge Transport in Polymer-Sorted Semiconducting Carbon Nanotube Networks with Different Diameter Distributions. *J. Phys. Chem. C* **2018**, *122*, 19886–19896. DOI: 10.1021/acs.jpcc.8b04302.

(163) Brohmann, M.; Berger, F. J.; Matthiesen, M.; Schießl, S. P.; Schneider, S.; Zaumseil, J. Charge Transport in Mixed Semiconducting Carbon Nanotube Networks with Tailored Mixing Ratios. *ACS Nano* **2019**, *13*, 7323–7332. DOI: 10.1021/acsnano.9b03699.

(164) Zorn, N. F.; Berger, F. J.; Zaumseil, J. Charge Transport in and Electroluminescence from sp^3-Functionalized Carbon Nanotube Networks. *ACS Nano* **2021**, *15*, 10451–10463. DOI: 10.1021/acsnano.1c02878.

(165) Zheng, W.; Zorn, N. F.; Bonn, M.; Zaumseil, J.; Wang, H. I. Probing Carrier Dynamics in sp^3-Functionalized Single-Walled Carbon Nanotubes with Time-Resolved Terahertz Spectroscopy. *ACS Nano* **2022**, *16*, 9401–9409. DOI: 10.1021/acsnano.2c02199.

(166) Lee, S.-H.; Xu, Y.; Khim, D.; Park, W.-T.; Kim, D.-Y.; Noh, Y.-Y. Effect of Polymer Gate Dielectrics on Charge Transport in Carbon Nanotube Network Transistors: Low-k Insulator for Favorable Active Interface. *ACS Appl. Mater. Interfaces* **2016**, *8*, 32421–32431. DOI: 10.1021/acsami.6b06882.

(167) Dash, A.; Scheunemann, D.; Kemerink, M. Comprehensive Model for the Thermoelectric Properties of Two-Dimensional Carbon Nanotube Networks. *Phys. Rev. Applied* **2022**, *18*, 64022. DOI: 10.1103/PhysRevApplied.18.064022.

(168) Tripathy, S.; Bose, B.; Chakrabarti, P. P.; Bhattacharyya, T. K. Resistive Analysis of Scattering-Dependent Electrical Transport in Single-Wall Carbon-Nanotube Networks. *J. Appl. Phys.* **2020**, *67*, 5676–5684. DOI: 10.1109/TED.2020.3029734.

(169) Gao, J.; Loo, Y.-L. L. Temperature-Dependent Electrical Transport in Polymer-Sorted Semiconducting Carbon Nanotube Networks. *Adv. Funct. Mater.* **2015**, *25*, 105–110. DOI: 10.1002/adfm.201402407.

(170) Sano, E.; Tanaka, T. A simple drain current model for single-walled carbon nanotube network thin-film transistors. *J. Appl. Phys.* **2014**, *115*, 154507. DOI: 10.1063/1.4871775.

(171) Li, Z.; Ouyang, J.; Ding, J. Diameter-Dependent Semiconducting Carbon Nanotube Network Transistor Performance. *ACS Appl. Electron. Mater.* **2022**, *4*, 6335–6344. DOI: 10.1021/acsaelm.2c01469.

(172) Scuratti, F.; Salazar-Rios, J. M.; Luzio, A.; Kowalski, S.; Allard, S.; Jung, S.; Scherf, U.; Loi, M. A.; Caironi, M. Charge Transport in High-Mobility Field-Effect Transistors Based on Inkjet Printed Random Networks of Polymer Wrapped Single-Walled Carbon Nanotubes. *Adv. Funct. Mater.* **2021**, *31*, 2006895. DOI: 10.1002/adfm.202006895.

(173) Chortos, A.; Pochorovski, I.; Lin, P.; Pitner, G.; Yan, X.; Gao, T. Z.; To, J. W. F.; Lei, T.; Will, J. W.; Wong, H.-S. P.; Bao, Z. Universal Selective Dispersion of Semiconducting Carbon Nanotubes from Commercial Sources Using a Supramolecular Polymer. *ACS Nano* **2017**, *11*, 5660–5669. DOI: 10.1021/acsnano.7b01076.

(174) Mirka, B.; Rice, N. A.; Williams, P.; Tousignant, M. N.; Boileau, N. T.; Bodnaryk, W. J.; Fong, D.; Adronov, A.; Lessard, B. H. Excess Polymer in Single-Walled Carbon Nanotube Thin-Film Transistors: Its Removal Prior to Fabrication Is Unnecessary. *ACS Nano* **2021**, *15*, 8252–8266. DOI: 10.1021/acsnano.0c08584.

(175) Perebeinos, V.; Rotkin, S. V.; Petrov, A. G.; Avouris, P. The effects of substrate phonon mode scattering on transport in carbon nanotubes. *Nano Lett.* **2009**, *9*, 312–316. DOI: 10.1021/nl8030086.

(176) Veres, J.; Ogier, S. D.; Leeming, S. W.; Cupertino, D. C.; Khaffaf, S. M. Low-k Insulators as the Choice of Dielectrics in Organic Field-Effect Transistors. *Adv. Funct. Mater.* **2003**, *13*, 199–204. DOI: 10.1002/adfm.200390030.

(177) Held, M.; Schießl, S. P.; Miehler, D.; Gannott, F.; Zaumseil, J. Polymer/metal oxide hybrid dielectrics for low voltage field-effect transistors with solution-processed, high-mobility semiconductors. *Appl. Phys. Lett.* **2015**, *107*, 83301. DOI: 10.1063/1.4929461.

(178) Rønnow, T. F.; Pedersen, T. G.; Cornean, H. D. Stability of singlet and triplet trions in carbon nanotubes. *Phys. Lett. A* **2009**, *373*, 1478–1481. DOI: 10.1016/j.physleta.2009.02.049.

(179) Brozena, A. H.; Leeds, J. D.; Zhang, Y.; Fourkas, J. T.; Wang, Y. Controlled defects in semiconducting carbon nanotubes promote efficient generation and luminescence of trions. *ACS Nano* **2014**, *8*, 4239–4247. DOI: 10.1021/nn500894p.

(180) Kwon, H.; Kim, M.; Nutz, M.; Hartmann, N. F.; Perrin, V.; Meany, B.; Hofmann, M. S.; Clark, C. W.; Htoon, H.; Doorn, S. K.; Högele, A.; Wang, Y. Probing Trions at Chemically Tailored Trapping Defects. *ACS Cent. Sci.* **2019**, *5*, 1786–1794. DOI: 10.1021/acscentsci.9b00707.

(181) Xu, B.; Wu, X.; Kim, M.; Wang, P.; Wang, Y. Electroluminescence from 4-nitroaryl organic color centers in semiconducting single-wall carbon nanotubes. *J. Appl. Phys.* **2021**, *129*, 44305. DOI: 10.1063/5.0039047.

(182) Yuma, B.; Berciaud, S.; Besbas, J.; Shaver, J.; Santos, S.; Ghosh, S.; Weisman, R. B.; Cognet, L.; Gallart, M.; Ziegler, M.; Hönerlage, B.; Lounis, B.; Gilliot, P. Biexciton, single carrier, and trion generation dynamics in single-walled carbon nanotubes. *Phys. Rev. B* **2013**, *87*, 205412. DOI: 10.1103/PhysRevB.87.205412.

(183) Nishihara, T.; Yamada, Y.; Kanemitsu, Y. Dynamics of exciton-hole recombination in hole-doped single-walled carbon nanotubes. *Phys. Rev. B* **2012**, *86*, 75449. DOI: 10.1103/PhysRevB.86.075449.

(184) Nishihara, T.; Yamada, Y.; Okano, M.; Kanemitsu, Y. Trion formation and recombination dynamics in hole-doped single-walled carbon nanotubes. *Appl. Phys. Lett.* **2013**, *103*, 23101. DOI: 10.1063/1.4813014.

(185) Koyama, T.; Shimizu, S.; Miyata, Y.; Shinohara, H.; Nakamura, A. Ultrafast formation and decay dynamics of trions in *p*-doped single-walled carbon nanotubes. *Phys. Rev. B* **2013**, *87*, 165430. DOI: 10.1103/PhysRevB.87.165430.

(186) Nishihara, T.; Okano, M.; Yamada, Y.; Kanemitsu, Y. Review – Photophysics of Trions in Single-Walled Carbon Nanotubes. *ECS J. Solid State Sci. Technol.* **2017**, *6*, M3062-M3064. DOI: 10.1149/2.0091706jss.

(187) Nishihara, T.; Yamada, Y.; Okano, M.; Kanemitsu, Y. Dynamics of the Lowest-Energy Excitons in Single-Walled Carbon Nanotubes under Resonant and Nonresonant Optical Excitation. *J. Phys. Chem. C* **2015**, *119*, 28654–28659. DOI: 10.1021/acs.jpcc.5b09485.

(188) El Yumin, A. A.; Zorn, N. F.; Berger, F. J.; Heimfarth, D.; Zaumseil, J. Trion emission from frozen *p-n* junctions in networks of electrolyte-gated (6,5) single-walled carbon nanotubes. *Carbon* **2023**, *202*, 547–553. DOI: 10.1016/j.carbon.2022.11.025.

(189) Watanabe, K.; Asano, K. Trions in semiconducting single-walled carbon nanotubes. *Phys. Rev. B* **2012**, *85*, 35416. DOI: 10.1103/PhysRevB.85.035416.

(190) Eremin, T. V.; Obraztsov, P. A.; Velikanov, V. A.; Shubina, T. V.; Obraztsova, E. D. Many-particle excitations in non-covalently doped single-walled carbon nanotubes. *Sci. Rep.* **2019**, *9*, 14985. DOI: 10.1038/s41598-019-50333-7.

(191) Miyauchi, Y.; Ajiki, H.; Maruyama, S. Electron-hole asymmetry in single-walled carbon nanotubes probed by direct observation of transverse quasidark excitons. *Phys. Rev. B* **2010**, *81*, 121415. DOI: 10.1103/PhysRevB.81.121415.

(192) Matsunaga, R.; Matsuda, K.; Kanemitsu, Y. Origin of low-energy photoluminescence peaks in single carbon nanotubes: K-momentum dark excitons and triplet dark excitons. *Phys. Rev. B* **2010**, *81*, 33401. DOI: 10.1103/PhysRevB.81.033401.

(193) Kilina, S.; Ramirez, J.; Tretiak, S. Brightening of the lowest exciton in carbon nanotubes via chemical functionalization. *Nano Lett.* **2012**, *12*, 2306–2312. DOI: 10.1021/nl300165w.

(194) Sykes, M. E.; Kim, M.; Wu, X.; Wiederrecht, G. P.; Peng, L.; Wang, Y.; Gosztola, D. J.; Ma, X. Ultrafast exciton trapping at sp^3 quantum defects in carbon nanotubes. *ACS Nano* **2019**, *13*, 13264–13270. DOI: 10.1021/acsnano.9b06279.

(195) Ma, X.; Adamska, L.; Yamaguchi, H.; Yalcin, S. E.; Tretiak, S.; Doorn, S. K.; Htoon, H. Electronic structure and chemical nature of oxygen dopant states in carbon nanotubes. *ACS Nano* **2014**, *8*, 10782–10789. DOI: 10.1021/nn504553y.

(196) Kim, M.; Adamska, L.; Hartmann, N. F.; Kwon, H.; Liu, J.; Velizhanin, K. A.; Piao, Y.; Powell, L. R.; Meany, B.; Doorn, S. K.; Tretiak, S.; Wang, Y. Fluorescent carbon nanotube defects manifest substantial vibrational reorganization. *J. Phys. Chem. C* **2016**, *120*, 11268–11276. DOI: 10.1021/acs.jpcc.6b02538.

(197) Berger, F. J.; Lüttgens, J.; Nowack, T.; Kutsch, T.; Lindenthal, S.; Kistner, L.; Müller, C. C.; Bongartz, L. M.; Lumsargis, V. A.; Zakharko, Y.; Zaumseil, J. Brightening of long, polymer-wrapped carbon nanotubes by sp^3 functionalization in organic solvents. *ACS Nano* **2019**, *13*, 9259–9269. DOI: 10.1021/acsnano.9b03792.

(198) Hartmann, N. F.; Velizhanin, K. A.; Haroz, E. H.; Kim, M.; Ma, X.; Wang, Y.; Htoon, H.; Doorn, S. K. Photoluminescence Dynamics of Aryl sp^3 Defect States in Single-Walled Carbon Nanotubes. *ACS Nano* **2016**, *10*, 8355–8365. DOI: 10.1021/acsnano.6b02986.

(199) Kim, Y.; Velizhanin, K. A.; He, X.; Sarpkaya, I.; Yomogida, Y.; Tanaka, T.; Kataura, H.; Doorn, S. K.; Htoon, H. Photoluminescence Intensity Fluctuations and Temperature-Dependent Decay Dynamics of Individual Carbon Nanotube sp^3 Defects. *J. Phys. Chem. Lett.* **2019**, *10*, 1423–1430. DOI: 10.1021/acs.jpclett.8b03732.

(200) He, X.; Velizhanin, K. A.; Bullard, G.; Bai, Y.; Olivier, J.-H.; Hartmann, N. F.; Gifford, B. J.; Kilina, S.; Tretiak, S.; Htoon, H.; Therien, M. J.; Doorn, S. K. Solvent- and Wavelength-Dependent Photoluminescence Relaxation Dynamics of Carbon

Nanotube sp^3 Defect States. *ACS Nano* **2018**, *12*, 8060–8070. DOI: 10.1021/acsnano.8b02909.

(201) Miyauchi, Y.; Iwamura, M.; Mouri, S.; Kawazoe, T.; Ohtsu, M.; Matsuda, K. Brightening of excitons in carbon nanotubes on dimensionality modification. *Nat. Photonics* **2013**, *7*, 715–719. DOI: 10.1038/nphoton.2013.179.

(202) Kozawa, D.; Wu, X.; Ishii, A.; Fortner, J.; Otsuka, K.; Xiang, R.; Inoue, T.; Maruyama, S.; Wang, Y.; Kato, Y. K. Formation of organic color centers in air-suspended carbon nanotubes using vapor-phase reaction. *Nat. Commun.* **2022**, *13*, 2814. DOI: 10.1038/s41467-022-30508-z.

(203) Danné, N.; Kim, M.; Godin, A. G.; Kwon, H.; Gao, Z.; Wu, X.; Hartmann, N. F.; Doorn, S. K.; Lounis, B.; Wang, Y.; Cognet, L. Ultrashort Carbon Nanotubes That Fluoresce Brightly in the Near-Infrared. *ACS Nano* **2018**, *12*, 6059–6065. DOI: 10.1021/acsnano.8b02307.

(204) Eremin, T.; Eremina, V.; Svirko, Y.; Obraztsov, P. Over Two-Fold Photoluminescence Enhancement from Single-Walled Carbon Nanotubes Induced by Oxygen Doping. *Nanomater.* **2023**, *13*, 1561. DOI: 10.3390/nano13091561.

(205) Lin, C.-W.; Bachilo, S. M.; Zheng, Y.; Tsedev, U.; Huang, S.; Weisman, R. B.; Belcher, A. M. Creating fluorescent quantum defects in carbon nanotubes using hypochlorite and light. *Nat. Commun.* **2019**, *10*, 2874. DOI: 10.1038/s41467-019-10917-3.

(206) He, X.; Sun, L.; Gifford, B. J.; Tretiak, S.; Piryatinski, A.; Li, X.; Htoon, H.; Doorn, S. K. Intrinsic limits of defect-state photoluminescence dynamics in functionalized carbon nanotubes. *Nanoscale* **2019**, *11*, 9125–9132. DOI: 10.1039/c9nr02175b.

(207) Sebastian, F. L.; Zorn, N. F.; Settele, S.; Lindenthal, S.; Berger, F. J.; Bendel, C.; Li, H.; Flavel, B. S.; Zaumseil, J. Absolute Quantification of sp^3 Defects in Semiconducting Single-Wall Carbon Nanotubes by Raman Spectroscopy. *J. Phys. Chem. Lett.* **2022**, *13*, 3542–3548. DOI: 10.1021/acs.jpclett.2c00758.

(208) Ma, X.; Baldwin, J. K. S.; Hartmann, N. F.; Doorn, S. K.; Htoon, H. Solid-State Approach for Fabrication of Photostable, Oxygen-Doped Carbon Nanotubes. *Adv. Funct. Mater.* **2015**, *25*, 6157–6164. DOI: 10.1002/adfm.201502580.

(209) Maeda, Y.; Zhao, P.; Ehara, M. Recent progress in controlling the photoluminescence properties of single-walled carbon nanotubes by oxidation and alkylation. *Chem. Commun.* **2023**, *59*, 14497–14508. DOI: 10.1039/d3cc05065c.

(210) Chiu, C. F.; Saidi, W. A.; Kagan, V. E.; Star, A. Defect-Induced Near-Infrared Photoluminescence of Single-Walled Carbon Nanotubes Treated with Polyunsaturated Fatty Acids. *J. Am. Chem. Soc.* **2017**, *139*, 4859–4865. DOI: 10.1021/jacs.7b00390.

(211) Maeda, Y.; Konno, Y.; Nishino, A.; Yamada, M.; Okudaira, S.; Miyauchi, Y.; Matsuda, K.; Matsui, J.; Mitsuishi, M.; Suzuki, M. Sonochemical reaction to control the near-infrared photoluminescence properties of single-walled carbon nanotubes. *Nanoscale* **2020**, *12*, 6263–6270. DOI: 10.1039/d0nr00271b.

(212) Shiraishi, T.; Juhász, G.; Shiraki, T.; Akizuki, N.; Miyauchi, Y.; Matsuda, K.; Nakashima, N. Determination of Precise Redox Properties of Oxygen-Doped Single-Walled Carbon Nanotubes Based on in Situ Photoluminescence Electrochemistry. *J. Phys. Chem. C* **2016**, *120*, 15632–15639. DOI: 10.1021/acs.jpcc.5b07841.

(213) Iizumi, Y.; Yudasaka, M.; Kim, J.; Sakakita, H.; Takeuchi, T.; Okazaki, T. Oxygen-doped carbon nanotubes for near-infrared fluorescent labels and imaging probes. *Sci. Rep.* **2018**, *8*, 6272. DOI: 10.1038/s41598-018-24399-8.

(214) Maeda, Y.; Higo, J.; Amagai, Y.; Matsui, J.; Ohkubo, K.; Yoshigoe, Y.; Hashimoto, M.; Eguchi, K.; Yamada, M.; Hasegawa, T.; Sato, Y.; Zhou, J.; Lu, J.; Miyashita, T.; Fukuzumi, S.; Murakami, T.; Tohji, K.; Nagase, S.; Akasaka, T. Helicity-selective photoreaction of single-walled carbon nanotubes with organosulfur compounds in the presence of oxygen. *J. Am. Chem. Soc.* **2013**, *135*, 6356–6362. DOI: 10.1021/ja402199n.

(215) Xhyliu, F.; Ao, G. Surface Coating- and Light-Controlled Oxygen Doping of Carbon Nanotubes. *J. Phys. Chem. C* **2021**, *125*, 9236–9243. DOI: 10.1021/acs.jpcc.1c00257.

(216) Zaumseil, J.; Sirringhaus, H. Electron and ambipolar transport in organic field-effect transistors. *Chem. Rev.* **2007**, *107*, 1296–1323. DOI: 10.1021/cr0501543.

(217) Kang, M. S.; Frisbie, C. D. A pedagogical perspective on ambipolar FETs. *ChemPhysChem* **2013**, *14*, 1547–1552. DOI: 10.1002/cphc.201300014.

(218) Klauk, H. Organic thin-film transistors. *Chem. Soc. Rev.* **2010**, *39*, 2643–2666. DOI: 10.1039/b909902f.

(219) Salleo, A. Charge transport in polymeric transistors. *Mater. Today* **2007**, *10*, 38–45. DOI: 10.1016/S1369-7021(07)70018-4.

(220) Chua, L.-L.; Ho, P. K. H.; Sirringhaus, H.; Friend, R. H. High-stability ultrathin spin-on benzocyclobutene gate dielectric for polymer field-effect transistors. *Appl. Phys. Lett.* **2004**, *84*, 3400–3402. DOI: 10.1063/1.1710716.

(221) Geoghegan, M.; Hadziioannou, G. Polymer Electronics; OUP Oxford, 2013. ISBN: 9780199533824.

(222) Kalb, W. L.; Batlogg, B. Calculating the trap density of states in organic field-effect transistors from experiment: A comparison of different methods. *Phys. Rev. B* **2010**, *81*, 35327. DOI: 10.1103/PhysRevB.81.035327.

(223) Klauk, H. Will We See Gigahertz Organic Transistors? *Adv. Electron. Mater.* **2018**, *4*, 1700474. DOI: 10.1002/aelm.201700474.

(224) Choi, H. H.; Cho, K.; Frisbie, C. D.; Sirringhaus, H.; Podzorov, V. Critical assessment of charge mobility extraction in FETs. *Nat. Mater.* **2017**, *17*, 2–7. DOI: 10.1038/nmat5035.

(225) Pesavento, P. V.; Puntambekar, K. P.; Frisbie, C. D.; McKeen, J. C.; Ruden, P. P. Film and contact resistance in pentacene thin-film transistors: Dependence on film thickness, electrode geometry, and correlation with hole mobility. *J. Appl. Phys.* **2006**, *99*, 94504. DOI: 10.1063/1.2197033.

(226) Choi, H. H.; Rodionov, Y. I.; Paterson, A. F.; Panidi, J.; Saranin, D.; Kharlamov, N.; Didenko, S. I.; Anthopoulos, T. D.; Cho, K.; Podzorov, V. Accurate Extraction of Charge Carrier Mobility in 4-Probe Field-Effect Transistors. *Adv. Funct. Mater.* **2018**, *28*, 1707105. DOI: 10.1002/adfm.201707105.

(227) Ding, J.; Li, Z.; Lefebvre, J.; Cheng, F.; Dubey, G.; Zou, S.; Finnie, P.; Hrdina, A.; Scoles, L.; Lopinski, G. P.; Kingston, C. T.; Simard, B.; Malenfant, P. R. L. Enrichment of large-diameter semiconducting SWCNTs by polyfluorene extraction for high network density thin film transistors. *Nanoscale* **2014**, *6*, 2328–2339. DOI: 10.1039/c3nr05511f.

(228) Schneider, S.; Brohmann, M.; Lorenz, R.; Hofstetter, Y. J.; Rother, M.; Sauter, E.; Zharnikov, M.; Vaynzof, Y.; Himmel, H.-J.; Zaumseil, J. Efficient *n*-Doping and Hole Blocking in Single-Walled Carbon Nanotube Transistors with 1,2,4,5-Tetrakis(tetramethylguanidino)benzene. *ACS Nano* **2018**, *12*, 5895–5902. DOI: 10.1021/acsnano.8b02061.

(229) Dresselhaus, M. S.; Jorio, A.; Hofmann, M.; Dresselhaus, G.; Saito, R. Perspectives on carbon nanotubes and graphene Raman spectroscopy. *Nano Lett.* **2010**, *10*, 751–758. DOI: 10.1021/nl904286r.

(230) Dresselhaus, M. S.; Jorio, A.; Souza Filho, A. G.; Saito, R. Defect characterization in graphene and carbon nanotubes using Raman spectroscopy. *Philos. Trans. R. Soc. A* **2010**, *368*, 5355–5377. DOI: 10.1098/rsta.2010.0213.

(231) Mooney, J.; Kambhampati, P. Get the Basics Right: Jacobian Conversion of Wavelength and Energy Scales for Quantitative Analysis of Emission Spectra. *J. Phys. Chem. Lett.* **2013**, *4*, 3316–3318. DOI: 10.1021/JZ401508T.

(232) Wieland, S.; El Yumin, A. A.; Gotthardt, J. M.; Zaumseil, J. Impact of Dielectric Environment on Trion Emission from Single-Walled Carbon Nanotube Networks. *J. Phys. Chem. C* **2023**, *127*, 3112–3122. DOI: 10.1021/acs.jpcc.2c08338.

(233) Freitag, M.; Steiner, M.; Naumov, A.; Small, J. P.; Bol, A. A.; Perebeinos, V.; Avouris, P. Carbon Nanotube Photo- and Electroluminescence in Longitudinal Electric Fields. *ACS Nano* **2009**, *3*, 3744–3748. DOI: 10.1021/nn900962f.

(234) Hulea, I. N.; Fratini, S.; Xie, H.; Mulder, C. L.; Iossad, N. N.; Rastelli, G.; Ciuchi, S.; Morpurgo, A. F. Tunable Fröhlich polarons in organic single-crystal transistors. *Nat. Mater.* **2006**, *5*, 982–986. DOI: 10.1038/nmat1774.

(235) Sirringhaus, H. Device Physics of Solution-Processed Organic Field-Effect Transistors. *Adv. Mater.* **2005**, *17*, 2411–2425. DOI: 10.1002/adma.200501152.

(236) Horowitz, G. Organic Transistors. In *Organic Electronics*; Klauk, H., Ed.; Wiley, 2006; pp 1–32. DOI: 10.1002/3527608753.ch1.

(237) Shea, M. J.; Mehlenbacher, R. D.; Zanni, M. T.; Arnold, M. S. Experimental Measurement of the Binding Configuration and Coverage of Chirality-Sorting Polyfluorenes on Carbon Nanotubes. *J. Phys. Chem. Lett.* **2014**, *5*, 3742–3749. DOI: 10.1021/jz5017813.

(238) Liu, L.; Han, J.; Xu, L.; Zhou, J.; Zhao, C.; Ding, S.; Shi, H.; Xiao, M.; Ding, L.; Ma, Z.; Jin, C.; Zhang, Z.; Peng, L.-M. Aligned, high-density semiconducting carbon nanotube arrays for high-performance electronics. *Science* **2020**, *368*, 850–856. DOI: 10.1126/science.aba5980.

(239) Paterson, A. F.; Mottram, A. D.; Faber, H.; Niazi, M. R.; Fei, Z.; Heeney, M.; Anthopoulos, T. D. Impact of the Gate Dielectric on Contact Resistance in High-Mobility Organic Transistors. *Adv. Electron. Mater.* **2019**, *5*, 1800723. DOI: 10.1002/aelm.201800723.

(240) Nketia-Yawson, B.; Noh, Y.-Y. Recent Progress on High-Capacitance Polymer Gate Dielectrics for Flexible Low-Voltage Transistors. *Adv. Funct. Mater.* **2018**, *28*, 1802201. DOI: 10.1002/adfm.201802201.

(241) Weiwei Xu; Zhen Liu; Jianwen Zhao; Wenya Xu; Weibing Gu; Xiang Zhang; Long Qian; Zheng Cui. Flexible logic circuits based on top-gate thin film transistors with printed semiconductor carbon nanotubes and top electrodes. *Nanoscale* **2014**, *6*, 14891–14897. DOI: 10.1039/C4NR05471G.

(242) Kim, S.; Suzuki, K.; Sugie, A.; Yoshida, H.; Yoshida, M.; Suzuki, Y. Effect of end group of amorphous perfluoro-polymer electrets on electron trapping. *Sci. Technol. Adv. Mater.* **2018**, *19*, 486–494. DOI: 10.1080/14686996.2018.1477395.

(243) Hirschberg, R. E.; Scharnberg, M.; Schröder, S.; Rehders, S.; Strunskus, T.; Faupel, F. Electret films with extremely high charge stability prepared by thermal evaporation of Teflon AF. *Org. Electron.* **2018**, *57*, 146–150. DOI: 10.1016/j.orgel.2018.02.040.

(244) Lau, C.; Srimani, T.; Bishop, M. D.; Hills, G.; Shulaker, M. M. Tunable *n*-Type Doping of Carbon Nanotubes through Engineered Atomic Layer Deposition HfOX Films. *ACS Nano* **2018**, *12*, 10924–10931. DOI: 10.1021/acsnano.8b04208.

(245) Tomohiro Shiraki; Yoshiaki Niidome; Fumiyuki Toshimitsu; Tomonari Shiraishi; Tamehito Shiga; Boda Yu; Tsuyohiko Fujigaya. Solvatochromism of near infrared photoluminescence from doped sites of locally functionalized single-walled carbon nanotubes. *Chem. Commun.* **2019**, *55*, 3662–3665. DOI: 10.1039/C9CC00829B.

(246) Kimoto, Y.; Okano, M.; Kanemitsu, Y. Observation of excited-state excitons and band-gap renormalization in hole-doped carbon nanotubes using photoluminescence excitation spectroscopy. *Phys. Rev. B* **2013**, *87*, 195416. DOI: 10.1103/PhysRevB.87.195416.

(247) Eckstein, K. H.; Hirsch, F.; Martel, R.; Hertel, T. Infrared Study of Charge Carrier Confinement in Doped (6,5) Carbon Nanotubes. *J. Phys. Chem. C* **2021**, *125*, 5700–5707. DOI: 10.1021/acs.jpcc.1c00123.

(248) Wieland, S.; El Yumin, A. A.; Settele, S.; Zaumseil, J. Photo-Activated, Solid-State Introduction of Luminescent Oxygen Defects into Semiconducting Single-Walled Carbon Nanotubes. *J. Phys. Chem. C* **2024**, *128*, 2012–2021. DOI: 10.1021/acs.jpcc.3c07000.

(249) Nosaka, Y.; Nosaka, A. Y. Generation and Detection of Reactive Oxygen Species in Photocatalysis. *Chem. Rev.* **2017**, *117*, 11302–11336. DOI: 10.1021/acs.chemrev.7b00161.

(250) Samadi, M.; Zirak, M.; Naseri, A.; Khorashadizade, E.; Moshfegh, A. Z. Recent progress on doped ZnO nanostructures for visible-light photocatalysis. *Thin Solid Films* **2016**, *605*, 2–19. DOI: 10.1016/j.tsf.2015.12.064.

(251) Mattila, H.; Khorobrykh, S.; Havurinne, V.; Tyystjärvi, E. Reactive oxygen species: Reactions and detection from photosynthetic tissues. *J. Photochem. Photobiol. B* **2015**, *152*, 176–214. DOI: 10.1016/j.jphotobiol.2015.10.001.

(252) Hsieh, H.-S.; Zepp, R. G. Reactivity of graphene oxide with reactive oxygen species (hydroxyl radical, singlet oxygen, and superoxide anion). *Environ. Sci. Nano* **2019**, *6*, 3734–3744. DOI: 10.1039/C9EN00693A.

(253) Armstrong, D. A.; Huie, R. E.; Lymar, S.; Koppenol, W. H.; Merényi, G.; Neta, P.; Stanbury, D. M.; Steenken, S.; Wardman, P. Standard electrode potentials involving radicals in aqueous solution: inorganic radicals. *Bioinorg. React. Mech.* **2013**, *9*, 59. DOI: 10.1515/irm-2013-0005.

(254) Banerjee, S.; Wong, S. S. Demonstration of Diameter-Selective Reactivity in the Sidewall Ozonation of SWNTs by Resonance Raman Spectroscopy. *Nano Lett.* **2004**, *4*, 1445–1450. DOI: 10.1021/nl049261n.

(255) Gordeev, G.; Rosenkranz, T.; Hennrich, F.; Reich, S.; Krupke, R. Light Control over Chirality Selective Functionalization of Substrate Supported Carbon Nanotubes. *J. Phys. Chem. C* **2022**, *126*, 9803–9812. DOI: 10.1021/acs.jpcc.2c01628.

(256) Bashir, A.; Wöbkenberg, P. H.; Smith, J.; Ball, J. M.; Adamopoulos, G.; Bradley, D. D. C.; Anthopoulos, T. D. High-Performance Zinc Oxide Transistors and Circuits Fabricated by Spray Pyrolysis in Ambient Atmosphere. *Adv. Mater.* **2009**, *21*, 2226–2231. DOI: 10.1002/adma.200803584.

(257) Collin, F. Chemical Basis of Reactive Oxygen Species Reactivity and Involvement in Neurodegenerative Diseases. *Int. J. Mol. Sci.* **2019**, *20*, 2407. DOI: 10.3390/ijms20102407.

(258) Noé, J. C.; Nutz, M.; Reschauer, J.; Morell, N.; Tsioutsios, I.; Reserbat-Plantey, A.; Watanabe, K.; Taniguchi, T.; Bachtold, A.; Högele, A. Environmental Electrometry with Luminescent Carbon Nanotubes. *Nano Lett.* **2018**, *18*, 4136–4140. DOI: 10.1021/acs.nanolett.8b00871.

(259) Ju, S.-Y.; Kopcha, W. P.; Papadimitrakopoulos, F. Brightly fluorescent single-walled carbon nanotubes via an oxygen-excluding surfactant organization. *Science* **2009**, *323*, 1319–1323. DOI: 10.1126/science.1166265.

(260) Li, Y.; Wu, X.; Kim, M.; Fortner, J.; Qu, H.; Wang, Y. Fluorescent Ultrashort Nanotubes from Defect-Induced Chemical Cutting. *Chem. Mater.* **2019**, *31*, 4536–4544. DOI: 10.1021/acs.chemmater.9b01196.

(261) Ziegler, K. J.; Gu, Z.; Peng, H.; Flor, E. L.; Hauge, R. H.; Smalley, R. E. Controlled oxidative cutting of single-walled carbon nanotubes. *J. Am. Chem. Soc.* **2005**, *127*, 1541–1547. DOI: 10.1021/ja044537e.

(262) Makuła, P.; Pacia, M.; Macyk, W. How To Correctly Determine the Band Gap Energy of Modified Semiconductor Photocatalysts Based on UV-Vis Spectra. *J. Phys. Chem. Lett.* **2018**, *9*, 6814–6817. DOI: 10.1021/acs.jpclett.8b02892.

(263) Niidome, Y.; Yu, B.; Juhasz, G.; Fujigaya, T.; Shiraki, T. Structure Dependence of Photoluminescence Solvatochromic Energy Shifts Based on Exciton Localization in Locally Functionalized Single-Walled Carbon Nanotubes. *J. Phys. Chem. C* **2021**, *125*, 12758–12766. DOI: 10.1021/acs.jpcc.1c02109.

(264) Powell, L. R.; Piao, Y.; Wang, Y. Optical Excitation of Carbon Nanotubes Drives Localized Diazonium Reactions. *J. Phys. Chem. Lett.* **2016**, *7*, 3690–3694. DOI: 10.1021/acs.jpclett.6b01771.

(265) McDonald, T. J.; Blackburn, J. L.; Metzger, W. K.; Rumbles, G.; Heben, M. J. Chiral-Selective Protection of Single-walled Carbon Nanotube Photoluminescence by Surfactant Selection. *J. Phys. Chem. C* **2007**, *111*, 17894–17900. DOI: 10.1021/jp071410d.

(266) Wang, Y.; Wang, Q.; Zhan, X.; Wang, F.; Safdar, M.; He, J. Visible light driven type II heterostructures and their enhanced photocatalysis properties: a review. *Nanoscale* **2013**, *5*, 8326–8339. DOI: 10.1039/C3NR01577G.

(267) Brohmann, M.; Wieland, S.; Angstenberger, S.; Herrmann, N. J.; Lüttgens, J.; Fazzi, D.; Zaumseil, J. Guiding Charge Transport in Semiconducting Carbon Nanotube Networks by Local Optical Switching. *ACS Appl. Mater. Interfaces* **2020**, *12*, 28392–28403. DOI: 10.1021/acsami.0c05640.

Eidesstattliche Versicherung

gemäß §8 der Promotionsordnung für die Gesamtfakultät für Mathematik, Ingenieur- und Naturwissenschaften der Universität Heidelberg

1. Bei der eingereichten Dissertation zu dem Thema „Electrical and Optical Properties of Doped and Functionalized Semiconducting Carbon Nanotube Networks“ handelt es sich um meine eigenständig erbrachte Leistung.
2. Ich habe nur die angegebenen Quellen und Hilfsmittel benutzt und mich keiner unzulässigen Hilfe Dritter bedient. Insbesondere habe ich wörtlich oder sinngemäß aus anderen Werken übernommene Inhalte als solche kenntlich gemacht.
3. Die Arbeit oder Teile davon habe ich bislang nicht an einer Hochschule des In- oder Auslands als Bestandteil einer Prüfungs- oder Qualifikationsleistung vorgelegt.
4. Die Richtigkeit der vorstehenden Erklärungen bestätige ich.
5. Die Bedeutung der eidesstattlichen Versicherung und die strafrechtlichen Folgen einer unrichtigen oder unvollständigen eidesstattlichen Versicherung sind mir bekannt.

Ich versichere an Eides statt, dass ich nach bestem Wissen die reine Wahrheit erklärt und nichts verschwiegen habe.

Geesthacht, 27.04.2024

Sonja Wieland